Bachelor Thesis

Degree Project in
Marine Geology 15 hp

Identification of gas seeps associated with fracture zones in the southwestern Baltic Sea using open-source software

Victor Bäcklin

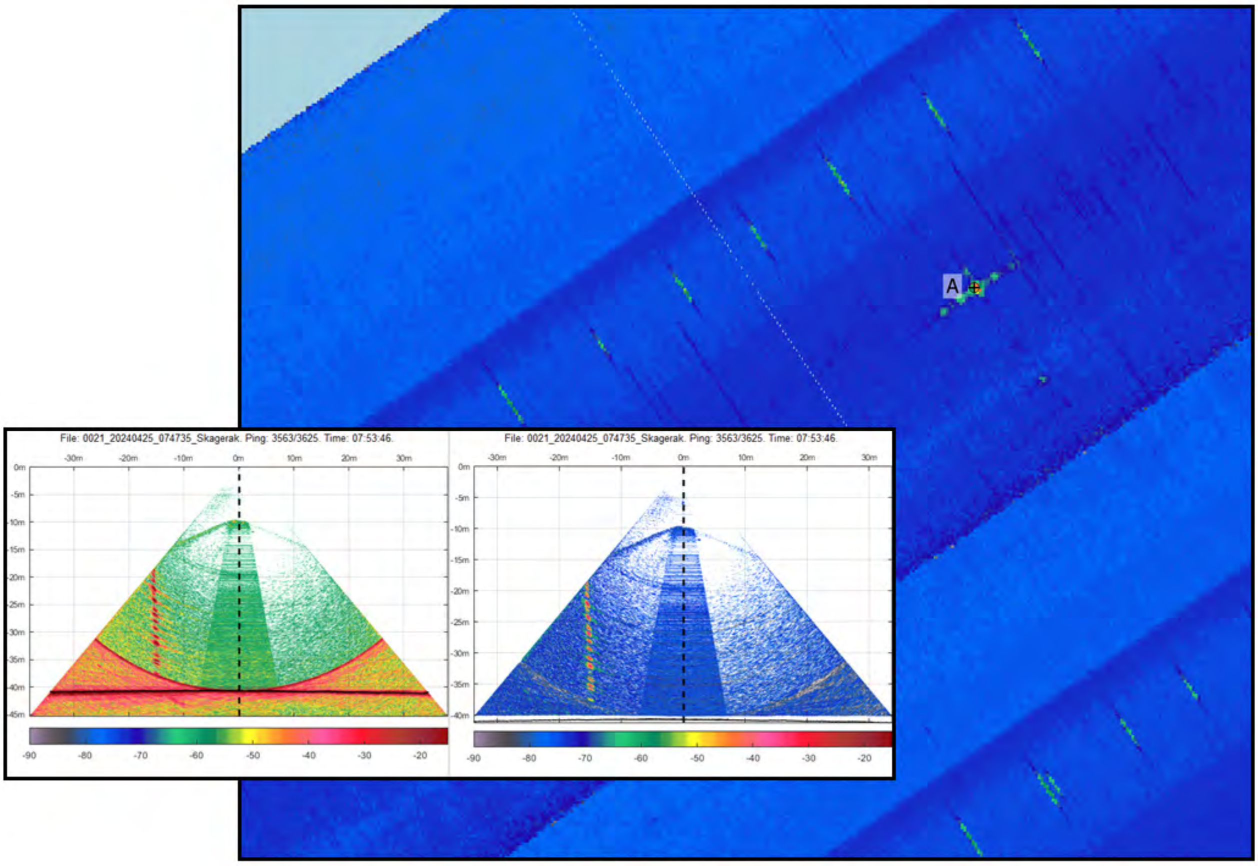

Stockholm 2025

Department of Geological Sciences
Stockholm University
SE-106 91 Stockholm

Abstract

Geological carbon capture and storage (CCS) has been identified as a valuable tool in addressing rising atmospheric CO_2 levels. In fracture zones, marine gas seeps can indicate compromised storage integrity and must be identified for both pre-injection assessments and post-injection monitoring. Traditional analysis of multibeam echosounder (MBES) water column data for seep detection is labor-intensive and impractical, especially for large datasets. This study evaluates Espresso, an MIT-licensed open-source software, as a tool for efficient gas seep detection through filtering and echo integration of MBES water column data. A known seep site in Byfjorden, Sweden, was used for validation, followed by application to sub-regions of a fracture-rich CCS candidate area in the southwestern Baltic Sea. Echo-integrated grids revealed 17 seep-like anomalies in the candidate area, particularly concentrated in one region. No spatial correlation with mapped fault lines was found, suggesting a likely biogenic origin. However, seep interpretation remains highly uncertain due to ambiguities in acoustic morphology, inclination, and the absence of updated water current measurements. Several filtering limitations were also encountered during this project, and ideas for potential improvements are discussed. The results suggest that, while Espresso is a useful tool for preliminary seep detection, professional software and supporting hydrological data remain essential for conclusive interpretation.

Sammanfattning

Geologisk infångning och lagring av koldioxid (CCS) har identifierats som ett värdefullt verktyg för att hantera stigande atmosfäriska CO_2-nivåer. I marina sprickzoner kan gasutsläpp, i form av bubbelströmmar, indikera bristande lagringsintegritet och måste identifieras för både lämplighetsbedömning före injektion och övervakning efter injektion. Traditionell analys av vattenkolumnsdata från multistråle-ekolod (MBES) är arbetsintensiv och opraktisk, särskilt för stora datamängder. Denna studie utvärderar Espresso, en MIT-licensierad öppen källkodsprogramvara, som ett verktyg för effektiv gasdetektion genom filtrering och ekointegration av vattenkolumnsdata. Ett område med bekräftade gasutsläpp i Byfjorden, Sverige, användes för validering, följt av tillämpning på delområden av ett sprickrikt CCS-kandidatområde i sydvästra Östersjön. Ekointegrerade mosaiknät avslöjade 17 läckageliknande anomalier i kandidatområdet, särskilt koncentrerade till ett område. Ingen rumslig korrelation med kartlagda förkastningslinjer kunde påvisas, vilket sannolikt tyder på gas av biologiskt ursprung. Tolkningen förblir dock osäker på grund av oklarheter i akustisk morfologi, lutning samt avsaknaden av uppdaterade mätningar av vattenströmmar. Flera filtreringsbegränsningar påträffades också under detta projekt, och idéer till potentiella förbättringar diskuteras. Resultaten antyder att även om Espresso är ett användbart verktyg för preliminär gasdetektion, är professionell mjukvara och kompletterande hydrologiska data fortfarande avgörande för en tillförlitlig tolkning.

Keywords: CCS, Geological storage, Gas seeps, Multibeam, Hydroacoustics, Water column imaging, Backscatter, Echo Integration, Sidelobe filtering, Baltic Sea, Arkona Basin, Climate change

Contents

1 Introduction

Carbon capture and storage (CCS) is an increasingly relevant climate mitigation strategy, and a critical aspect of its viability is the long-term integrity of geological storage sites (Chadwick et al., 2008). Leakage indicators such as gas seeps, especially in areas with prominent faults and fractures, can reveal potential pathways through which injected CO_2 may migrate to the seafloor. Even in the absence of leakage, gas seeps may indicate in-situ biogenic processes, and identifying these is important for distinguishing future leakage from natural background seepage (Andersson et al., 2023). Therefore, early detection of gas seeps is crucial, both pre- and post-injection.

Traditional manual analysis of multibeam echosounder (MBES) water column backscatter for gas seeps detection is labor-intensive and costly, particularly for large survey areas (Mitchell et al., 2022). Additionally, the inherently noisy nature of this water column data (WCD) further complicates the reliable identification of seepage features (Urban et al., 2017). These challenges highlight the need for more efficient and accessible tools for gas seep detection.

One promising method for anomaly detection is echo integration, in which the WCD is vertically stacked into a two-dimensional grid, creating a heatmap overview where high-backscatter targets, such as gas seeps, can be more easily detected from a top-down perspective (e.g., Lamarche et al., 2019; Mitchell et al., 2022; Turco et al., 2022; Urban et al., 2017, 2023). However, no commercial WCD processing software currently implements this functionality.

This study investigates whether Espresso, a free and open-source tool for WCD processing and echo integration (Schimel et al., 2024a), can be used efficiently to identify possible gas seeps. To achieve this, two datasets are analyzed: **1.** a known seep site in Byfjorden, Uddevalla, Sweden, used as a validation case, and **2.** a fracture zone in the southwestern Baltic Sea, currently under assessment as a potential CCS storage site as part of a national Government Assignment.

The aim is to evaluate Espresso's performance in both controlled and uncertain seep environments, and assess its suitability for integration into marine geophysical survey workflows of large-scale CCS site investigations.

This study was conducted in association with the Geological Survey of Sweden (SGU) as part of their ongoing CCS assessment (Andersson et al., 2023, 2025).

2 Background

2.1 Carbon Capture and Storage (CCS)

Carbon capture and storage (CCS) involves capturing carbon dioxide (CO_2) emissions and injecting them into deep geological formations for long-term storage. These formations must consist of a sequestration reservoir, i.e. a permeable sedimentary formation with high porosity, overlain by low permeability caprocks. The CO_2 is injected into the reservoir in a supercritical fluid state, allowing large volumes of gas to be compressed into much smaller volumes for storage (Rutqvist, 2012).

Once injected, the CO_2 is retained in the reservoir by a combination of geochemical and physical trapping mechanisms. Geochemical trapping includes dissolution, ionic dissociation and mineral precipitation (Okuyama et al., 2011), while physical mechanisms include capillary trapping (immobilization due to interfacial tension) (Benson and Cole, 2008) and structural trapping by the sealing capabilities of the caprock, which inhibits any meaningful amount of migration of residual CO_2 (Fleury et al., 2011).

CCS is considered a valuable tool to battle the challenge of the rise in atmospheric CO_2, which recent studies have shown hit record high rates between 2023 and 2024 (Ke et al., 2025). Although successful implementations have been demonstrated within the last couple of decades (Haszeldine et al., 2014), concerns remain about leakage through faults, fractures or wells, especially in marine environments (Oldenburg et al., 2009). Monitoring strategies for possible seepage are vital to ensure containment and evaluating storage performance (Chadwick et al., 2008), although some studies suggest that fractures and/or leakage does not necessarily mean inefficient long-term storage (Haszeldine et al., 2014; Vielstädte et al., 2019). Nonetheless, international guidelines exist for evaluating a potential storage site, including risk assessments of potential leakage in fracture zones (Dixon et al., 2014; International Maritime Organization, 2012). In light of these risks, it becomes critical to identify any present-day gas seepage when evaluating sites for CCS deployment. This is particularly important along fault zones, where seepage can reveal existing migration pathways along the fractures that may encourage leakage. When monitoring the region post injection, awareness of existing marine gas seeps is also important to help distinguish between leakage of CO_2 from the reservoir and seepage of natural origins (Andersson et al., 2023).

2.2 Marine Gas Seeps

Marine gas seeps, usually consisting of CH_4 or CO_2 (Lamarche et al., 2019), can originate from biogenic sources in shallow seafloor sediments or from deeper thermogenic hydrocarbon reservoirs (Suess, 2018). Advances in echo sounding technology, particularly the maturation of multibeam echosounders (MBES), have significantly improved the ability to study these seeps over the past few decades. Research typically range from identification and detection (e.g. Lamarche et al., 2019; Mitchell et al., 2022; Nau et al., 2022; Schneider Von Deimling and Papenberg, 2012; Schneider Von Deimling et al., 2007; Spain et al., 2022; Urban et al., 2017; Weber, 2021; W. Zhang et al., 2022; Zhao et al., 2017, 2020), to quantitative methods estimating fluxes and environmental impacts due to the powerful green house gas characteristics of methane (e.g. Higgs et al., 2019; Leifer et al., 2006; Ruppel et al., 2024; Skarke et al., 2014; Turco et al., 2022; Urban et al., 2023; Von Deimling et al., 2010; Weber et al., 2014). In water column backscatter soundings provided by modern MBES systems, gas seeps typically show up as (semi-)vertical plumes, or flares, due to the strong acoustic reflection of the bubbles (Fig. 1). This acoustic reflectivity is caused by the large difference in acoustic impedance between water and gas, as well as the size dependent resonant frequency of gas bubbles, making them strong acoustic reflectors (Colbo et al., 2014).

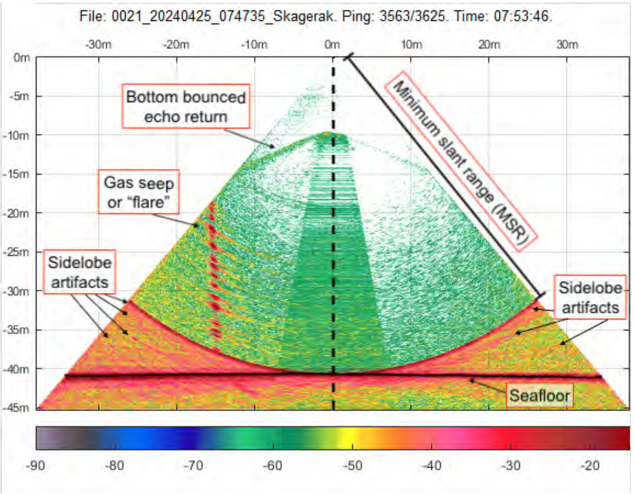

Fig. 1: Example of a marine gas seep flare, shown in the typical "fan view" of water column backscatter data, together with some typical acoustic artifacts. See Section 4 for details and more examples.

2.3 Water Column Backscatter

Multibeam echosounders were originally developed in the 1970s to map the seafloor by emitting a fan of acoustic beams and measuring the return time and intensity of each signal. Compared to single-beam systems, MBES offers significantly greater spatial coverage, enabling high-resolution bathymetric mapping. Over time, MBES systems have become increasingly more sophisticated, providing not only precise bathymetry but also detailed acoustic backscatter data from both the seafloor and the water column (Hughes Clarke, 2006).

Water column returns capture the strength of acoustic reflections from midwater targets such as gas bubbles, fish, or debris at varying depths (Colbo et al., 2014). This dataset of backscatter intensities, commonly referred to as water column data (WCD), is inherently multidimensional. Each recorded value corresponds to a specific *ping* (i.e. one acoustic transmission and its received echoes), *beam* (a directional segment of the acoustic fan), and *range* (the distance from the sonar to the reflecting target). Compared to seafloor-focused datasets like bathymetry or bottom backscatter, which typically store data indexed only by ping and beam, WCD captures a full vertical profile for each beam. This means that every ping-beam pair will contain hundreds or even thousands of additional values, each representing signal strength at a different range from the sonar head through the water column (Schimel et al., 2024b). This makes WCD much larger in size and therefore impractical for data transfer, processing and storage.

Another major challenge in working with WCD is its susceptibility to noise and artifacts, especially outside of the minimum slant range (MSR, see Fig. 1). Hughes Clarke, 2006, Nau et al., 2025, and Ryan et al., 2015, all do an excellent job describing and summarizing some of the most common artifacts, including sidelobe interference, outer beam noise, nadir artifacts, impulsive noise, transient noise, propeller noise, bubble wash-down masking, and echo returns from direct arrival or bottom bounces. Visual examples of some of these artifacts can be seen in Fig. 1, and more will be explored in Sections 4.1 and 6.1.

The aforementioned complexities of WCD presents challenges for visualization and interpretation, particularly when scanning large volumes of data for subtle anomalies like gas seeps.

2.4 Previous Work in Gas Seep Identification

Historically, detecting gas seeps has been done by manually looking at the "fan view" (sometimes referred to as "wedge view") of each individual ping (see e.g. Fig. 1 for a visual example), scanning for characteristic acoustic anomalies that indicate seepage (e.g. Higgs et al., 2019; Skarke et al., 2014; Weber et al., 2014). A single MBES survey line can consist of thousands of individual pings, with regional scale surveys sometimes amounting to hundreds (or even thousands) of survey lines, indicating an immense amount of labor needed. It has been reported that as much as half of a typical 12 hour shift during offshore surveys can be spent reviewing water column data using this manual method (Mitchell et al., 2022).

Due to these limitations, considerable effort has been put into the development of automated detection methods for gas seeps and other midwater acoustic targets. Early work by McGonigle et al., 2010, incorporated intensity thresholding in combination with machine learning techniques like PCA (principal component analysis) and k-means clustering for the classification of benthic macroalgae (kelp). Schneider Von Deimling and Papenberg, 2012, introduced a particle imaging velocimetry (PIV) algorithm on rising bubble patterns for automated bubble detection, although this approach was limited to spatially separable groups of bubbles and require high resolution in-situ monitoring for any quantitative analysis. Zhao et al., 2017, showed improved detection by extracting the morphological features of gas flares from the intersect of threshold-segmented images, though the method was limited to seeps found within the MSR. This detection method was later expanded on by introducing a Haar-LBP detector for automatic classification, eliminating the MSR restraint and achieving high accuracy rates (Zhao

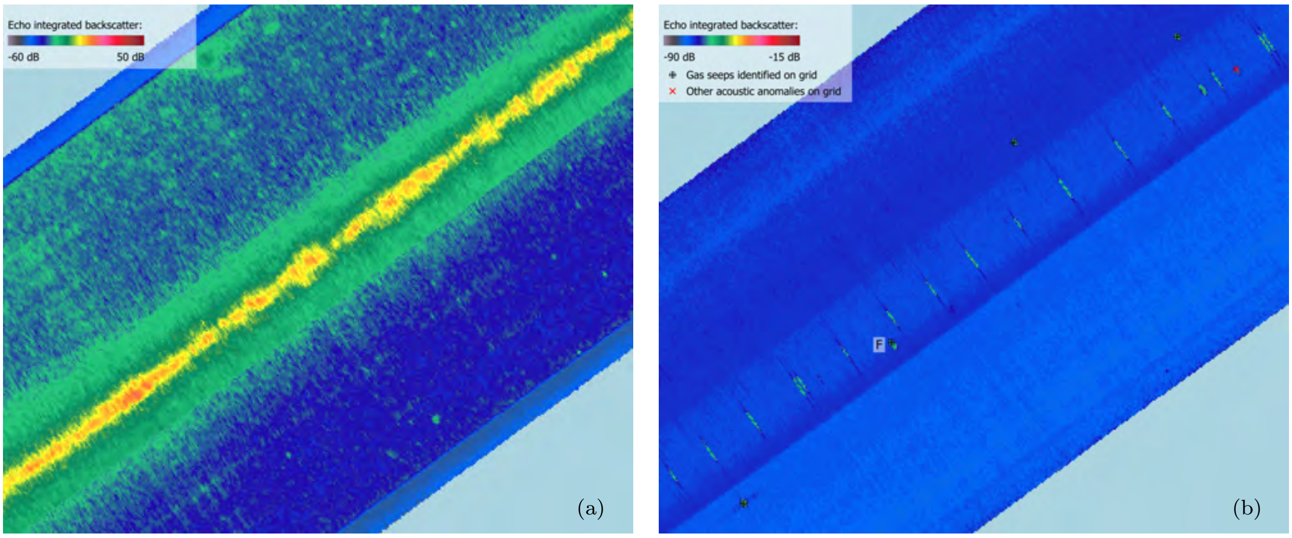

Fig. 2: Comparison showing the importance of processing the water column data for effective anomaly identification on an echo integrated grid, including gas seep F from Section 4.2. (a) shows the full WC data gridded without any preprocessing, while (b) is preprocessed and gridded with the parameters discussed in Section 3.2.

et al., 2020). The morphological characteristics of gas plumes, such as the tall-and-narrow aspect ratio, were also utilized by Weber, 2021, in conjunction with a cell-averaged constant false alarm rate (CFAR) detector to filter the test data down to a fraction of a percent, effectively leaving only the suspected gas seeps. However, this method could require different parameters depending on factors like water depth, echo sounder type and specific target characteristics, limiting its full automation across different settings. Nau et al., 2022, also used a series of thresholds and noise filters to extract gas seep point clouds with high accuracy.

In more recent developments, some researchers have started to explore the utilization of deep learning techniques like convolutional neural networks (Hicks et al., 2023; Manjur et al., 2025) with favorable results. Another promising line of research focuses on echo integration techniques, which aim to quantify backscatter intensity across larger spatial volumes (e.g. Urban et al., 2017).

Modern high-end commercial WCD processing software, like FMMidwater from QPS ("FMMidwater", 2022) and Echoview ("Echoview", 2021), have developed tools to identify flares in WCD, typically based around filtering of background noise and target identification of point clusters to separate seeps. They have however yet to implement any functionality for deep learning seep classification or echo integration.

2.5 Echo Integration

Echo integration (EI) is a method that quantifies acoustic backscatter by vertically stacking water column data over a defined volume, producing a 2D-grid raster allowing the visualization of many gigabytes of data as a single heatmap, particularly useful for identifying anomalies across wide areas. While EI has long been used for estimating biomass in fisheries applications (Colbo et al., 2014; Maclennan, 2002), the last decade has seen growing interest to both identify, map and quantify other targets in the water column, including benthic macroalgae (Porskamp et al., 2022) and gas seeps (Lamarche et al., 2019; Mitchell et al., 2022; Turco et al., 2022; Urban et al., 2017, 2023). Most of these studies include preprocessing and filtering the WCD prior to integration and gridding to avoid generating noisy mosaics in which target anomalies become difficult to distinguish (Fig. 2).

Urban et al., 2017, disregarded data outside the MSR and applied a median mask filter to reduce static artifacts. A 3D flare template was then used to correct for bubble displacement caused by ocean currents, resulting in more accurate geolocation of seep origins on an 2D gridded "acoustic flare map". While effective, the method was not well suited to areas with complex bathymetry. Urban et al., 2023, later expanded on their previous work, using numerical simulation in combination with echo integration to quantify gas bubble emissions. Mitchell et al., 2022, demonstrated how echo-integrated heat maps could serve as a powerful alternative to manual geopicking from fan views during offshore surveys, comparing EI-based results to previously manually marked seeps from an offshore survey with over 600 detected features. The study effectively showed that manual methods not only had lower spatial accuracy but also missed several seeps entirely. Turco et al., 2022, applied echo integration to MBES data to quantify the spatial extent of methane vents at the southern Hikurangi Margin. By pairing this with split-beam echosounder measurements that allowed them to estimate gas fluxes from representative flares, they could extrapolate total annual methane emissions across the region. This integrated approach enabled one of the most comprehensive methane flux assessments for the area to date.

2.6 Espresso

Espresso is an open-source research software, written in MATLAB, designed for processing and echo integra-

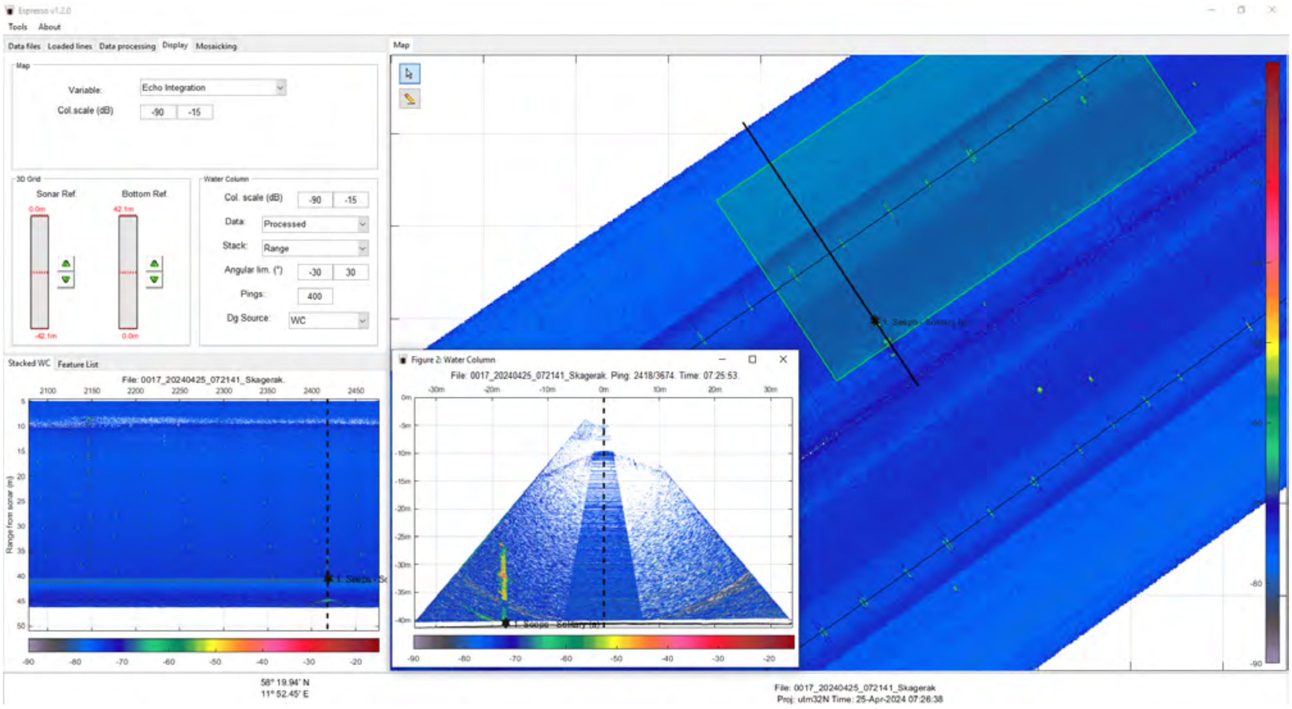

Fig. 3: The UI for the Windows compiled Espresso. The main section on the right shows the map view, including the echo integrated grids where acoustic anomalies can be detected from a top-down view. Top left currently shows the display parameters, but includes tabs for file management, MBES line selection, data processing and mosaic generation as exported GeoTIFF files. Bottom left shows the side stacked view, with the currently selected stacked ping range and beam angle indicated by the green block on the EI grid. To the right of the stacked view we see the fan view displaying the current ping, denoted by the solid across-track black line on the EI grid and the dashed black line in the stacked view. A seep has been marked with the geo-picking tool to create a point feature that can be exported as a shapefile.

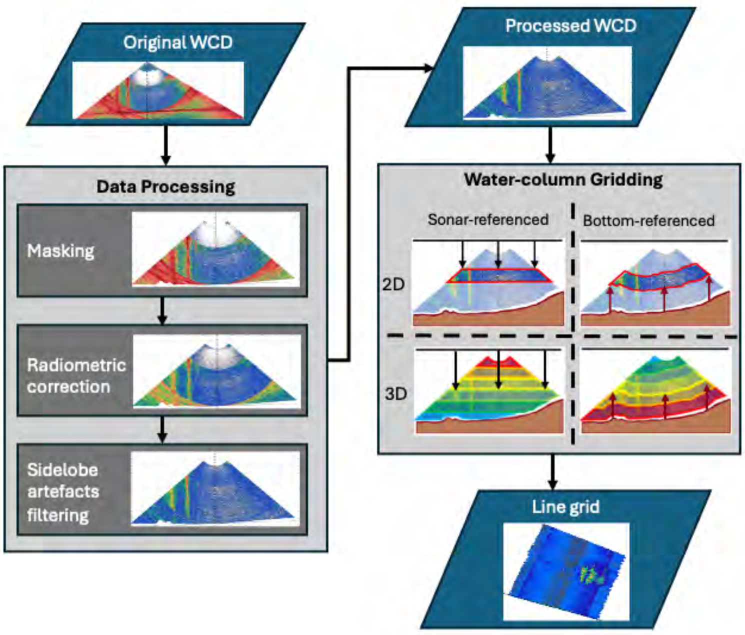

Fig. 4: Image from the Espresso User Guide, visualizing the workflow for the processing and gridding of water column data in Espresso.

tion of multibeam water column data. It is available under the MIT license and was originally developed by researchers at NIWA (National Institute of Water and Atmospheric Research, New Zealand) (Schimel et al., 2024a). All source code is available at GitHub, as is a Windows compiled standalone application with a full user interface (UI). Espresso is built upon the MATLAB WCD processing toolkit CoFFee, developed to facilitate rapid processing of MBES data. As Espresso is a research tool developed by researchers it has certain limitations when compared to commercial software, such as lower positional accuracy and quality sacrifices due to simplified processing (Schimel et al., 2024b). Currently, it supports only a few MBES formats: Kongsberg's .all/.wcd and .kmall/.kmwcd, and Teledyne-Reson's .s7k. Nonetheless, it provides the public with a set of powerful and easy to use WCD processing tools, and has so far been used effectively in research for gas seep flux estimation (Turco et al., 2022) and benthic habitat mapping (Porskamp et al., 2022; Schimel et al., 2020). Additionally, the built-in bottom detect functionality also allows Espresso to calculate and grid both bathymetry and seafloor backscatter.

Fig. 3 shows the main window for the Windows compiled version of Espresso. The top left contains tabs for file management, line display, data processing, display parameter setting and mosaicking. Before processing and visualization, supported MBES files needs to be converted to the specialized fData format arrays used by Espresso and selected to load these into memory.

The data processing workflow in Espresso can be broadly divided into three main stages:

(1) The "Mask selected data" options allow for unnecessary data to be excluded from further analysis. These options include noisy outer beams outside a set angle, bad pings, a specific depth range from the sonar or above the seafloor, as well as everything beyond the MSR.

(2) For the measured backscatter signal to have any use in quantitative studies, the signal must be corrected due to the interactions caused by both water column and seafloor, as well as the hardware and software of the MBES system itself. This is known as "Radiometric correction" (Schimel et al., 2018), and Espresso implements this with a user choice of desired output reference:

- S_v - Volume backscattering strength
- TS - Target strength
- S_a - Surface backscattering strength

These acoustic properties are formally and mathematically defined in Maclennan, 2002. In short TS can be understood as the backscatter by a single point target and is therefore useful as a corrected output when it is important that a single fish returns the same echo level no matter the depth, while S_v is the backscatter of 1 m^3 of a more diffuse target (like bubbles in a gas seep) that is spread over a volume of water and therefore ensures consistency that a diffuse target returns a consistent echo level at different depths. S_a is similar to S_v but spread over a surface instead of a volume. The Espresso User Guide does however point out that, due to missing information from the raw MBES data, absolute levels can not be achieved and the resulting output will still vary from true calibrated values by a constant offset. This radiometric correction is not fully necessary for qualitative tasks, like gas seep detection, but it still helps to paint a more accurate picture of acoustic responses than the measured MBES backscatter values.

(3) Schimel et al., 2020, described a "slant-range signal normalization" (SRSN) algorithm that effectively removes sidelobe induced artifacts, including the strong "specular artifact" that approximately marks the MSR (see the strong curved red line in Fig. 1). In essence, for each ping it calculates the average backscatter level for every sample at a given range, i.e. distance from the sonar. This average is then subtracted from all samples at that range, followed by adding back a reference level calculated from the average of the 11 most central beams, which are typically less noisy. This process is then repeated for all ranges in the ping. The filter therefore removes all noise that is range-dependent, like sidelobe artifacts tend to be, for all ranges in every ping. The SRSN algorithm is implemented in Espresso as "Filter sidelobe artefacts". The combination of these three processing steps filters the data to help separate interesting acoustic targets without disregarding the noisy areas outside the MSR, as seen in the left side of Fig. 4.

After processing, the water column data can be echo integrated and gridded. The most important consideration for this process is how to define the volume to integrate. The depth slice for integration can be chosen in two different ways; sonar referenced or bottom referenced. Sonar referenced depth is simply the distance from the sonar, i.e. approximately the hull of the vessel. Choosing to integrate over a sonar referenced depth between 10 and 25 meters would then integrate over the volume made up by all the pings cutoff as 15 meter thick depth slices starting 10 meters under the sonar. If bottom referenced integration is instead chosen, the volume would be composed of all the pings cutoff into 15 meter slices positioned 10 meters above the bottom. There is also an alternative to create multiple grids by integrating over several depth slices, whether sonar or bottom referenced, with a chosen thickness, referred to as "3D Water-column gridding". See the right side of Fig. 4 for a visualized example of these different gridding methods. Other settings include data decimation for saving memory and processing speed up, as well as cell resolution of the resulting grid. During echo integration, each sample is first georeferenced according to the method described in Schimel et al., 2018. Samples falling within the same grid cell are then summed vertically and normalized by the number of contributing samples.

Once all data has been processed and gridded, acoustic anomalies can be explored using the **map view**, containing the grids from a top-down perspective, the

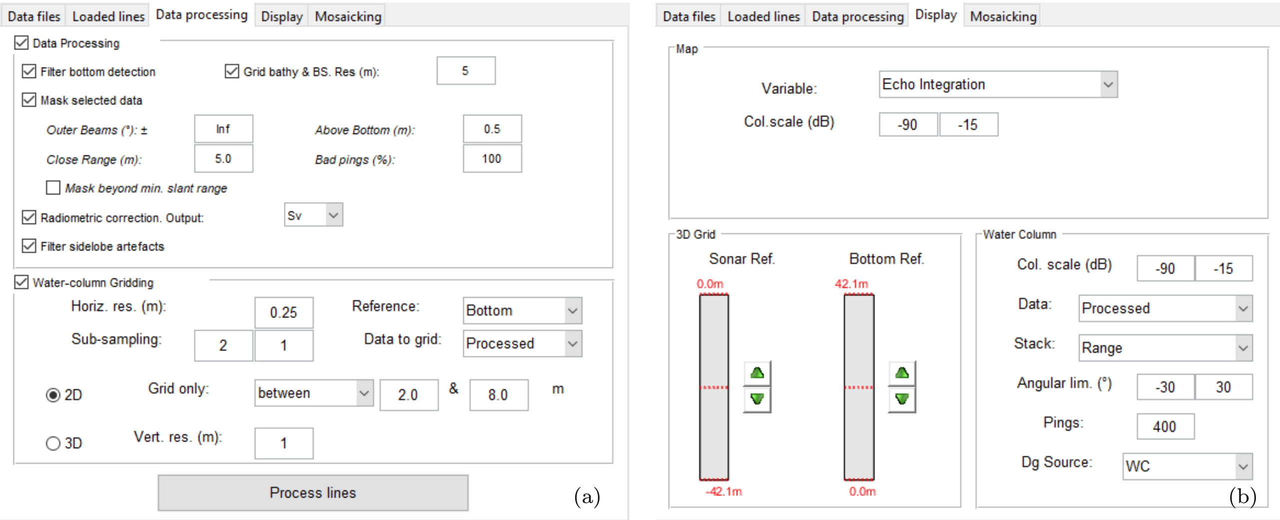

Fig. 5: (a) Processing and (b) Display parameters used for the Byfjorden dataset.

stacked view, which displays a side-on compilation of successive pings across a selected beam range, and the **fan view**, which shows the backscatter of a single ping in cross-track perspective (see Fig. 3). Any important findings can be geo-picked as point or polygon features and exported as vector shapefiles, while the grids can be exported as mosaics, in the form of GeoTIFF raster files. These exports can then be used in e.g. GIS-software for spatial analysis and visualization.

In this project, Espresso served as the primary tool for processing and echo integration of water column data, with the aim of evaluating its effectiveness for seep detection across a large spatial area in support of a potential CCS project. Specific parameter choices and dataset workflows are detailed in Section 3.2.

3 Materials and Methods

3.1 Datasets

Two water column datasets were used in this project:

1. A known gas seep site in Byfjorden (Uddevalla, Sweden). This data was used for baseline validation of seep detection and helped to guide the parameters later used for seep hunting in the second dataset. This dataset will be referred to as the Byfjorden data, and was collected on 25 April 2024 with the Kongsberg EM 2040 MBES. See Section 4 for details.

2. A small subset of a large survey area in the southwestern Baltic Sea, off the southern coast of Skåne, Sweden. This area is one of two large regions selected by the Geological Survey of Sweden (SGU) as a potential candidate for CCS utilization as part of a national Government Assignment (Andersson et al., 2023), and the aim of this project is to assess whether Espresso is a valid tool to use for qualitative seep detection over the large faults in this region. This data, which will here be referred to as the Skåne data, was collected in April and June 2024 using a Kongsberg EM 2040 Dual Rx system with a wider swath angle. See Section 5 for more information.

3.2 Workflow and Processing Parameters

The general workflow for processing, EI gridding, analysis, and visualization of the water column data in this project followed these main steps:

(1) Files for a region were located in Espresso's file manager and converted and processed using the "Batch stacked WC export" tool, with the "Keep converted files" setting enabled. This tool converts an entire folder of raw WCD files to the fData format used by Espresso, processes them using the currently set "Data Processing" parameters, and then generates screenshots of the stacked views for every line based on the selected display parameters. Only one MBES line is loaded at a time in this batch mode, ensuring that system RAM is not exceeded, important given the typically large size of WCD files. This functionality allows for substantial amounts of data to be processed overnight, avoiding the need to load lines manually or risk software crashes. The resulting collection of stacked view screenshots offers a high-level overview of the dataset and the possible acoustic anomalies it may contain. All stacked view screenshots from this project are included in Appendix B.

(2) After all files were converted and processed, a few lines at a time (due to hardware limitations) were selected for EI gridding, as described in Section 2.6. These grids, in combination with the corresponding stacked views, were then manually inspected for acoustic anomalies. Polygon or point features were created for any interesting anomalies using the built-in geo-picking tool. Screenshots were also taken of the fan view for visual reference. Additionally, GIF animations were created from several consecutive pings for those anomalies that were difficult to interpret by viewing a single ping.

(3) The "Mosaicking" tool was used to generate GeoTIFF raster files that were exported for each EI grid, along with vector shapefiles of the created features. These files were then imported into QGIS (QGIS Development Team, 2024) for mapping and spatial analysis.

While some initial exploration of both datasets was done manually using selected lines to test appropriate settings, the final processing and gridding parameters were chosen with the objective of seep detection in mind. The parameters used for the Byfjorden dataset are shown in Fig. 5. The bottom filter was enabled to avoid acoustic artifacts like beam smearing at the seafloor, and the 0.5 meters closest to the seafloor were excluded. The 5 meters closest to the sonar were also masked out, as this region often contains vessel-related noise like bubble wash down (e.g. Hughes Clarke, 2006) and is not necessary for seep detection. No outer beams or bad pings were excluded, in order to retain a complete overview of the dataset, including its imperfections. Radiometric correction was applied with S_v output, as this is appropriate for diffuse targets like gas seeps, and sidelobe artifacts were filtered as described in Section 2.6.

The Skåne dataset was processed using similar filtering, with one major exception: the exclusion of the noisy outermost beams, due to the much wider swath width used in that survey. Only the inner ±70° beams were retained to improve fan view readability by avoiding overly wide acoustic coverage, while still preserving a reasonable survey area per line. Additionally, the stacked view display was adjusted to show 600 pings per block (instead of 400), to reduce the number of screenshots per line. This was deemed necessary as the Skåne survey lines often exceeded 6000 pings, compared to around 3600 pings per line in the Byfjorden dataset.

EI gridding parameters (Fig. 5a, lower panel) were selected based on the expected morphology of gas seeps and informed by visual inspection of the stacked view screenshots. A bottom-referenced 2D grid was chosen to ensure that seeps originating from the seafloor were captured, even in areas with variable bathymetry. To reduce processing time, every other sample was decimated, while all beams were retained for resolution purposes. The lowest 2 meters above the seafloor were excluded to suppress near-bottom noise from fish or boulders. The upper limit of integration was set to 8 meters above the seafloor, focusing the grid on the region where rising flares are most likely to appear while minimizing interference from unrelated targets higher in the water column. This resulted in a 6-meter-thick integration window. The Byfjorden dataset was gridded at a horizontal resolution of 0.25 m, while the Skåne dataset was gridded at 0.5 m due to its wider swath width and resulting lower spatial resolution.

Preliminary exploration of the known seep site in Byfjorden showed that some seeps may only be visible in the upper water column (see Section 4.2). This means that some seeps could be missed by the selected grid parameters. However, in the context of a CCS pre-study, it is reasonable to assume that meaningful seepage from deep geological sources would manifest more prominently throughout the water column. Likewise, minor near-bottom seeps with limited vertical extent are more likely biogenic in nature and should not indicate leakage risk. The 2–8 m window was therefore chosen to strike a balance between coverage and focus. A more narrow integration window (e.g. 3–4 m above the bottom) might further suppress interference from unrelated targets while still capturing major seepage events, but at the cost of potentially missing subtle features. The selected window aims to ensure thoroughness, even if it increases the number of anomalies to manually assess, especially since awareness of even minor biogenic seepage is important for distinguishing future leakage signals during post-injection monitoring.

Finally, some additional grid variations were generated at a few select positions (e.g. Fig. 2, Fig. 21, Fig. 22) to demonstrate how parameter choices can significantly affect the output.

4 Test Case: Byfjorden

Since the presence of gas seeps in the main CCS pre-study area was unknown, baseline validation of the filtering, echo integration, and seep detection capabilities of Espresso was first performed on a dataset where seepage had already been confirmed. This reference dataset was collected in April 2024 in Byfjorden, Uddevalla, during a survey conducted by the research vessel *R/V Skagerak* (Göteborgs Universitet, 2024). The expedition, led by Bonaglia et al. for the University of Gothenburg (publication pending), utilized a Kongsberg EM 2040 multibeam echosounder to record the WCD. A multitude of flare structures were discovered, attributed to gas seepage from CH_4 rich sediments. All six MBES lines used in this test case were surveyed on the morning of 25 April 2024.

Section 4.1 examines systematic artifacts observed in the dataset both before and after processing, in order to evaluate the effectiveness of Espresso's filters. Section 4.2 presents a selection of seeps, illustrating how different expressions of gas release appear in fan and stacked views.

Figure 6 provides an overview of the survey area, displaying the echo-integrated grids. It highlights gas seeps readily visible on the grid, seeps only detectable through manual inspection, and other transient acoustic anomalies. Two zoomed-in panels illustrate the visual appearance of these anomalies on the EI grids.

4.1 Artifacts and Noise

The general background noise in the Byfjorden dataset is illustrated by the representative ping in Fig. 7a. Sidelobe induced artifacts, inherent to the Mills Cross beam pattern used by Kongsberg MBES systems (Hughes Clarke, 2006), are clearly visible. These appear as high-intensity returns outside the minimum slant range (MSR), resulting from sidelobes in recep-

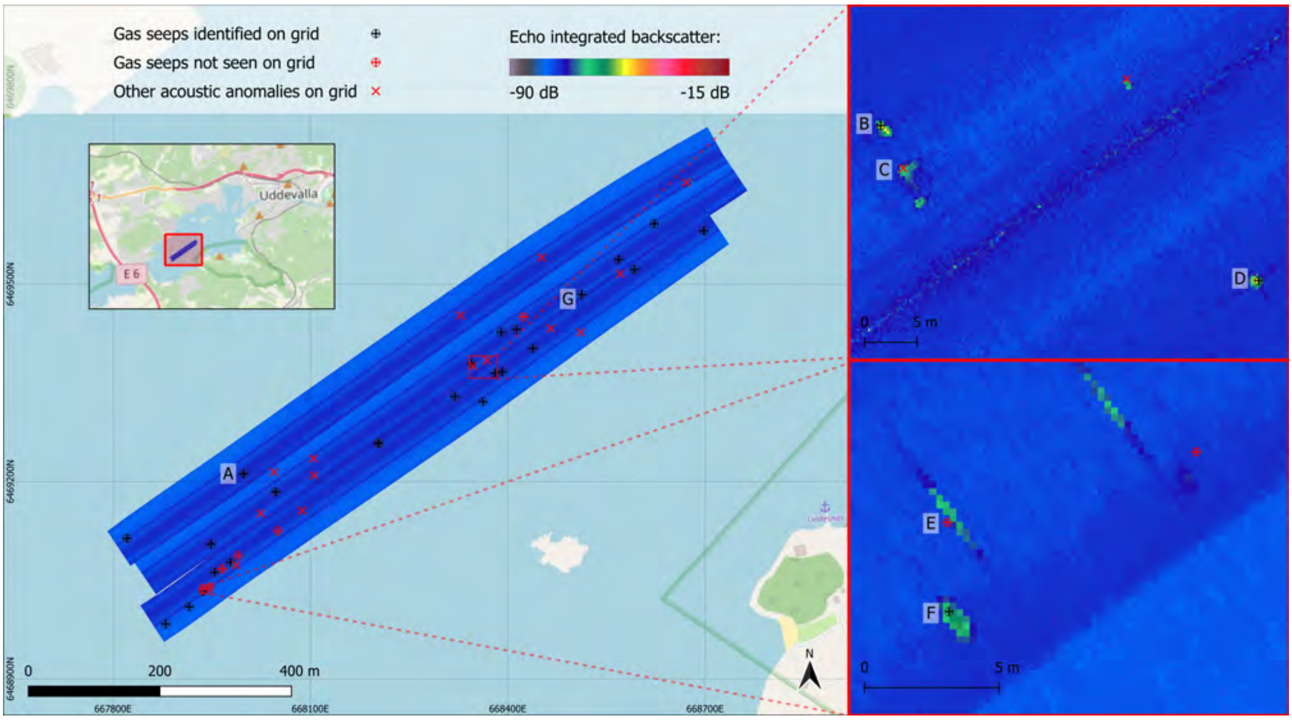

Fig. 6: Map of the research area in Byfjorden, and its position relative to the town of Uddevalla, including echo-integrated backscatter mosaics with two zoomed-in areas for detail. Marked on the map are gas seeps identified from the grid, seeps only visible through manual inspection of fan or stacked views, and other non-seep acoustic anomalies (e.g. fish). Labels of capitalized letters refer to anomalies explored in fan and stacked view in Section 4.2. Coordinate system: SWEREF99.

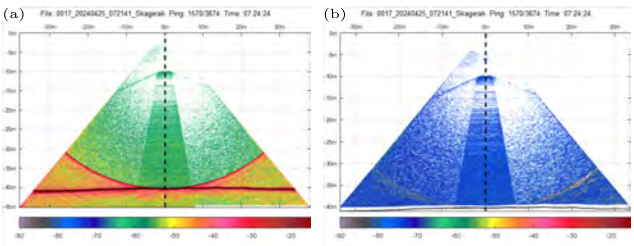

Fig. 7: A representative single ping of the water column in fan view from Byfjorden, (a) before and (b) after processing.

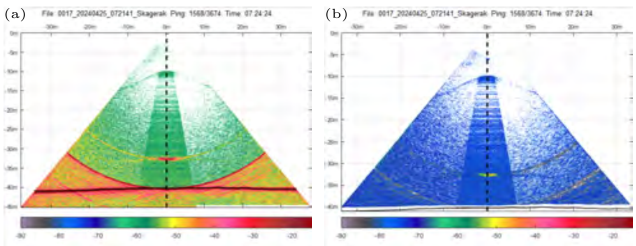

Fig. 8: Ping in fan view showing a typical example of the repeated artifact that persists throughout the Byfjorden dataset, (a) before and (b) after processing.

tion. A prominent static "frown-shaped" artifact is also visible, consistent with what Schimel et al., 2020, describe as a transmit sidelobe artifact, caused by along-track energy reflecting off the seafloor. This phenomenon is also referred to as a bottom bounced echo return by Hughes Clarke, 2006 (see Fig. 1 for annotated artifact explanations). There seems to be a general trend of intensity increasing with range from the sonar, as well as some outer beam noise, even inside the MSR. These features align with typical system artifact patterns observed for the EM 2040, as noted by Nau et al., 2025.

Fig. 7b shows the same ping after applying the processing described in Section 3.2. The radiometric output correction has shifted the general background intensity from around –60 dB to a range between –70 and –80 dB. The sidelobe induced artifacts from reception are well suppressed, as is the slant range-dependent intensity within the MSR. This outcome is expected, given the SRSN algorithm's normalization of the data by range (see Section 2.6). However, some sidelobe features may be slightly overcorrected, appearing weaker than the surrounding background signal, especially for the strong artifact that approximately outlines the MSR. This could be due to a particularly strong nadir return at the seafloor, elevating the mean backscatter level subtracted during normalization. The bottom bounced echo return is not filtered out, as it appears at different ranges across the beam fan.

In the stacked views of Figs. 9, 10, 11, 12, and 13, small rectangular green artifacts appear in a repeated step-like pattern throughout the dataset. Some of these fall within the 2–8 m bottom-referenced EI depth range and are visible on the mosaic grids in Figs. 2 and 6, typically as elongated across-track anomalies. One such artifact is shown in fan view in Fig. 8. A strong, horizontal central-beam echo is visible, with a radiating sidelobe in the outer beams. After processing (Fig. 8b), the sidelobe is effectively removed, though again slightly overcorrected, while the central beam echo remains. This artifact pattern is most

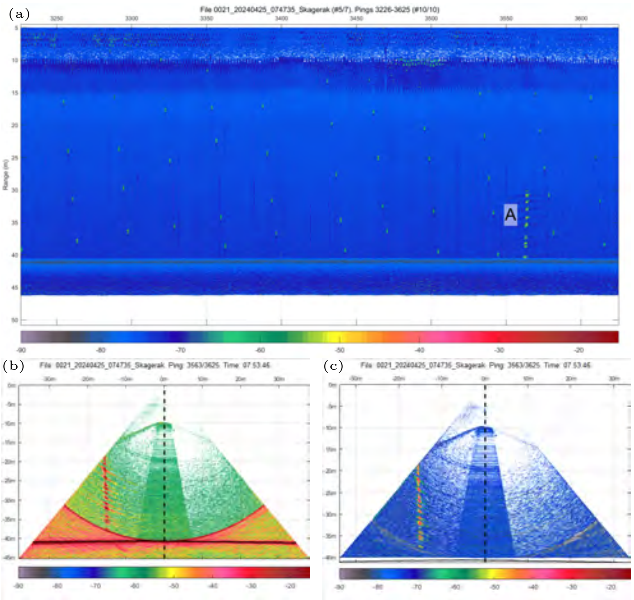

Fig. 9: Seep A from Fig. 6; one of the most discernible seeps in the set, even for the unprocessed data. Shown in (a) stacked view as well as fan view (b) before and (c) after processing.

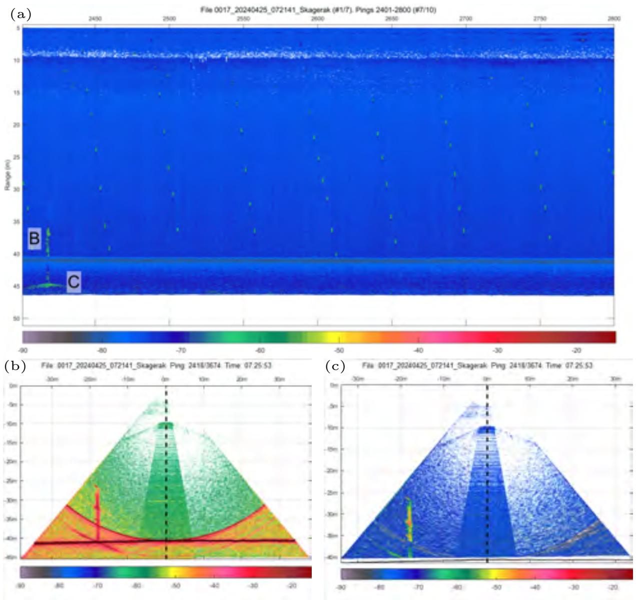

Fig. 10: Typical cohesive vertical nature of a gas seep flare (marked as B in Fig. 6.) seen before and after processing of the water column data. Also visible is the acoustic anomaly C, a sidelobe induced artifact from the strong response of the seep. Shown in (a) stacked viewed as well as fan view (b) before and (c) after processing.

likely impulse noise caused by interference from another echosounder, as suggested by the regular step-like pattern in stacked views, consistent with examples in Hughes Clarke, 2006, and Ryan et al., 2015.

4.2 Detected Gas Seeps

Several acoustic anomalies interpreted as gas seeps were identified in the Byfjorden dataset. These seeps exhibited a range of morphologies and intensities in both the fan and stacked views, as well as varying degrees of visibility on the echo-integrated grids. In total, 24 out of 30 identified seeps were clearly visible on the EI grids, while the others were discovered from inspection of the stacked views. 14 non-seep anomalies (e.g. fish or noisy artifacts) were visible on the EI grids and ruled out first after manual ping inspection, based on morphology and/or motion pattern. The following examples illustrate different types of seep responses and the role of preprocessing and integration parameters in their detectability.

Seep A (Fig. 9) is one of the most acoustically prominent seeps in the Byfjorden dataset, exhibiting a strong and easily recognizable response in both raw and processed water column data. Unlike a smooth, continuous flare, the seep appears as a discontinuous vertical stream of bubble-like reflections, suggesting either intermittent bubble release or clustering of bubble "packages". Despite its segmented appearance, the vertical alignment and intensity of the returns makes it unambiguous as a seep feature. It is clearly visible in both the fan and stacked views, at least inside the MSR, and serves as a useful reference point for the interpretation of weaker or more ambiguous anomalies in the dataset.

Seep B, shown in Fig. 10, exhibits the classic columnar appearance of a gas flare. Adjacent to it is a secondary anomaly (C) that also appears on the EI grid (see top right panel of Fig. 6). The anomaly is consistent with a sidelobe induced artifact resulting from the strong acoustic return of the primary flare. Adjusting the lower bound of the bottom-referenced EI depth window upward from the current 2 m level would likely have excluded this artifact from the gridded output. The seep looks "cut" approximately at the minimum slant range. This phenomenon, caused by the SRSN algorithm, is also noted by Schimel et al., 2020, and is due to the sidelobe artifact being stronger than any other overlapping signal from the seep at the MSR.

Seep D, depicted in Fig. 11, represents a more subtle case. It is barely discernible in either the stacked or fan views due to its limited vertical extent, making it particularly difficult to identify when manually reviewing thousands of pings. Nonetheless, it stands out clearly on the EI grid, underscoring the value of echo integration for enhancing the detectability of faint or compact features. Notably, increasing the lower bound of the integration window, an adjustment previously considered to exclude anomaly C, would likely have caused Seep D to be omitted as well, demonstrating the challenging nuance of setting these parameters effectively.

How variations in vertical gridding parameters influence seep detectability is further highlighted in Fig. 12, which presents two seeps with differing vertical distributions. Seep E is confined to the upper 25 meters of the water column and does not appear on the EI grid due to falling outside the selected integration depth. Seep F, in contrast, extends from the seafloor and throughout the entire water column, making it clearly visible on the EI grid as seen in Figs. 2 and 6.

Seep G (Fig. 13) offers another instructive example. Although it is a clearly defined feature in the fan view, it lies outside the 30° innermost beams defined in the

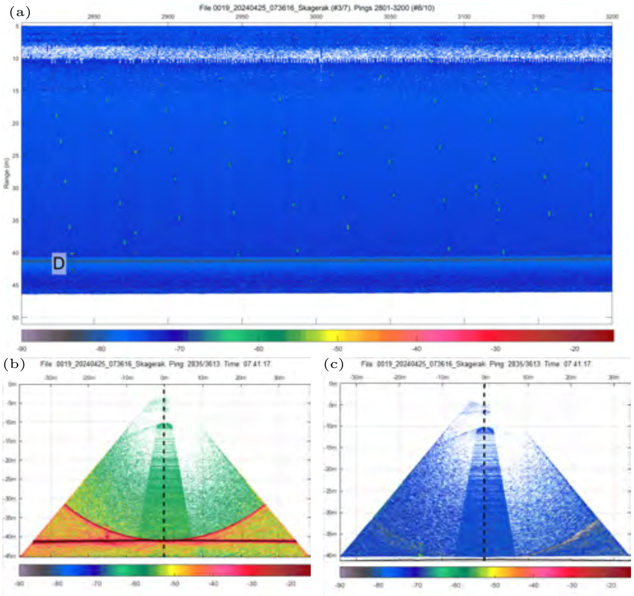

Fig. 11: Seep D, a minor seep that could be easy to miss (or hard to interpret) in the fan view ((b), (c)) when manually going through thousands of individual pings, or when looking at the stacked view in (a). It does however clearly show up on the EI grid in Fig. 6.

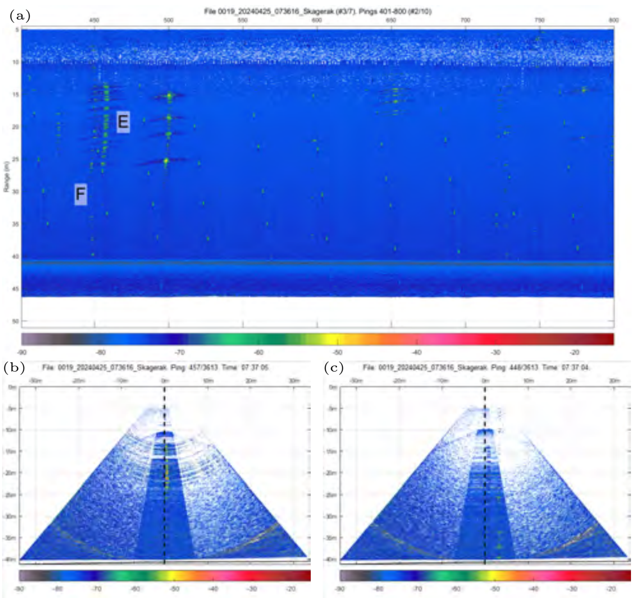

Fig. 12: (a) Seeps E and F in stacked view, (b) Seep E in fan view and (c) Seep F in fan view. E is only visible in the upper 25 meters of the water column, making it unidentifiable on the EI grid in Fig. 6, while F shows up as a vertical stream of bubble-like targets from the seafloor all the way up through the water column.

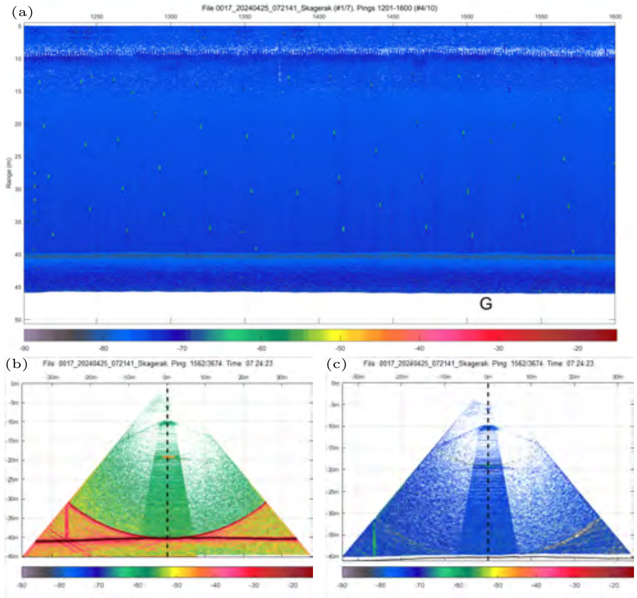

Fig. 13: Seep G, a cohesive seep that happens to be outside of the angular bounds needed to show up in the stacked view. The stacked view in (a) is marked with a **G** at the ping range where G would have showed up if a wider angle range for the stacked view was used. However, it clearly appears on the EI grid in Fig. 6. (b) and (c) shows the fan view before and after processing respectively.

display settings for the stacked view for this project. However, it is readily visible on the EI grid, reinforcing the benefit of combining different viewing perspectives during analysis. Detection methods that completely disregard the typically noisy data outside of the MSR (e.g. Urban et al., 2017; Zhao et al., 2017), would have completely missed this seep.

5 CCS Study Area: Southwestern Baltic

As part of a national Government Assignment to evaluate the potential for geological carbon storage in Sweden, the Geological Survey of Sweden (SGU) was tasked with identifying and assessing candidate offshore areas for CCS suitability (Andersson et al., 2023). Two primary regions in the Baltic Sea were selected based on geological and geophysical data: one south/southeast of Gotland and one south/southwest of Skåne. This report focuses on the latter region (Fig. 14), located in the southwestern Baltic Sea in the Arkona Basin, where the presence of several known fault zones adds complexity and makes gas seep detection an essential part of the preliminary site assessment.

As detailed in the latest Government Assignment progress report from SGU (Andersson et al., 2025), recent core drillings have confirmed the presence of a glauconite-bearing sedimentary unit in the Skåne region, known as the Arnagergrönsand, situated at a depth of approximately 1250 meters. This unit has been identified as a potential reservoir and consists of different lithologies of glauconitic sand, sandstones and

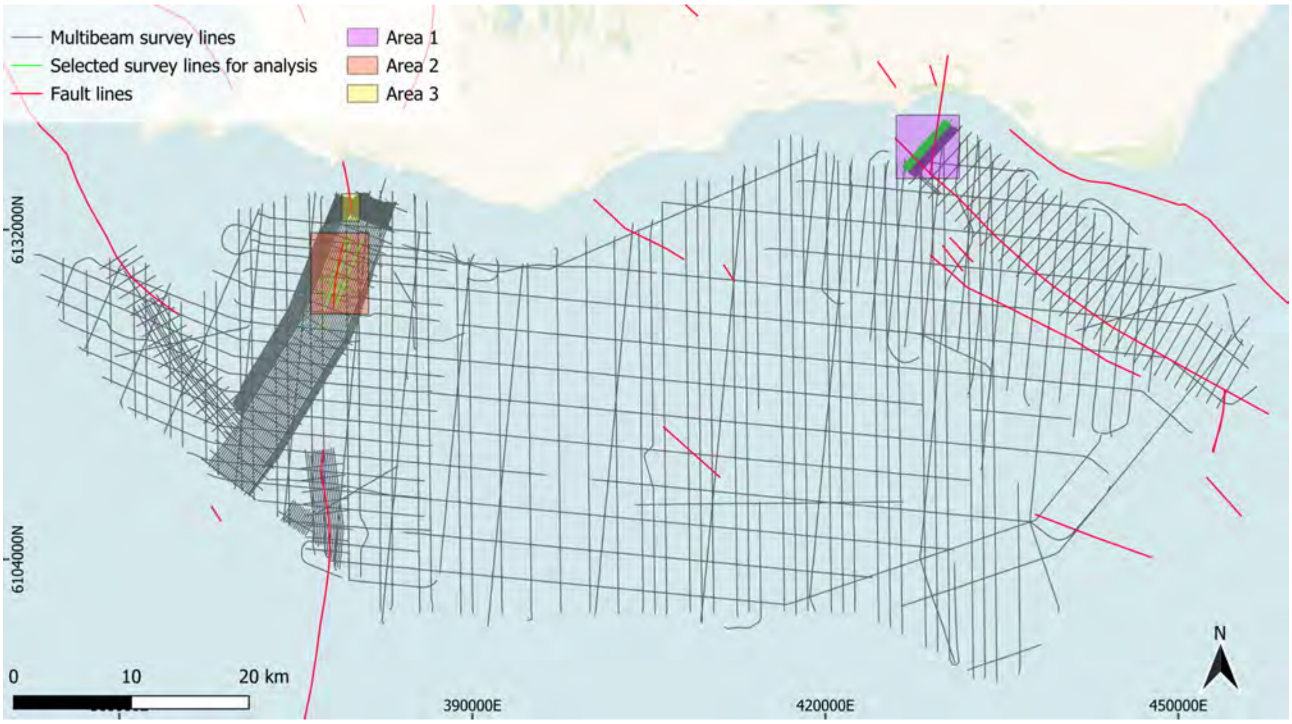

Fig. 14: Map over the CCS project area in the southwestern part of the Baltic Sea, just off the southern coastline of Skåne, Sweden. Marked on the map is all the MBES survey lines from 2023-2024, along with the documented fault lines. Also highlighted are the three sampled areas investigated in this report. Coordinate system: SWEREF99

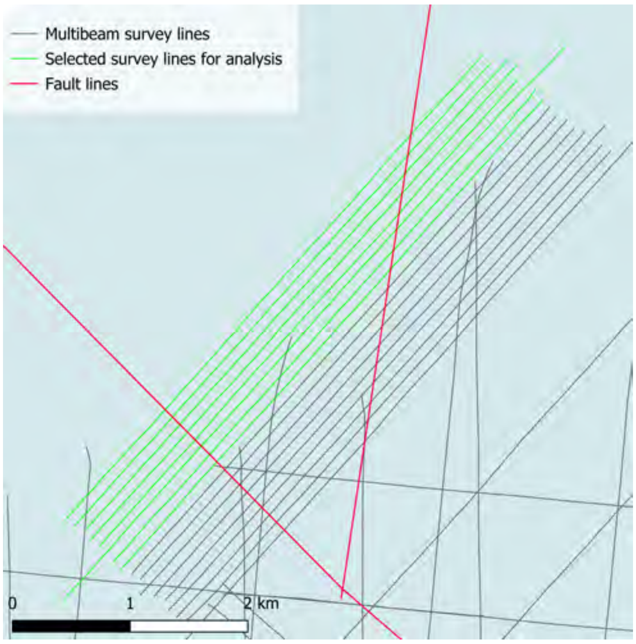

Fig. 15: Overview of Area 1, with selected lines for analysis highlighted in green.

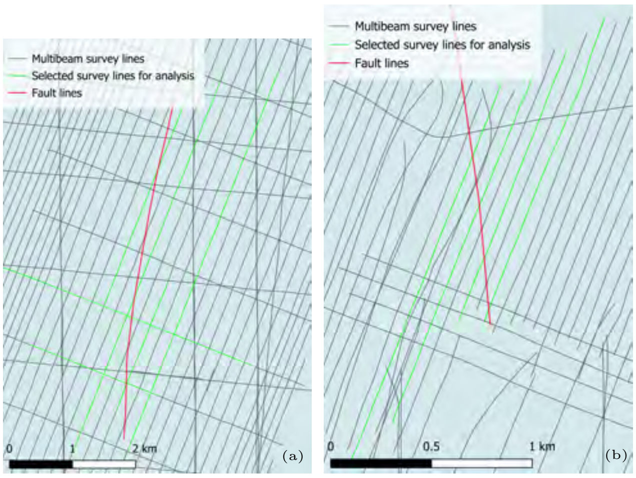

Fig. 16: Overview of (a) Area 2 and (b) Area 3, with selected lines for analysis highlighted in green.

mudstones with varying grain sizes and carbonate content. Reservoir properties range from relatively poor to very good, depending on porosity and permeability, with the lower half of the Arnagergrönsand deemed to have the most promising characteristics. Overlying the reservoir is a ∼40-meter thick layer of fine-grained, partially silicified limestone, topped by ∼30 meters of interbedded limestone and carbonate-rich mudstone, judged to act as a satisfactory caprock. Together, these stratigraphic units provide promising structural and lithological conditions for CO_2 sequestration, though it should be noted that reservoir thickness and properties may vary across the region.

In addition to suitable porosity and permeability, the high glauconite content of the Arnagergrönsand makes it particularly attractive for long-term mineral trapping. Glauconite is a cation-bearing silicate mineral with demonstrated potential to facilitate mineral carbonation reactions, allowing injected CO_2 to form stable carbonate minerals such as siderite ($FeCO_3$) (Q. Zhang and Tutolo, 2022).

Due to the prominence of fault zones in the area and their potential to act as migration pathways for injected CO_2, SGU initiated extended marine geophysical surveys during 2023 and 2024, with additional work planned for 2025. These surveys included seismic profiling to map fault structures and stratigraphy, as well as multibeam echo sounding to collect bathymetry, seafloor backscatter, and water column backscatter. All MBES surveys were conducted by the research vessel *Ocean Surveyor* (Sveriges Geologiska Undersökning, 2025) with a Kongsberg EM 2040 Dual Rx system, configured for a wider swath angle than for the Byfjorden test dataset, to increase area coverage per survey line.

In total, more than 1700 MBES lines of water column data were collected across the region in 2023 and 2024, with each raw file typically ranging from 3 to 3.5 GB in size. This represents an immense dataset that is impractical to analyze manually using traditional fan view inspection alone. For this thesis project, a representative subset of 33 lines, less than 2% of the full dataset, was selected to evaluate Espresso's echo integration capabilities for gas seep detection. These lines were picked from three sub-areas, each positioned over mapped fractures. The lines in Area 1 (Fig. 15) were surveyed on 13 April 2024, while the lines in Area 2 (Fig. 16a) span multiple survey dates in April and June 2024 (17/4, 18/4, 22/4, 24/4, and 14/6). The lines comprising Area 3 (Fig. 16b) were recorded on 13 June 2024.

6 Results

6.1 Background Artifacts and Non-seep Anomalies

The Kongsberg EM 2040 used in this survey is a multi-sector MBES system, meaning that its acoustic swath can be divided into distinct transmit sectors. As described by Hughes Clarke, 2006, this technique improves survey efficiency and data quality by enabling wider swath coverage by reducing the intensity of the specular sidelobe artifacts in the outer sectors. However, it also introduces visible boundaries between sectors, or sector transitions (Nau et al., 2025), which become apparent in water column returns. These transitions were not visible in the more narrow swath of the Byfjorden dataset, but a three-sector division becomes clearly discernible in the Skåne data due to its wider angular coverage.

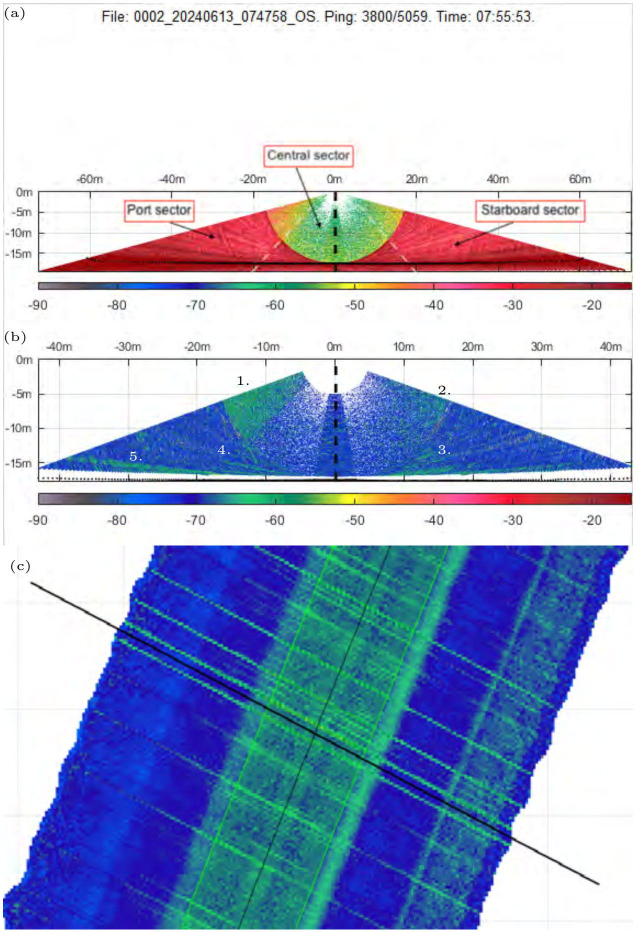

Fig. 17: Typical background noise for the Skåne dataset, (a) before and (b) after processing. The white dashed lines in (a) denote the sector transitions and were added for visual clarity. Five main artifacts remain after processing; **1.** Typical outer beam noise inside the MSR in the port sector. **2.** A less pronounced but similar outer beam noise in the starboard sector. **3.** Typical sidelobe induced artifacts outside the MSR on the starboard side of the central sector. **4.** Weaker but similar sidelobe induced artifacts outside the MSR on the port side of the central sector. **5.** Near-bottom sidelobe artifact in the port sector. The survey vessel is traveling towards the southwest in the Espresso map view (c), where the across-track black line indicates the ping in question. Example is from Area 3.

These sector transitions are apparent in Fig. 17, which shows a representative ping of the typical background noise for the Skåne dataset, both before and after processing. Although much of the background clutter is reduced by the radiometric correction and SRSN filtering, several artifacts remain in the processed ping (Fig. 17b). Artifacts **1.** and **2.**, located within the MSR in the port and starboard sectors respectively, illustrate typical outer beam noise (e.g., Nau et al., 2025). These are not effectively addressed by the SRSN algorithm, which is designed to correct for range-dependent patterns (see Section 2.6), but will leave more beam-dependent anomalies such as these largely intact.

Artifacts **3.** and **4.**, outside the MSR in the central sector, are sidelobe induced echoes that remain partially uncorrected. While SRSN is designed to suppress such range-dependent features, the sidelobe returns in the central sector are stronger than those in the outer sectors (as seen by the more intense red returns outside the MSR in Fig. 17a). Because the multi-sector configuration is intended to reduce sidelobe interference specifically in the outer sectors, the average signal used for normalization at each slant range beyond the MSR, is biased by the cleaner outer beams. This may have caused some of the central sector returns to persist.

Artifact **5.**, a near-bottom reflection in the port sector, does not appear fully range-dependent and may stem from exaggerated sidelobe returns at the seafloor in this wide-swath configuration, making it difficult for the SRSN algorithm to filter.

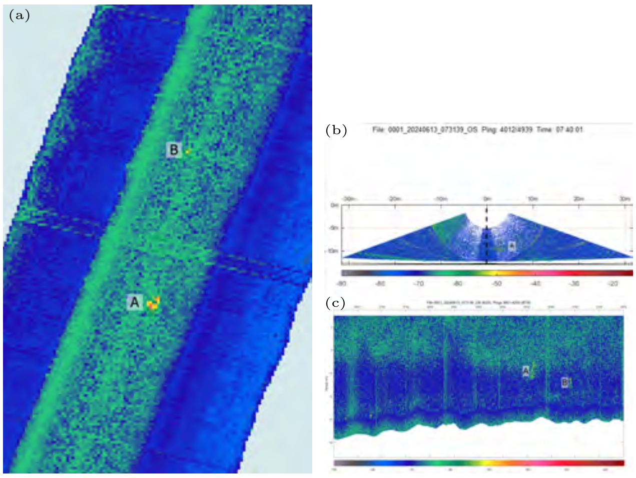

Fig. 18: Example from Area 3 showing that acoustic targets still can show up clearly on the EI grids, despite the noisy background of the WCD.

Overall, these artifacts illustrate some limitations of Espresso's SRSN filter when applied to multi-sector MBES data. While the multi-sector configuration improves performance in the outer beams, it introduces a sector-dependency to the signal returns that undermines the assumption of uniform range-dependence central to the SRSN approach. Nevertheless, strong anomalous targets in the water column still appear to remain distinguishable on the EI grids despite this background clutter, as demonstrated in Fig. 18.

A separate recurring anomaly is also present in the Skåne dataset, characterized by short-lived spikes of noise, typically spanning one to three pings, that appear orthogonal to the track lines in the EI grids and as thin vertical lines in stacked views. These anomalies occur across a range of depths and survey areas but vary in frequency and extent. Fig. 19 shows an example, highlighting the noisy ping in both unprocessed and processed fan views, along with its corresponding appearance on the EI grid. In the unprocessed fan view, this artifact dominates the central beams, though its full extent is difficult to determine due to overlapping sidelobe noise outside the MSR. The observed orthogonal pattern in the EI grids likely arises from the way SRSN applies its range correction. After normalizing by range, the algorithm reintroduces a reference level calculated from the central-most beams, assumed to be the cleanest. When these beams are instead dominated by noise, the reference level contaminates the entire ping, reinforcing the artifact across the swath and creating a prominent across-track band on the EI grid.

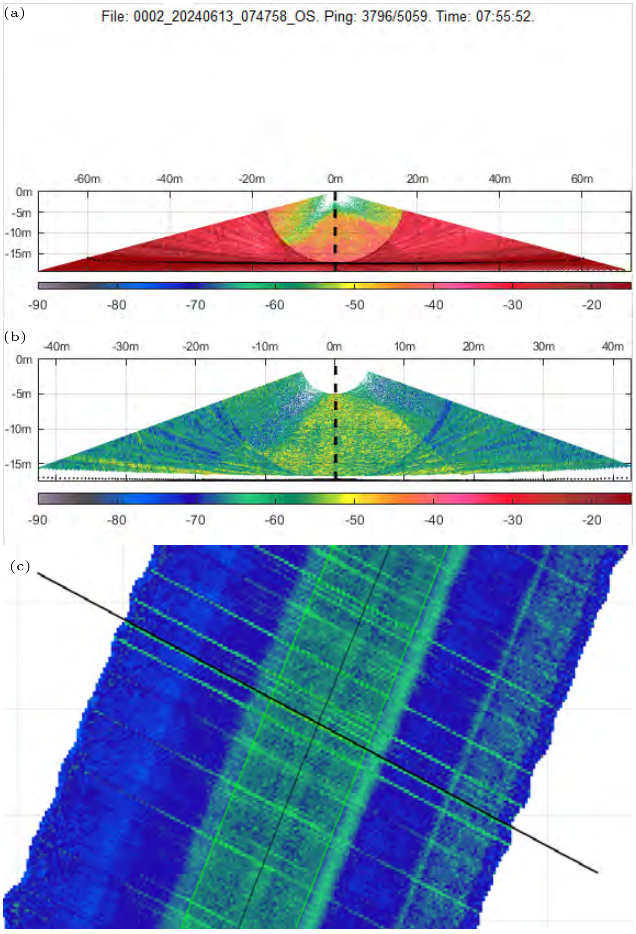

Fig. 19: Example of one of the very noisy pings, here from Area 3, (a) before and (b) after processing. These pings show up as prominent across-track lines orthogonal to the vessel direction on the echo integrated grid (c).

The origin of this artifact remains uncertain. It differs notably from the third party sonar impulse interference seen in the Byfjorden dataset (Section 4.1), which manifested as more regular step-like patterns. One possibility is transient acoustic interference from external acoustic sources or onboard electronics, though the exact cause cannot be confirmed in the scope of this study.

Another class of artifacts observed throughout the Skåne dataset are near-bottom anomalies likely caused by along-track sidelobe interference, particularly in areas with high bathymetric variability or from scattered

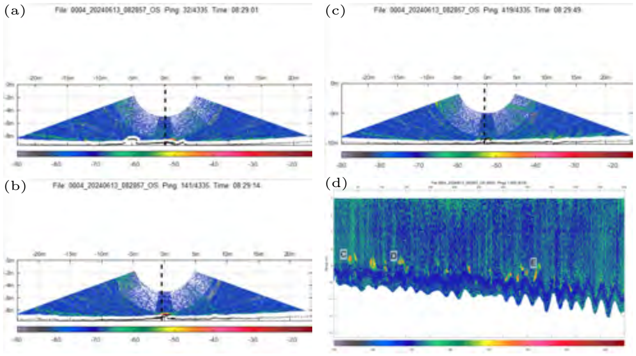

Fig. 20: Examples of near-bottom artifacts from Area 3, likely caused by along-track sidelobe interference caused by the dynamic seafloor topography. Fan views in (a)–(c) show high-intensity returns just above seafloor elevations, while (d) shows the corresponding stacked view with marked artifact locations (C–E), along a wavy and topographically complex bottom.

boulders on the seafloor. These artifacts are consistent with those described by Nau et al., 2018, where complex seafloor topography or hard, protruding targets reflect transmit sidelobes back into the sonar, resulting in strong acoustic returns just above the bottom creating characteristic artifacts.

Fig. 20 shows several examples from Area 3. The fan views display high-intensity returns positioned directly in relation to seafloor elevations. As this data was processed with an 0.5 m above-bottom mask (see Section 3.2), their apparent position in the water column exceeds that threshold. Fig. 20d, a stacked view covering the same region, highlights the prevalence of these anomalies in areas with undulating bathymetry. Some examples, including Artifact E, is also available to view as GIF animations at the project GitHub. The animation reveals the artifact transitioning from a free-floating anomaly to one recognized as bottom by the automatic bottom detection in Espresso as the vessel passes over it. This behavior further supports the interpretation that these anomalies stem from sidelobe returns misinterpreted above complex or sloping terrain.

Artifacts like these illustrate the risk of false positives when echo-integrating close to the seafloor, especially in rugged environments. Fig. 21 further emphasizes this point using a similar example from Area 1. The stacked view in Fig. 21a shows additional near-bottom artifacts across a less topographically dramatic, but still irregular, seafloor. Fig. 21b presents an EI grid generated using all processed data, with no vertical integration limits applied. Several of the near-bottom artifacts appear as bright, compact anomalies that could easily be mistaken for gas seeps. In contrast, Fig. 21c shows the result of echo integrating only the 2–8 meter interval above the seafloor, defined in Section 3.2. The cleaner appearance of this grid highlights the importance of setting appropriate vertical thresholds during gridding to avoid excessive manual review of non-seep anomalies.

A similar challenge arises when dealing with biological targets in the lower water column. Fig. 22 demon-

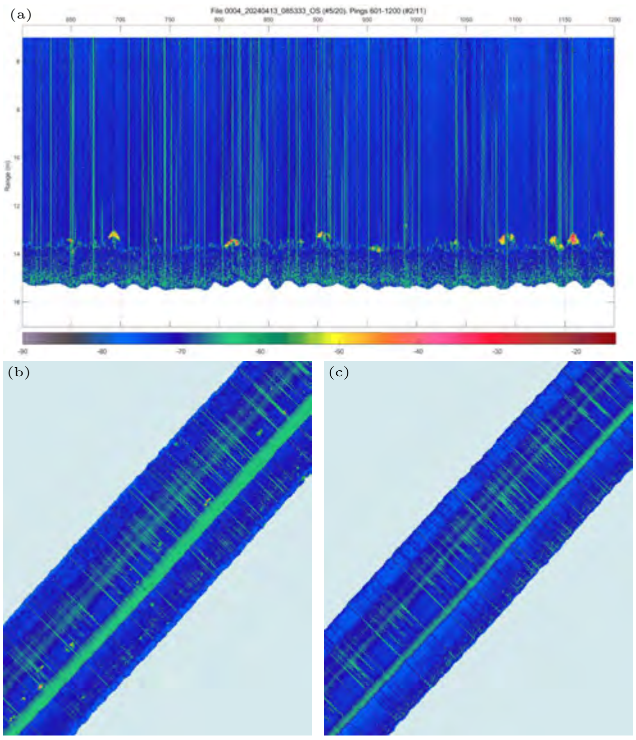

Fig. 21: Example from Area 1 highlighting the importance of excluding near-bottom data when creating EI grids. (a) Stacked view shows near-bottom artifacts likely caused by protruding features on the seafloor. (b) Gridding the full processed water column (no vertical masking) produces many bright anomalies. (c) Applying a 2–8 meter above-bottom integration window reduces false positives, resulting in a cleaner grid.

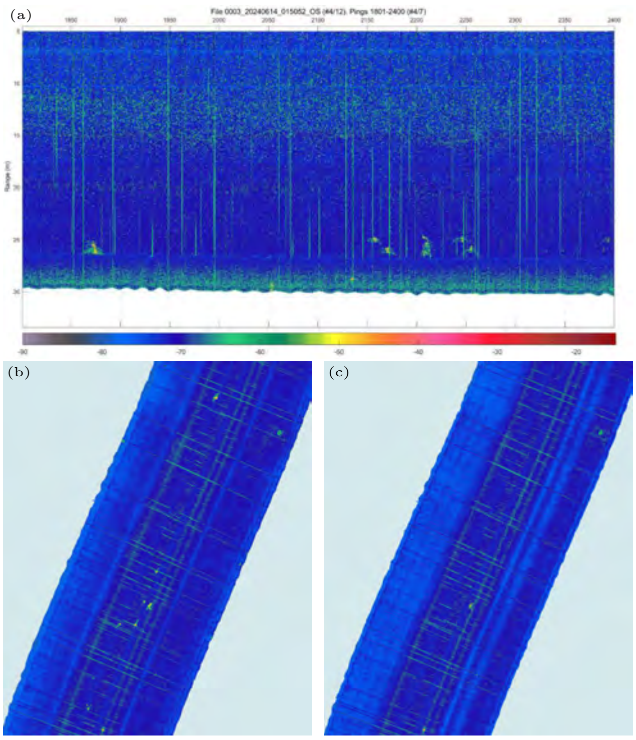

Fig. 22: Example from Area 2 showing fish-like targets just above the seafloor. (a) Stacked view reveals multiple low-lying targets. (b) EI grid using a 2–8 meter above-bottom integration window includes many of these as potential anomalies. (c) Increasing the lower limit to 3 meters removes most fish echoes, reducing the number of non-seep anomalies.

strates this scenario using an example from Area 2. The stacked view in Fig. 22a shows several small targets hovering roughly 1–2 meters above the seafloor, which likely correspond to individual fish or small schools. Some of these appear as anomalies on the EI grid in Fig. 22b, created using the default 2–8 meter integration window. When the lower bound of the integration range is increased to 3 meters in Fig. 22c, many of these fish-like targets are excluded from the final mosaic. These two examples illustrate the trade-off between thoroughness and efficiency: while a larger integration window increases the chance of detecting subtle seepage, it also introduces a greater number of irrelevant anomalies requiring manual inspection.

This section presents a selection of acoustic anomalies from the Skåne dataset that display some characteristics typically associated with gas seeps. However, none of these anomalies exhibit the clear and unambiguous flare morphologies seen in the confirmed seeps from Byfjorden (Section 4.2). For this reason, they are referred to here as ”seep-like” targets or ”possible seeps”, reflecting the uncertain nature of their interpretation (see Section 7.1 for further discussion).

These anomalies were identified through combined inspection of the echo-integrated grids, stacked views and fan views. If an anomaly was not deemed to have enough seep-like resemblance in one of these view-modes, it was omitted. The most prominent and ambiguous examples are presented and discussed below, grouped by the survey areas in which they were found (Areas 1–3). A complete index of all identified seep-like targets is included in Appendix A, including additional pings for the examples shown in this current section.

Given that the spatial and vertical extent of many of these anomalies is not easily discernible from a single ping, animated GIFs have been generated for each candidate seep. These animations are available at: github.com/vbacklin/marine_geo_thesis. They are highly recommended for readers seeking a clearer understanding of the temporal and spatial characteristics of each anomaly, and help to aid with interpretation. For each anomaly, two animation versions are available: **1.** A standard version that shows pings in chronological order, illustrating the real-time progression of the acoustic signal. **2.** A temporally reversed version, in which the sequence is played backwards. This perspective is useful in visualizing the potential plume structure by beginning at the presumed seafloor origin and following the upward trajectory of the target. However, because this reverse perspective can introduce interpretive bias, the forward-time version is provided alongside it for contextual balance.

6.2 Acoustic Anomalies with Seep-like Qualities

6.2.1 Area 1

Four acoustic anomalies identified in Area 1 exhibit characteristics consistent with possible gas seeps. These targets vary in morphology, strength, and degree of ambiguity. While none display the clearly defined flare shapes seen in the confirmed Byfjorden seeps (Section 4.2), several show coherent vertical structure or clustering patterns that warrant consideration. Fig. 23 shows the location of these possible seeps in relation to the fault lines, as well as an overview of the EI grids. The average distance between each seep-like target and the closest fault line, calculated with the ”Shortest line between features”-tool in QGIS, was 543 meters. Possible seep D was the closest target with a distance of 275 meters.

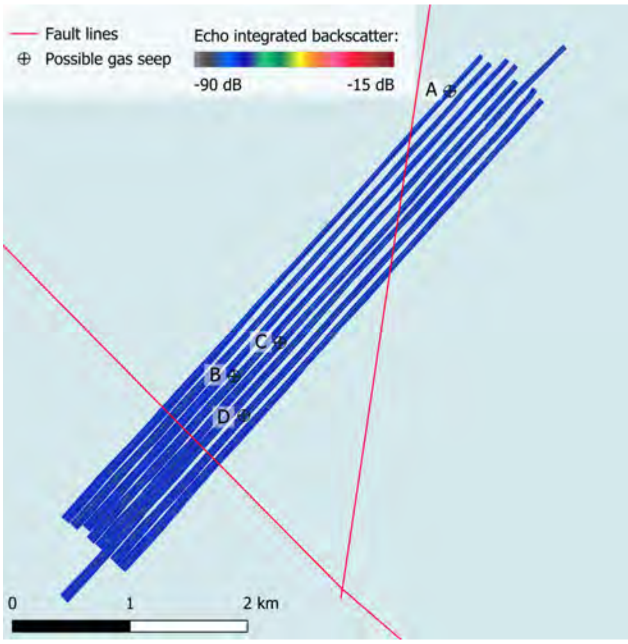

Fig. 23: Overview of the echo integrated grids created for Area 1, with labeled markers for any seep-like acoustic anomalies.

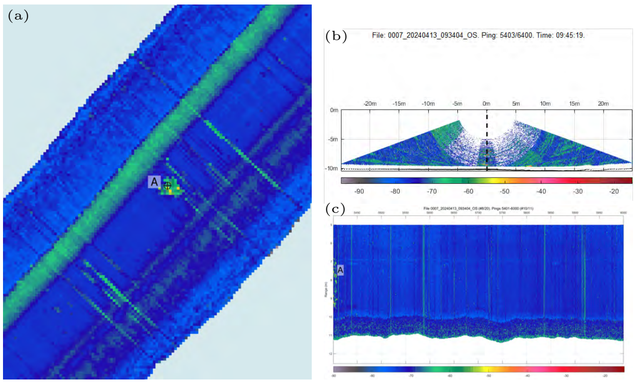

Fig. 24: Possible seep A in Area 1, as seen on the (a) EI grid, in (b) fan view and (c) stacked view. The stacked view shows a typical vertical structure that could be indicative of a gas seep. However, the structure does not look as cohesive as the typical flares seen in Section 4, instead looking more segmented as smaller targets in both stacked view and fan view.

Possible seep A (Fig. 24) presents as a vertically oriented anomaly on both the EI grid and in stacked view. While the general geometry resembles a rising plume, the signal is fragmented, appearing as a sequence of discrete targets rather than a cohesive flare. This segmented appearance is also reflected in the fan view and interpretation remains uncertain.

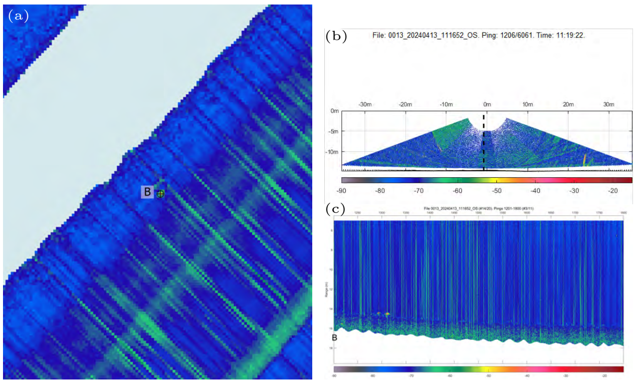

Fig. 25: Possible seep B in Area 1, as seen on the (a) EI grid, in (b) fan view and (c) stacked view. The fan view shows a small but cohesive and vertical flare shape. It is not visible in the stacked view as it is far outside the 30° beam range used to define the stacked view in Section 3.2.

Possible seep B (Fig. 25) appears as a small but cohesive and vertically aligned target with a strong backscatter response in the fan view. It is not visible in the stacked view due to its location outside the 30° beam range used for stacked view rendering (Section 3.2). Despite its limited extent, the shape and coherence make it a compelling candidate for a weak seep-like feature.

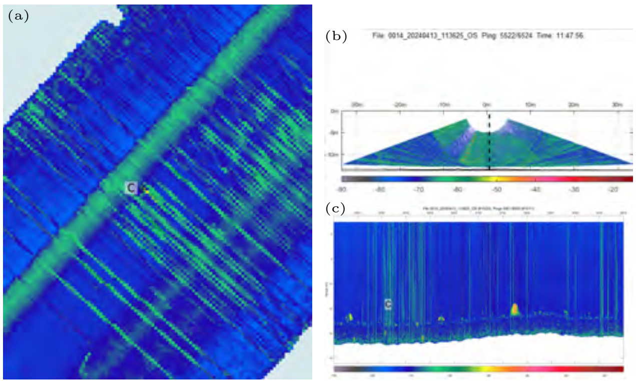

Fig. 26: Possible seep C in Area 1, as seen on the (a) EI grid, in (b) fan view and (c) stacked view. This anomaly does only show up in a single ping, and consist of regularly spaced targets, that could be interpreted as bubbles, traveling in what looks to be a perfect angled line towards the sonar. These facts would most likely indicate a digital artifact, and not a natural seep.

Possible seep C (Fig. 26) is visible in only a single ping, with a strikingly regular arrangement of evenly spaced reflections that align along a perfect diagonal path toward the sonar. While this may at first resemble rising bubbles, the regularity and single-ping duration strongly suggest a digital artifact rather than a physical phenomenon in the water column.

Possible seep D (Fig. 27) is a faint and narrow feature visible primarily in the central beams. It shows a slightly tilted orientation in the fan view and a subtle expression on the EI grid. Although its backscatter response is weak, the consistent structure across several pings supports its inclusion as a potentially interesting but low-certainty seep-like anomaly.

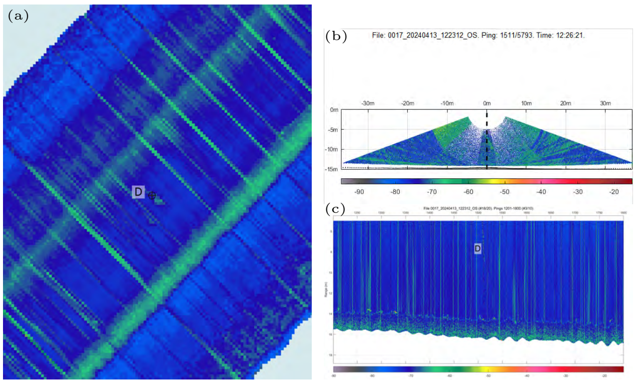

Fig. 27: Possible seep D in Area 1, as seen on the (a) EI grid, in (b) fan view and (c) stacked view. This anomaly exists in the central beams as a slightly angled flare with a relatively weak backscatter response.

6.2.2 Area 2

Fig. 28: Overview of the echo integrated grids created for Area 2, with labeled markers for any seep-like acoustic anomalies.

Area 2 contains the largest number of seep-like anomalies identified in the Skåne dataset, with a total of 13 candidates. Compared to the weaker and more compact anomalies observed in Area 1, many of the anomalies in Area 2 appear significantly more pronounced in both the stacked and fan views. These features often span greater vertical and horizontal extents, producing clearer and more coherent shapes on the EI grids, side-stacked views and individual pings.

A consistent challenge with interpreting these anomalies is their inclined geometry. Several targets extend across multiple pings and are heavily tilted away from the vertical axis, particularly toward the northwest. While this may suggest current-influenced gas plumes, it also complicates the interpretation, as schools of fish or other mobile biological targets could feasibly generate similar trajectories. Notably, the orientation is not random as many of the larger, more striking flare-shaped anomalies in Area 2 share the same general inclination, with only a few, less defined targets deviating from this pattern. This issue is explored further in Section 7.1.

Area 2 also differs from the other regions in terms of overall data quality. The WCD here appears less noisy, likely due to the greater water depths (25–30 m) and relatively smooth seafloor, compared to the more complex bathymetry and shallow conditions of Areas 1 and 3, although some of the static background artifacts from Section 6.1 still persist.

Figure 28 provides an overview of the results in Area 2, with all 13 seep-like targets marked on the EI grids and their proximity to the fault lines. A subset of six of the most visually compelling and representative anomalies are described in detail below, with the remaining examples listed in Appendix A. The average distance between each seep-like target and the closest fault line, calculated with the "Shortest line between features"-tool in QGIS, was 971 meters. Possible seep J was the closest target with a distance of 295 meters.

Possible seep A (Fig. 29) is one of the more prominent anomalies in Area 2. In the stacked view, it appears as a vertically structured flare that broadens with height and shows a slight inclination toward the northeast. The fan views, however, reveal a more horizontally extended plume leaning strongly westward. Together, these perspectives suggest the anomaly is inclined toward the northwest, consistent with its position and shape on the EI grid. While visually distinct and spatially coherent, the pronounced inclination complicates its interpretation as a classic gas seep.

Possible seeps C and E (Fig. 30) represent two contrasting cases. Seep C is notable for deviating from the dominant inclination pattern in Area 2, appearing to rise toward the northeast. It also features a small, detached target approximately 6–7 meters above the main structure, adding to its ambiguity. In contrast, Seep E exhibits the more typical northwest-leaning geometry, consistent across the fan, stacked, and EI grid views. The differing orientations of these two anomalies, despite being found in relatively close proximity, hint at either variable local currents or non-seep origins for at least one of the targets.

Possible seep F (Fig. 31) stands out as one of the most distinctly flare-like anomalies in the entire dataset. The fan view reveals a well-defined plume extending diagonally upward and westward from the seafloor. The stacked view once again shows a north/northeast tilt, supporting the interpretation of a northwest-oriented plume. While visually compelling, the pronounced inclination again raises uncertainty as to whether the shape reflects a bubble plume influenced

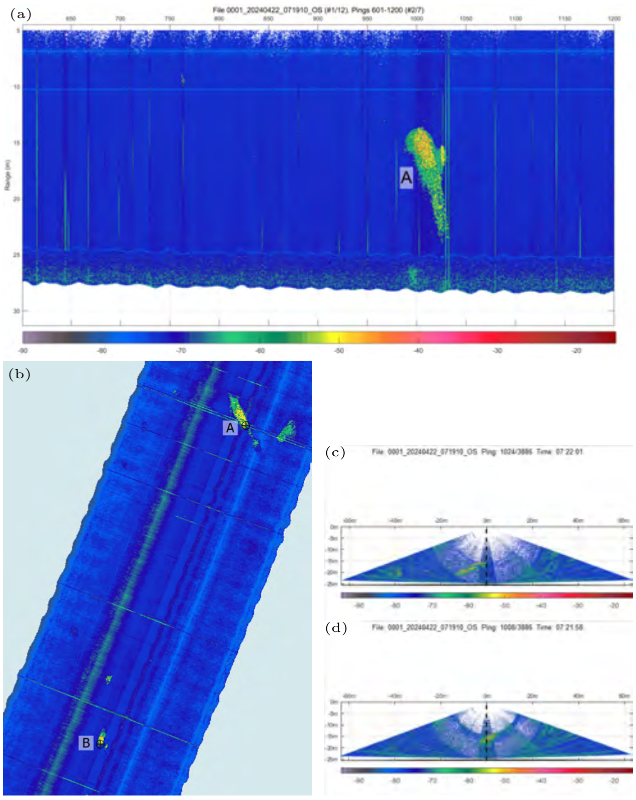

Fig. 29: Possible seep A in Area 2, as seen on; (a) stacked view, (b) EI grid and two different pings in fan view ((c) and (d)). The stacked view shows a characteristic flare shape that is leaning slightly toward north/northeast (as the ship is traveling south/southwest), while the fan views shows a westward direction that is more horizontally inclined than it is vertical. This indicates that the possible seep is heavily inclined towards the northwest, which lines up with what is seen on the EI grid, as the marker shows an approximation of the possible seep origin.

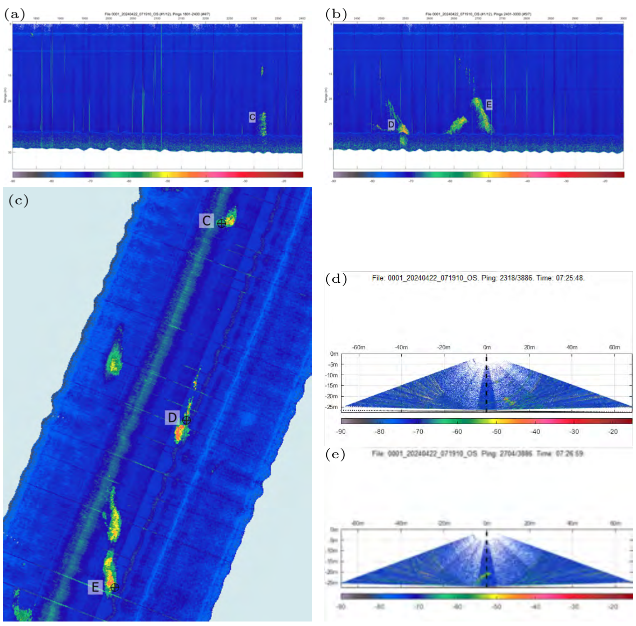

Fig. 30: Possible seep C in Area 2, as seen on; (a) stacked view, (c) EI grid and (d) fan view. The structure consist of a vertical flare (in stacked view) and a smaller separated shape about 6-7 meter above the main plume. This is one of very few possible seeps that seems to be angled toward the northeast. Possible seep E as seen on; (b) stacked view, (c) EI grid and (e) fan view. The characteristic flare shape seems to be angled towards the north/northwest, similar to several other anomalies in the area.

by current flow, or the lateral movement of a different type of acoustic target.

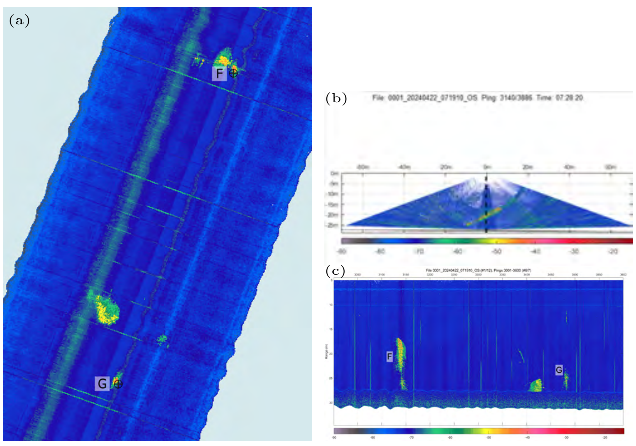

Fig. 31: Possible seep F in Area 2, as seen on; (a) EI grid, (b) fan view and (c) stacked view. One of the most striking flare shapes from Area 2, especially in fan view. Similarly to possible seep A in Fig. 29, we can see the stacked view showing a slight inclination to the north/northeast and a heavy inclination to the west in the fan view, indicating a northwestern inclination.

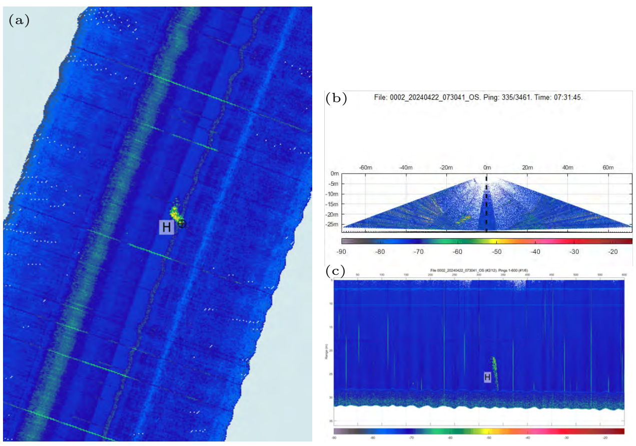

Fig. 32: Possible seep H in Area 2, as seen on; (a) EI grid, (b) fan view and (c) stacked view. The stacked view shows a very typical flare shape of a relatively small possible seep. The fan view and EI grid indicates the typical northwestern inclination seen throughout the area.

Possible seep H (Fig. 32) is smaller in scale but displays a clean, vertically structured shape in the stacked view, with a slight north/northeast tilt. The fan view reveals the typical westward inclination, making the overall orientation of this minor seep-like target consistent with the general northwest trend observed throughout Area 2.

Possible seep K (Fig. 33) is among the more ambiguous anomalies. Initially, it presents a plume-like structure rising from the seafloor, resembling the other northwest-leaning anomalies described above. However, as the ping sequence progresses, the structure transitions downward, behavior that is atypical for gas plumes. This unusual movement suggests either a secondary biological target that happen to coincide with the main plume, or a single target exhibiting complex motion, such as a school of fish traversing the water column in an irregular pattern, without any actual seepage present.

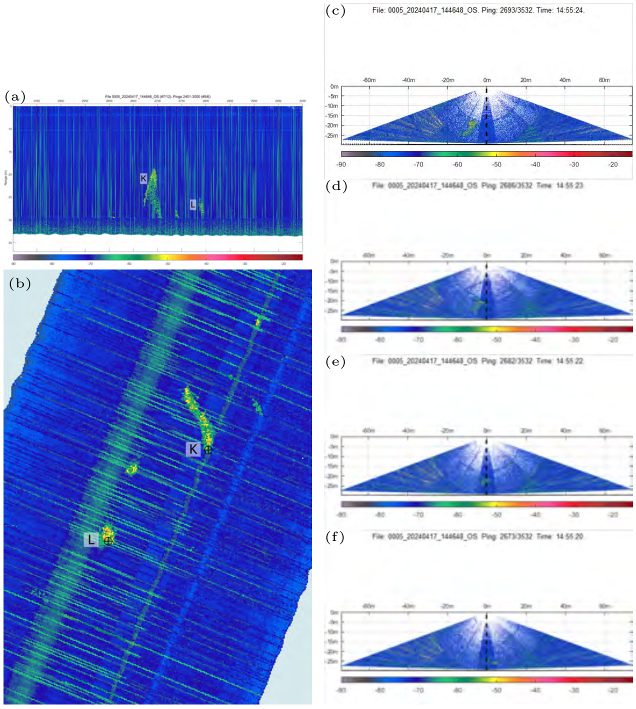

Fig. 33: Possible seep K in Area 2, as seen on; (a) stacked view, (b) EI grid and four different pings in fan view (c), (d), (e), (f). Tracking the movement from the interpreted origin of the possible seep, we first see a characteristic flare shape rising with the typical inclined northwestern direction for Area 2. The movement then shifts downwards without the typical flare shape. Note that the order of the pings is reversed in a temporal sense, to get a better sense for the possible seep morphology, starting at the origin.

6.2.3 Area 3

No seep-like acoustic anomalies were identified in Area 3. Compared to the other regions, the water column data here is noticeably noisier, likely due to the combination of shallow water depths, highly dynamic bathymetry, and the wide swath angle used during data acquisition. Figure 34 provides an overview of the EI grids from this area, highlighting the lack of distinct flare-like structures.

7 Discussion

7.1 Interpretation of Acoustic Anomalies

In evaluating the acoustic anomalies detected in Area 2, a central question arises: do these features represent genuine gas seeps, or are they manifestations of biological activity such as schools of fish? The inclination, directionality, and acoustic morphology of these anomalies provide clues, but also introduce ambiguity. It is however important to note that gas seepage in this region would not be unexpected. Mathys et al., 2005, documented the presence of gas-rich near-surface sediments in the Arkona Basin. While their study area does not overlap directly with the dataset of this study, it nonetheless supports the possibility of natural seepage in this broader geological context.

Supporting the gas seep interpretation is the morphological structure of flare-like shapes, especially as seen in the stacked view throughout the area. When viewing the temporally reversed animations, several of these anomalies resemble gas rising from the seafloor. However, the strong horizontal inclination, commonly towards the northwest, observed in the fan view is less typical for seepage. Although there are examples of tilted or angled plumes in the literature (e.g., Nau et al., 2022, 2025; Rovere et al., 2020; Turco et al., 2022; Zhao et al., 2017, 2020), they are generally not as extremely inclined as those observed here, and often occur in much deeper waters, with plumes extending hundreds of meters in the water column. However, W. Zhang et al., 2022, documented a similarly inclined gas plume in 40-meter-deep waters of the South China Sea, as seen from their 3D point cloud reconstruction. In their case, the inclination was attributed to horizontal current flow deflecting the bubble stream. A comparable interpretation could apply here, although the hydrodynamic conditions in the southwest Baltic are likely quite different, making it difficult to draw conclusions without accurate water current measurements.

The most recent publicly available water current data for the region comes from the Stena Skåne Ferrybox (Id 38058) (SMHI, 2023). Fig. 35 shows the location of this current measuring buoy relative to Area 2. All WCD associated with these anomalies were collected in April 2024, but current measurements from the buoy are only available up to January 2023. Calculating the average flow direction for the most recent April data (i.e., April 2022; see Appendix C for the Python script used), yields an average direction of 290°, which aligns well with the northwestern inclination in the gas seep hypothesis. However, averaging all April measurements between 2019–2022 results in a mean direction of 240°, and some years exhibit nearly opposite trends, for example 123° in 2021, making these data unreliable as proxies for flow direction on the specific survey days in April 2024 due to their apparent variability. The buoy is also located approximately 10 km away from Area 2, and its measurements reflect only surface currents. The true direction at the 15–25 meter depths where the anomalies occur may therefore differ further, due to processes like the Ekman spiral (Ekman, 1905). Furthermore, the average current velocities, around 40 cm/s, may be insufficient to account for the degree of lateral displacement observed. However, the typical maximum velocities, which exceed 1 m/s, could perhaps generate such an effect. Table 1 summarizes surface current directions and velocities measured by the buoy for April between 2019 and 2022.

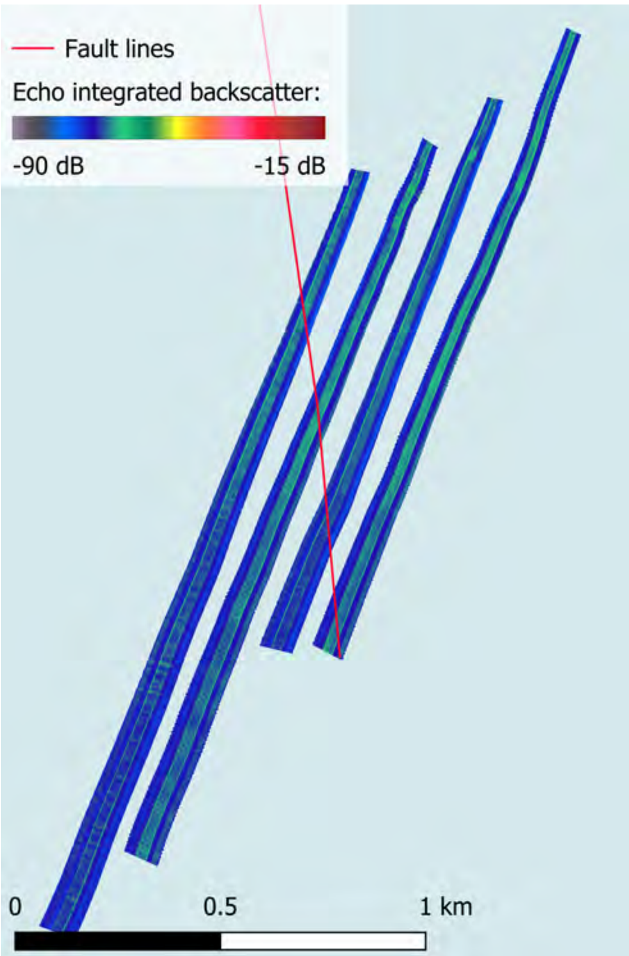

Fig. 34: Overview of the EI grids created for Area 3. No distinct seep-like acoustic anomalies were found.

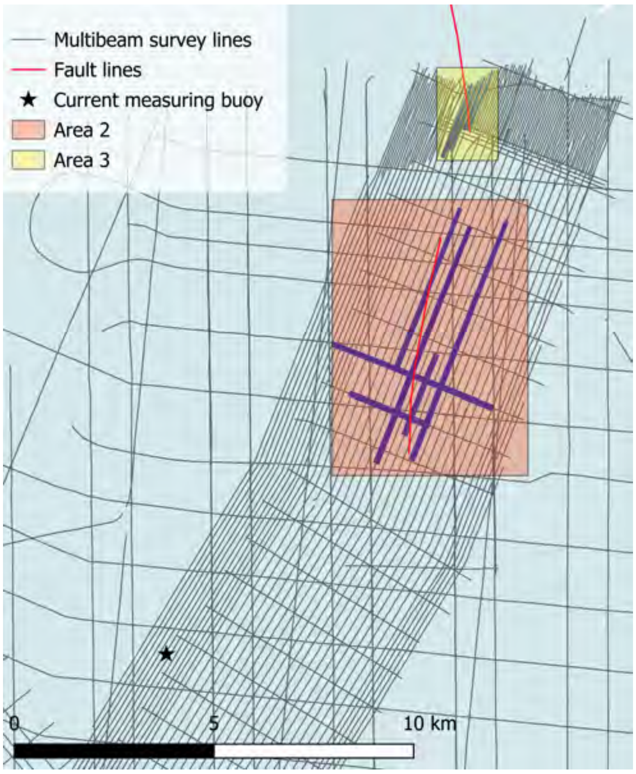

Fig. 35: Map showing the position of the current measuring buoy Stena Skåne Ferrybox (Id 38058) in relation to Area 2 and 3.

The possibility of biological origins for these anomalies cannot be dismissed. Herring (Clupea harengus), known for their schooling behavior and high abundance in the Baltic Sea (Havs- och vattenmyndigheten, 2023),

Table 1: Summarized surface current data from the Stena Skåne Ferrybox.

Time Period	Average Direction (°)	Average Velocity (cm/s)	Median Velocity (cm/s)	Maximum Velocity (cm/s)	Avg. Velocity-scaled Vector Direction (°)
April 2019	266	42	41	132	266
April 2020	138	41	39	168	125
April 2021	123	36	34	106	132
April 2022	290	40	38	106	189
April 2019 - 2022	240	40	38	168	225

are a plausible explanation. Herring are known to be vessel avoidant (De Robertis and Handegard, 2013), which could account for the downward movement seen in the temporally forward animations. Further supporting a biological interpretation is the observation that not all anomalies rise toward the northwest; if the anomalies were due to gas seeps, consistent current flow would likely produce more uniform orientations for targets in close proximity.

Another possible explanation is that some anomalies may represent interactions between biological targets and active seepage, potentially altering the morphology and acoustic signature. This could be the case for Seep K, which initially presents as a typical northwest-leaning flare but then appears to descend in subsequent pings. While methane cold seeps have been shown to attract biological activity in deep-sea environments (e.g., Åström et al., 2018), no such findings have yet been confirmed in shallow, more productive waters like these.

It is also worth noting that not all anomalies need to share a common origin. Despite certain visual similarities, it is entirely plausible that some are true gas seeps while others result from biological activity. For instance, the more prominent flare shapes such as A, E, F, G, H, and I may represent gas seeps, while more ambiguous anomalies like B, C, D, J, K, L, and M could be attributed to biological targets.

In summary, the data presented in this study, along with the author's limited experience in WCD interpretation, have not allowed for a conclusive classification of these acoustic anomalies.

7.2 Evaluation of Espresso as a Tool

Espresso offers several important benefits, particularly in terms of time savings and early-stage anomaly filtering, features that become especially valuable when working across large spatial areas. Despite challenges with interpretation and occasional data quality issues, this study demonstrated multiple cases where the echo-integrated grids revealed seep or seep-like anomalies that could easily have been missed using only fan or stacked views. This highlights the strong potential of echo integration as a detection tool for gas seeps. The software is user-friendly and delivers impressive sidelobe noise filtering, particularly notable given that Espresso is free and open-source. This filtering significantly reduced visual clutter and made interesting targets more identifiable. However, portions of seep-like structures that extended outside the MSR were sometimes lost, obscuring their apparent seafloor origin. This was especially noticeable for the more inclined targets in Area 2. It is unclear whether this is due to the SRSN algorithm itself or to the fact that sidelobe noise outside the MSR overpowered the original signal entirely.

The addition of some more features could further improve Espresso's usability and scalability. For instance, the ability to export fan or stacked views directly as PNGs, without relying on screenshots, would make documentation easier. Additional batch processing options would also be valuable, particularly for gridding. Currently, memory limitations restrict how many lines can be loaded and gridded at the same time. A batch function capable of loading, gridding, mosaicking, exporting (as GeoTIFF), and unloading one line at a time would make it possible to echo integrate an entire folder overnight. Another useful feature would be the ability create stacked fan views, i.e. averaging the along-track backscatter for a set amount of pings. This would be especially beneficial in situations where full flare shapes stretch over multiple pings, like the larger structures of Area 2 whose animations needed 30-40 consecutive pings for proper visualization of morphology.

Choosing appropriate gridding parameters proved to be a nontrivial task, with a constant balance between thoroughness and efficiency. For broad-area pre-studies like this CCS assessment, where quantification of seepage is not the primary goal and minor biogenic seeps may be of limited interest, a narrowed vertical integration window may be preferred. For example, most seep-like targets in Area 2 would likely have been detected even if the echo integration window was reduced to 3–4 m above the bottom, significantly decreasing the number of gridded non-seep anomalies requiring manual review. Given that the 33 lines analyzed here represent less than 2% of the full dataset, a narrower integration window would be recommended for large-scale processing to achieve significant time savings.

Compared to professional and commercial software like FMMidwater or Echoview, Espresso does have some limitations. These include the lack of 3D visualization, reduced positional accuracy and potential compromises in data quality due to processing simplifications. The use of MATLAB also introduces performance constraints, as scripting languages are generally slower and less memory-efficient than compiled alternatives such as C++ (Ousterhout, 1998). This remains true despite the thoughtful performance optimizations within Espresso, such as the use of memory mapping to handle large data volumes (Schimel et al., 2024b).

8 Conclusions

Echo integration of water column data is a valuable technique for gas seep detection in large datasets. It is particularly effective during the early filtering stages of a study, offering a broad overview that can help prioritize where to focus more detailed interpretation efforts. For echo integration to be effective, background noise must be filtered out. This presents a challenge, as WCD is inherently noisy, especially due to sidelobe induced artifacts. While no commercial software (to my knowledge) currently offers MBES echo integration functionality, Espresso provides a free, open-source alternative with built-in sidelobe filtering. In this study, Espresso proved effective in many cases, but struggled with removing certain sidelobe artifacts for multi-sector data, as well as a subset of extremely noisy pings. The origin of this noise remains unknown, but its recurring nature and impact on data processing suggest it warrants further investigation. Understanding the cause, and how to mitigate it, will be important for improving future WCD analyses.

In the CCS project area, several anomalies with seep-like characteristics were detected, though their interpretation remains uncertain. Notably, the identified anomalies were not located directly above any mapped fault lines. The closest was approximately 275 meters away, with an average distance of 870 meters across all anomalies. The most seep-like anomalies (A, E, F, G, H, and I) were, on average, 1179 meters from the nearest fault. This spatial pattern suggests a likely biogenic origin from shallow sediments, rather than leakage from deeper geological structures. This interpretation is supported by previous studies reporting gas-rich near-surface sediments in the broader region (Mathys et al., 2005).

While such biogenic seepage may not indicate a risk for CO_2 leakage in a CCS context, it is still important to characterize. Understanding the baseline presence of natural gas emissions is critical for effective post-injection monitoring, where distinguishing between leakage and natural seepage is essential. This study covered only a small fraction of the total CCS project area, and further work is needed to fully evaluate the risk of potential CO_2 leakage and overall CCS viability of the region.

9 Future Work

For the CCS project:

- Expand the creation of echo-integrated grids to additional fault lines in the broader fracture zones. This would help efficiently prioritize areas for more detailed manual analysis ahead of final assessments regarding the viability of the Skåne region as a potential CCS site.
- Conduct further analysis of the ambiguous seep-like anomalies using professional tools such as FM-Midwater. Extracting the features like 3D point clouds may provide a clearer understanding of their origin.
- Integrate a broader range of oceanographic data, such as current velocity and direction, and biological habitat distributions, to support interpretation and help distinguish between gas seeps and biological targets. Findings should also be compared with other geophysical data, such as marine seismic data and sub-bottom profiles.

For gas seep detection:

- This study has demonstrated the value of combining echo integration with effective noise filtering. Further development of advanced filtering approaches, such as those proposed by Zhao et al., 2020, Weber, 2021, and Nau et al., 2025, holds great potential to enhance seep detection and quantification when used in conjunction with echo integration. Whether this progress will occur through expanded filtering functionality in Espresso, or by commercial software adopting similar techniques, remains to be seen.
- As seen in Section 6.1, the current SRSN algorithm in Espresso struggles with multi-sector WCD, due to differing sidelobe behavior across sectors. One potential improvement would be to allow users to define sector transitions by beam angle, unless some clever algorithm can be developed to identify the transitions automatically. This would enable SRSN filtering to operate independently within each sector, where sidelobes should be more range-dependent. While speculative, this may offer a path toward better adaptation of the SRSN algorithm to multi-sector systems and could therefore improve sidelobe suppression in wider swath surveys, yielding cleaner data for echo integration.
- Emerging work on deep learning methods, such as the use of convolutional neural networks for gas seep detection (Hicks et al., 2023; Manjur et al., 2025), appears highly promising. It is this author's belief that such techniques will play an increasingly central role in the future of automated WCD target classification and detection.

10 Acknowledgements

First, I want to thank my supervisors, Christian Stranne (SU) and Francis Freire (SGU), for providing all the support and resources needed for me to complete this project. A sincere thanks goes out to Stefano Bonaglia at the University of Gothenburg for his interest in the project and for granting access to the Byfjorden dataset. I'm especially thankful to Daniel Stålnacke (SGU) for taking a chance on a bachelor student with a dream of contributing to the SGU Data Analysis team. Lastly, I extend my gratitude to Dr. Alexandre C.G. Schimel. Not only for developing Espresso as an open-source software, but for answering my novice-level email questions with such patience. This project would have been far more difficult without the incredibly detailed responses you provided, and I'm truly grateful for the interest you've shown in my work.

References

Andersson, M., Andolfsson, T., Brattström, T., Christiansson, P., Dahlqvist, P., Ericsson, U., Erlström, M., Hedin, P., Hjerne, C.-E., Holmström, M., Khalili, M., Lindgren, P., Lindström, S., Lund, B., Persson, L., Ringstad, K., Slagbrand, P., Sopher, D., Wickström, L., & Yotis, L. (2025, March). *Geologisk lagring av koldioxid, delrapport 2* (Rapportering av regeringsuppdrag No. Diarie-nr: 21-3126/2024). Sveriges geologiska undersökning. Uppsala. Retrieved May 20, 2025, from https://resource.sgu.se/dokument/publikation/rr/rr202502rapport/RR2502.pdf

Andersson, M., Dahlqvist, P., Ericsson, U., Erlström, M., Hedin, P., Lindgren, P., Persson, L., Slagbrand, P., Sopher, D., Wickström, L., von Zweigbergk, H., & Yotis, L. (2023, December). *Geologisk lagring av koldioxid, delrapport 1* (Rapportering av regeringsuppdrag No. Diarie-nr: 21-3102/2022). Sveriges geologiska undersökning. Uppsala. Retrieved May 20, 2025, from https://resource.sgu.se/dokument/publikation/rr/rr202304rapport/RR2304.pdf

Åström, E. K. L., Carroll, M. L., Ambrose, W. G., Sen, A., Silyakova, A., & Carroll, J. (2018). Methane cold seeps as biological oases in the high-Arctic deep sea. *Limnology and Oceanography*, *63*(S1). https://doi.org/10.1002/lno.10732

Benson, S. M., & Cole, D. R. (2008). CO_2 sequestration in deep sedimentary formations. *Elements*, *4*(5), 325–331. https://doi.org/10.2113/gselements.4.5.325

Chadwick, A., Arts, R., Bernstone, C., May, F., Thibeau, S., & Zweigel, P. (2008, March). *Best practice for the storage of CO_2 in saline aquifers - observations and guidelines from the SACS and CO2STORE projects* (Vol. 14). British Geological Survey. Retrieved May 20, 2025, from http://www.bgs.ac.uk/downloads

Colbo, K., Ross, T., Brown, C., & Weber, T. (2014). A review of oceanographic applications of water column data from multibeam echosounders. *Estuarine, Coastal and Shelf Science*, *145*, 41–56. https://doi.org/10.1016/j.ecss.2014.04.002

De Robertis, A., & Handegard, N. O. (2013). Fish avoidance of research vessels and the efficacy of noise-reduced vessels: A review. *ICES Journal of Marine Science*, *70*(1), 34–45. https://doi.org/10.1093/icesjms/fss155

Dixon, T., Garrett, J., & Kleverlaan, E. (2014). Update on the london protocol – developments on transboundary ccs and on geoengineering. *Energy Procedia*, *63*, 6623–6628. https://doi.org/10.1016/j.egypro.2014.11.698

Echoview. (2021). https://echoview.com/

Ekman, V. W. (1905). On the influence of the earth's rotation on ocean-currents. *Arkiv för matematik, astronomi och fysik, Bd. 2, no. 11.*

Fleury, M., Pironon, J., Le Nindre, Y., Bildstein, O., Berne, P., Lagneau, V., Broseta, D., Pichery, T., Fillacier, S., Lescanne, M., & Vidal, O. (2011). Evaluating sealing efficiency of caprocks for CO_2 storage: An overviewof the Geocarbone Integrity program and results. *Energy Procedia*, *4*, 5227–5234. https://doi.org/10.1016/j.egypro.2011.02.501

FMMidwater. (2022). https://qps.nl/fledermaus/

Göteborgs Universitet. (2024, November). Information om R/V Skagerak | Skagerak Facility [publisher: Göteborgs Universitet]. Retrieved May 28, 2025, from https://www.gu.se/skagerak/information-om-rv-skagerak

Haszeldine, R. S., Scott, V., Johnson, G., Mabon, L., Gilfillan, S., & Shackley, S. (2014, January). *Sleipner CO_2 securely stored deep beneath seabed, in spite of unexpected Hugin fracture discovery* (Working Paper). Scottish Carbon Capture and Storage (SCCS). https://doi.org/10.7488/WP-SCCS-2014-01

Havs- och vattenmyndigheten. (2023, June). Sill/Strömming [publisher: Havs- och vattenmyndigheten]. Retrieved May 20, 2025, from https://www.havochvatten.se/arter-och-livsmiljoer/arter-och-naturtyper/sill-stromming.html

Hicks, B., Ayna, C. O., Senyurek, V., Gupta, S., Skarke, A., & Gurbuz, A. C. (2023). Machine learning based automated detection of seafloor gas seeps, 1–6. https://doi.org/10.23919/OCEANS52994.2023.10337038

Higgs, B., Mountjoy, J. J., Crutchley, G. J., Townend, J., Ladroit, Y., Greinert, J., & McGovern, C. (2019). Seep-bubble characteristics and gas flow rates from a shallow-water, high-density seep field on the shelf-to-slope transition of the Hikurangi subduction margin. *Marine Geology*, *417*, 105985. https://doi.org/10.1016/j.margeo.2019.105985

Hughes Clarke, J. (2006). Applications of multibeam water column imaging for hydrographic survey. *Hydrographic Journal*, *120*, 3–15.

International Maritime Organization. (2012, November). *2012 specific guidelines for the assessment of carbon dioxide for disposal into sub-seabed geological formations* (Guideline No. LP.7. LC 34/15, Annex 8) (aka Revised CO2 Specific Guidelines or Revised CO2 Sequestration Guidelines). International Maritime Organization. Retrieved May 20, 2025, from https://www.imo.org/en/OurWork/Environment/Pages/CCS-Default.aspx

Ke, P., Ciais, P., Yao, Y., Sitch, S., Li, W., Xu, Y., Du, X., Gui, X., Bastos, A., Zaehle, S., Poulter, B., Colligan, T., Woude, A. M. v. d., Peters, W., Liu, Z., Jin, Z., Tian, X., Wang, Y., Liu, J., ... Chevallier, F. (2025, April). Low latency global carbon budget reveals a continuous decline of the land carbon sink during the 2023/24 El Nino event [arXiv:2504.09189]. https://doi.org/10.48550/arXiv.2504.09189

Lamarche, G., Le Gonidec, Y., Lucieer, V., Ladroit, Y., Weber, T., Gaillot, A., Heffron, E., Watson, S., & Pallentin, A. (2019). Gas bubble forensics team surveils the new zealand ocean. *Eos*, *100*. https://doi.org/10.1029/2019EO133649

Leifer, I., Luyendyk, B. P., Boles, J., & Clark, J. F. (2006). Natural marine seepage blowout: Contribution to atmospheric methane. *Global Biogeochemical Cycles*, *20*(3), 2005GB002668. https://doi.org/10.1029/2005GB002668

Maclennan, D. (2002). A consistent approach to definitions and symbols in fisheries acoustics. *ICES Journal of Marine Science*, *59*(2), 365–369. https://doi.org/10.1006/jmsc.2001.1158

Manjur, S. M., Senyurek, V., Kalski, R., Gupta, S., Skarke, A., & Gurbuz, A. C. (2025). Automated detection of seafloor gas seeps in multibeam echosounder data with an attention-guided convolutional neural network. *IEEE Journal of Selected Topics in Applied Earth Observations and Remote Sensing*, *18*, 5633–5645. https://doi.org/10.1109/JSTARS.2025.3535234

Mathys, M., Thießen, O., Theilen, F., & Schmidt, M. (2005). Seismic characterisation of gas-rich near surface sediments in the arkona basin, baltic sea. *Marine Geophysical Researches*, *26*(2-4), 207–224. https://doi.org/10.1007/s11001-005-3719-4

McGonigle, C., Grabowski, J. H., Brown, C. J., Weber, T. C., & Quinn, R. (2010). Detection of deep water benthic macroalgae using image-based classification techniques on multibeam backscatter at Cashes Ledge, Gulf of Maine, USA. *Estuarine, Coastal and Shelf Science*, *91*(1), 87–101. https://doi.org/10.1016/j.ecss.2010.10.016

Mitchell, G. A., Mayer, L. A., & Gharib, J. J. (2022). Bubble vent localization for marine hydrocarbon seep surveys. *Interpretation*, *10*(1), SB107–SB128. https://doi.org/10.1190/INT-2021-0084.1

Nau, A. W., Lucieer, V., Ladroit, Y., Kunnath, H., & Martin, T. (2025). A method for the simulation and removal of multibeam echosounder water column data artifacts. *IEEE Journal of Oceanic Engineering*, 1–15. https://doi.org/10.1109/JOE.2024.3525157

Nau, A. W., Lucieer, V., & Schimel, A. C. G. (2018). Modeling the along-track sidelobe interference artifact in multibeam sonar water-column data. *OCEANS 2018 MTS/IEEE Charleston*, 1–5. https://doi.org/10.1109/OCEANS.2018.8604866

Nau, A. W., Scoulding, B., Kloser, R. J., Ladroit, Y., & Lucieer, V. (2022). Extended detection of shallow water gas seeps from multibeam echosounder water column data. *Frontiers in Remote Sensing*, *3*, 839417. https://doi.org/10.3389/frsen.2022.839417

Okuyama, Y., Nakashima, Y., Sasaki, M., & Ueda, A. (2011). Do the sedimentary strata have power to neutralize leaking CO_2 ?: A natural analogue study on past CO_2 invasion and carbonate precipitation in the Cretaceous Izumi Group, SW Japan. *Energy Procedia*, *4*, 4953–4960. https://doi.org/10.1016/j.egypro.2011.02.465

Oldenburg, C. M., Bryant, S. L., & Nicot, J.-P. (2009). Certification framework based on effective trapping for geologic carbon sequestration. *International Journal of Greenhouse Gas Control*, *3*(4), 444–457. https://doi.org/10.1016/j.ijggc.2009.02.009

Ousterhout, J. (1998). Scripting: Higher level programming for the 21st Century. *Computer*, *31*(3), 23–30. https://doi.org/10.1109/2.660187

Porskamp, P., Schimel, A. C. G., Young, M., Rattray, A., Ladroit, Y., & Ierodiaconou, D. (2022). Integrating multibeam echosounder water-column data into benthic habitat mapping. *Limnology and Oceanography*, *67*(8), 1701–1713. https://doi.org/10.1002/lno.12160

QGIS Development Team. (2024). QGIS Geographic Information System. https://www.qgis.org

Rovere, M., Mercorella, A., Frapiccini, E., Funari, V., Spagnoli, F., Pellegrini, C., Bonetti, A. S., Veneruso, T., Tassetti, A. N., Dell'Orso, M., Mastroianni, M., Giuliani, G., De Marco, R., Fabi, G., Ciccone, F., & Antoncecchi, I. (2020). Geochemical and geophysical monitoring of hydrocarbon seepage in the adriatic sea. *Sensors*, *20*(5), 1504. https://doi.org/10.3390/s20051504

Ruppel, C., Skarke, A., Miller, N., Kidiwela, M., Kluesner, J., & Baldwin, W. (2024). Methane seeps on the U.S. Atlantic margin: An updated inventory and interpretative framework. *Marine Geology*, *471*, 107287. https://doi.org/10.1016/j.margeo.2024.107287

Rutqvist, J. (2012). The geomechanics of CO_2 storage in deep sedimentary formations. *Geotechnical and Geological Engineering*, *30*(3), 525–551. https://doi.org/10.1007/s10706-011-9491-0

Ryan, T. E., Downie, R. A., Kloser, R. J., & Keith, G. (2015). Reducing bias due to noise and attenuation in open-ocean echo integration data. *ICES Journal of Marine Science*, *72*(8), 2482–2493. https://doi.org/10.1093/icesjms/fsv121

Schimel, A. C. G., Beaudoin, J., Parnum, I. M., Le Bas, T., Schmidt, V., Keith, G., & Ierodiaconou, D. (2018). Multibeam sonar backscatter data processing. *Marine Geophysical Research*, *39*(1-2), 121–137. https://doi.org/10.1007/s11001-018-9341-z

Schimel, A. C. G., Brown, C. J., & Ierodiaconou, D. (2020). Automated filtering of multibeam water-column data to detect relative abundance of giant kelp(Macrocystis pyrifera). *Remote Sensing*, *12*(9), 1371. https://doi.org/10.3390/rs12091371

Schimel, A. C. G., Ladroit, Y., & Watson, S. (2024a). Espresso: An open-source software tool for visualizing and analysing multibeam water-column data. https://doi.org/10.5194/egusphere-egu24-11043

Schimel, A. C. G., Ladroit, Y., & Watson, S. (2024b, October). Espresso: Open source software for the visualization of multibeam water column data [publisher: Hydro International]. Retrieved May 22, 2025, from https://www.hydro-international.com/content/article/espresso-open-source-software-for-the-visualization-of-multibeam-water-column-data

Schneider Von Deimling, J., Brockhoff, J., & Greinert, J. (2007). Flare imaging with multibeam systems: Data processing for bubble detection at seeps. *Geochemistry, Geophysics, Geosystems*, *8*(6), 2007GC001577. https://doi.org/10.1029/2007GC001577

Schneider Von Deimling, J., & Papenberg, C. (2012). Technical Note: Detection of gas bubble leakage via correlation of water column multibeam images. *Ocean Science*, *8*(2), 175–181. https://doi.org/10.5194/os-8-175-2012

Skarke, A., Ruppel, C., Kodis, M., Brothers, D., & Lobecker, E. (2014). Widespread methane leakage from the sea floor on the northern US Atlantic margin. *Nature Geoscience*, *7*(9), 657–661. https://doi.org/10.1038/ngeo2232

SMHI. (2023, January). Strömmar - Stena Skåne Ferrybox [publisher: SMHI]. Retrieved May 20, 2025, from https://www.smhi.se/data/hav-och-havsmiljo/strommar

Spain, E., Lamarche, G., Lucieer, V., Watson, S. J., Ladroit, Y., Heffron, E., Pallentin, A., & Whittaker, J. M. (2022). Acoustic predictors of active fluid expulsion from a hydrothermal vent field, offshore taupō volcanic zone, new zealand. *Frontiers in Earth Science*, *9*, 785396. https://doi.org/10.3389/feart.2021.785396

Suess, E. (2018). Marine cold seeps: Background and recent advances. In H. Wilkes (Ed.), *Hydrocarbons, Oils and Lipids: Diversity, Origin, Chemistry and Fate* (pp. 1–21). Springer International Publishing. https://doi.org/10.1007/978-3-319-54529-5_27-1

Sveriges Geologiska Undersökning. (2025, January). Facts about Ocean Surveyor [publisher: Sveriges Geologiska Undersökning]. Retrieved May 29, 2025, from https://www.sgu.se/en/products/sgus-research-vessels/facts-about-ocean-surveyor/

Turco, F., Ladroit, Y., Watson, S. J., Seabrook, S., Law, C. S., Crutchley, G. J., Mountjoy, J., Pecher, I. A., Hillman, J. I. T., Woelz, S., & Gorman, A. R. (2022). Estimates of methane release from gas seeps at the southern hikurangi margin, new zealand. *Frontiers in Earth Science*, *10*, 834047. https://doi.org/10.3389/feart.2022.834047

Urban, P., Köser, K., & Greinert, J. (2017). Processing of multibeam water column image data for automated bubble/seep detection and repeated mapping. *Limnology and Oceanography: Methods*, *15*(1), 1–21. https://doi.org/10.1002/lom3.10138

Urban, P., Veloso-Alarcón, M. E., & Greinert, J. (2023). Echo grid integration: A novel method for preprocessing multibeam water column data to quantify underwater gas bubble emissions. *Limnology and Oceanography: Methods*, *21*(7), 377–400. https://doi.org/10.1002/lom3.10552

Vielstädte, L., Linke, P., Schmidt, M., Sommer, S., Haeckel, M., Braack, M., & Wallmann, K. (2019). Footprint and detectability of a well leaking CO_2 in the Central North Sea: Implications from a field experiment and numerical modelling. *International Journal of Greenhouse Gas Control*, *84*, 190–203. https://doi.org/10.1016/j.ijggc.2019.03.012

Von Deimling, J. S., Greinert, J., Chapman, N. R., Rabbel, W., & Linke, P. (2010). Acoustic imaging of natural gas seepage in the North Sea: Sensing bubbles controlled by variable currents. *Limnology and Oceanography: Methods*, *8*(5), 155–171. https://doi.org/10.4319/lom.2010.8.155

Weber, T. C. (2021). A cfar detection approach for identifying gas bubble seeps with multibeam echo sounders. *IEEE Journal of Oceanic Engineering*, *46*(4), 1346–1355. https://doi.org/10.1109/JOE.2021.3056910

Weber, T. C., Mayer, L., Jerram, K., Beaudoin, J., Rzhanov, Y., & Lovalvo, D. (2014). Acoustic estimates of methane gas flux from the seabed in a 6000 km^2 region in the Northern Gulf of Mexico. *Geochemistry, Geophysics, Geosystems*, *15*(5), 1911–1925. https://doi.org/10.1002/2014GC005271

Zhang, Q., & Tutolo, B. M. (2022). Evaluation of the potential of glauconite in the Western Canadian Sedimentary Basin for large-scale carbon dioxide mineralization. *International Journal of Greenhouse Gas Control*, *117*, 103663. https://doi.org/10.1016/j.ijggc.2022.103663

Zhang, W., Zhou, T., Li, J., & Xu, C. (2022). An efficient method for detection and quantitation of underwater gas leakage based on a 300-

khz multibeam sonar. *Remote Sensing*, *14*(17), 4301. https://doi.org/10.3390/rs14174301

Zhao, J., Mai, D., Zhang, H., & Wang, S. (2020). Automatic detection and segmentation on gas plumes from multibeam water column images. *Remote Sensing*, *12*(18), 3085. https://doi.org/10.3390/rs12183085

Zhao, J., Meng, J., Zhang, H., & Wang, S. (2017). Comprehensive detection of gas plumes from multibeam water column images with minimisation of noise interferences. *Sensors*, *17*(12), 2755. https://doi.org/10.3390/s17122755

Appendices

Appendix A

This appendix contains a closer look at all anomalies deemed "seep-like targets" in Section 6.2. For every seep, the following will be provided:

- Echo integrated grid.
- One or two pings in fan view.
- Marked stacked view.
- Link to GitHub folder containing additional pings in fan view, numbered in reverse chronological order, and GIF animations (both normal and in reverse).

Area 1

As possible seep C only lasted for one ping (and is most likely digital noise), it will be omitted from this section.

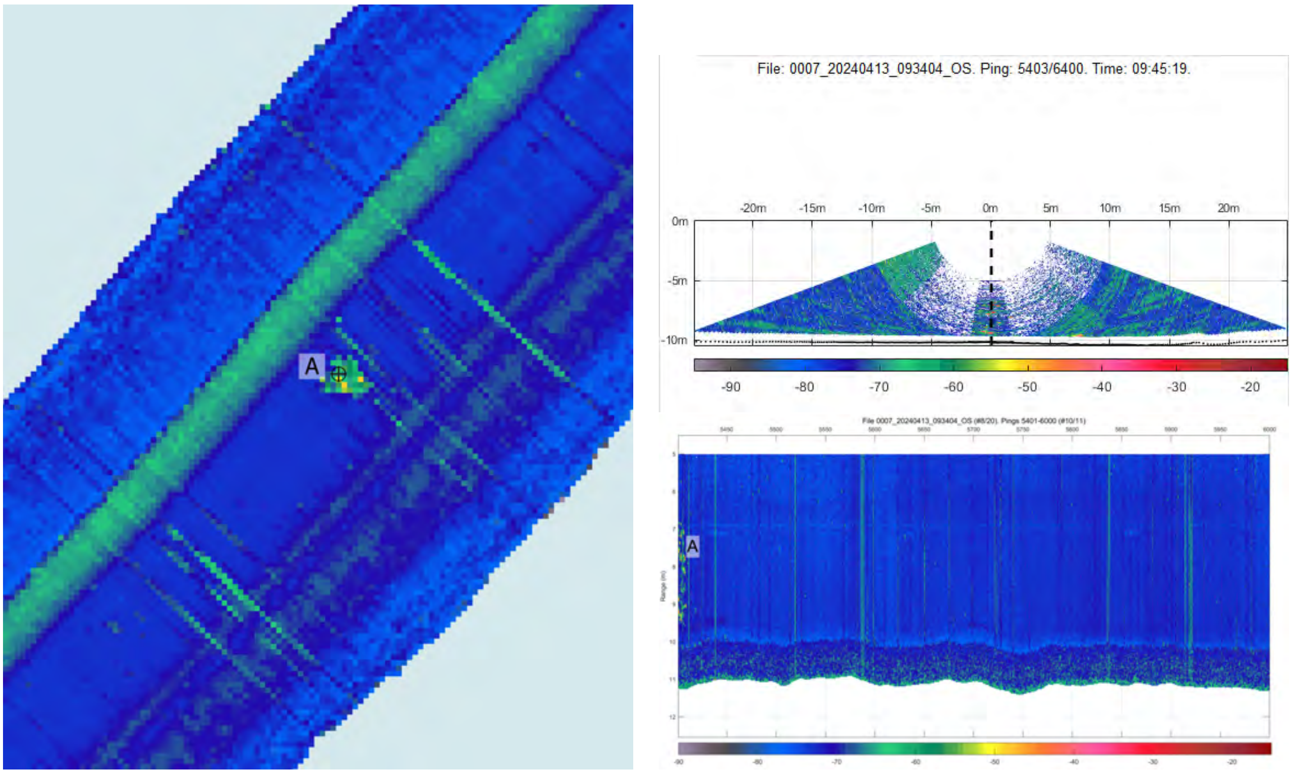

Fig. 36: Possible seep A in Area 1. Link to folder: Area 1 - A

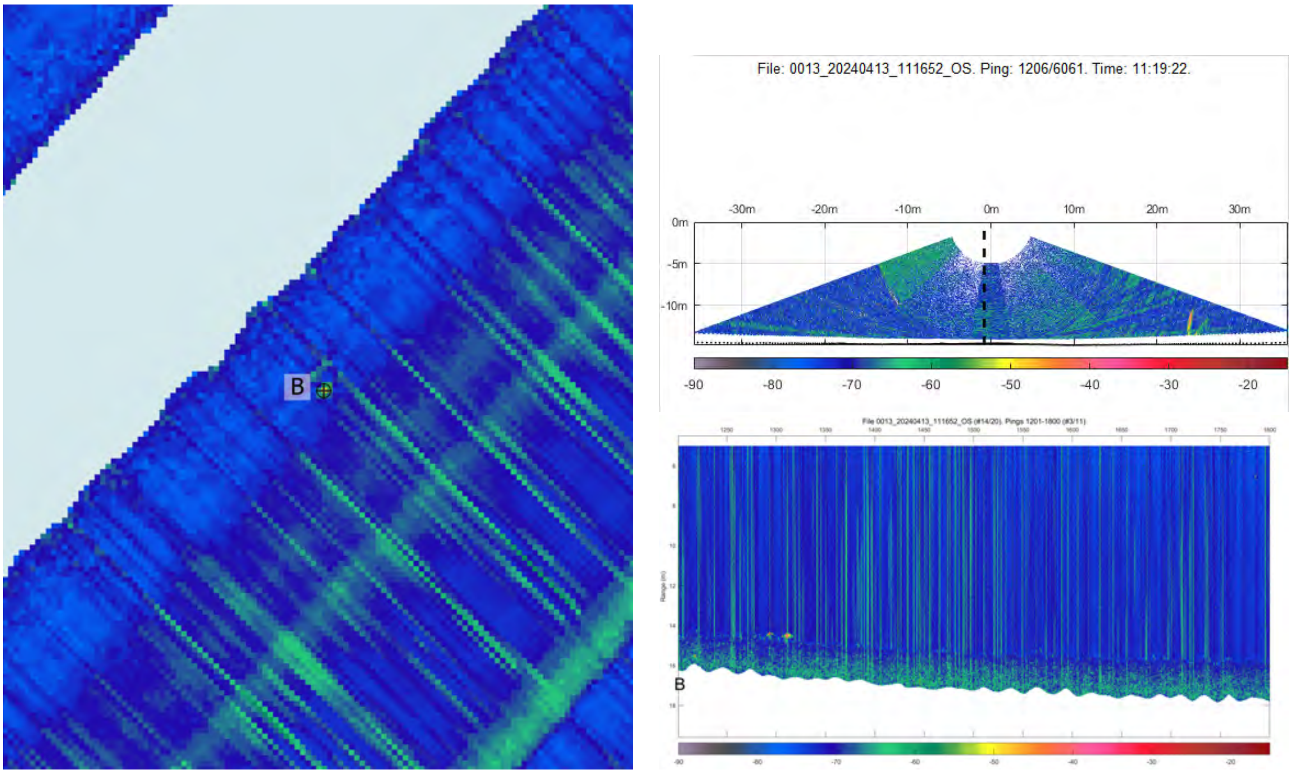

Fig. 37: Possible seep B in Area 1. Link to folder: Area 1 - B

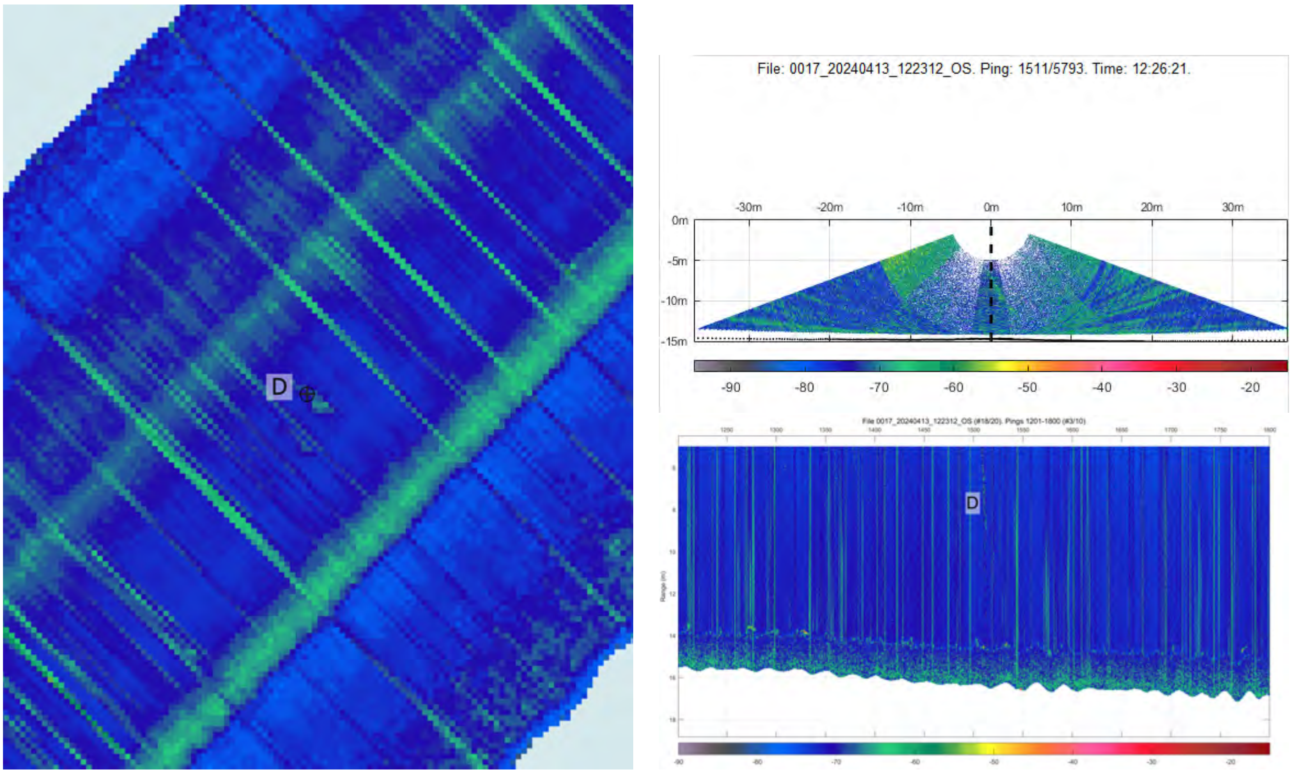

Fig. 38: Possible seep D in Area 1. Link to folder: Area 1 - D

Area 2

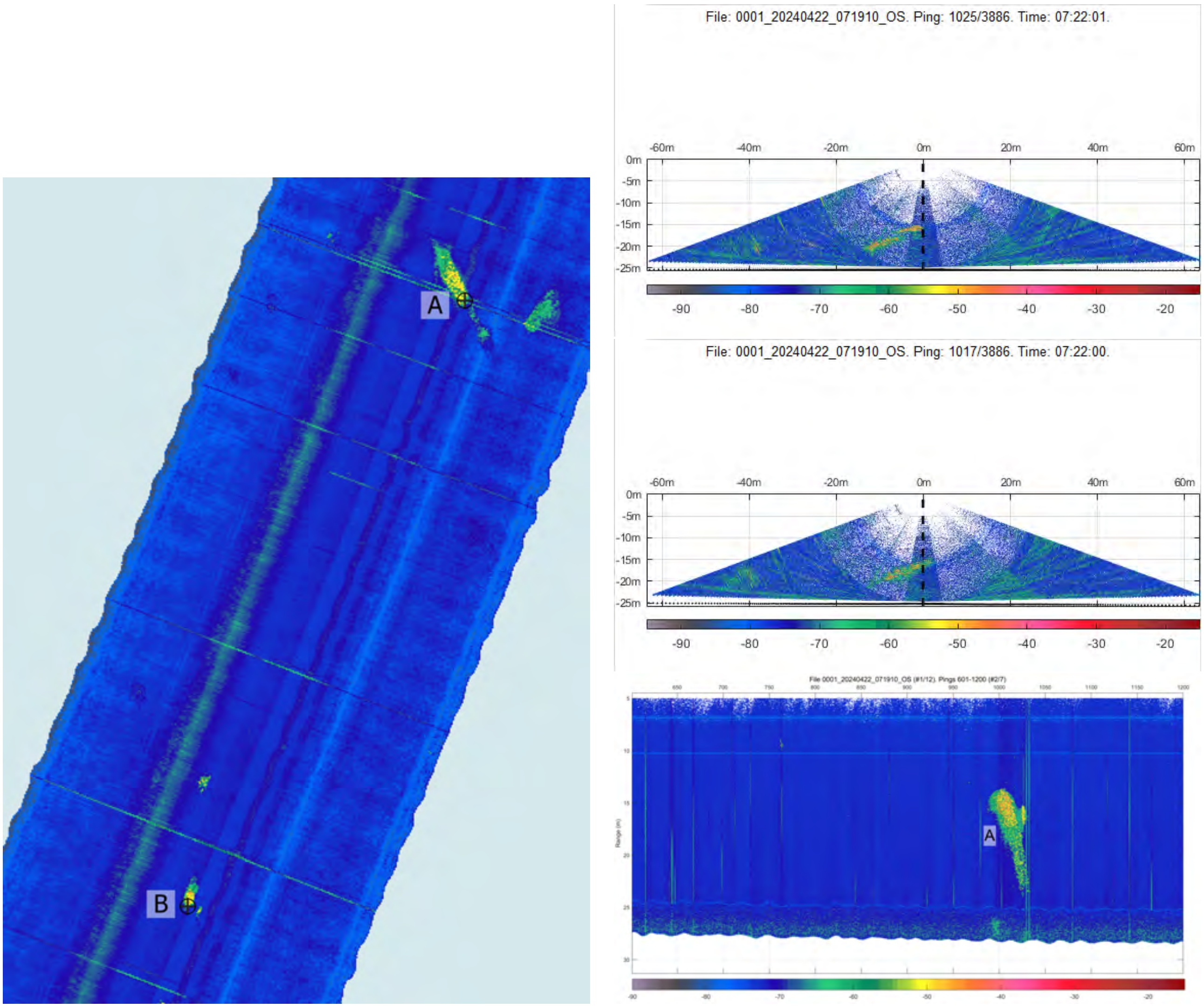

Fig. 39: Possible seep A in Area 2. Link to folder: Area 2 - A

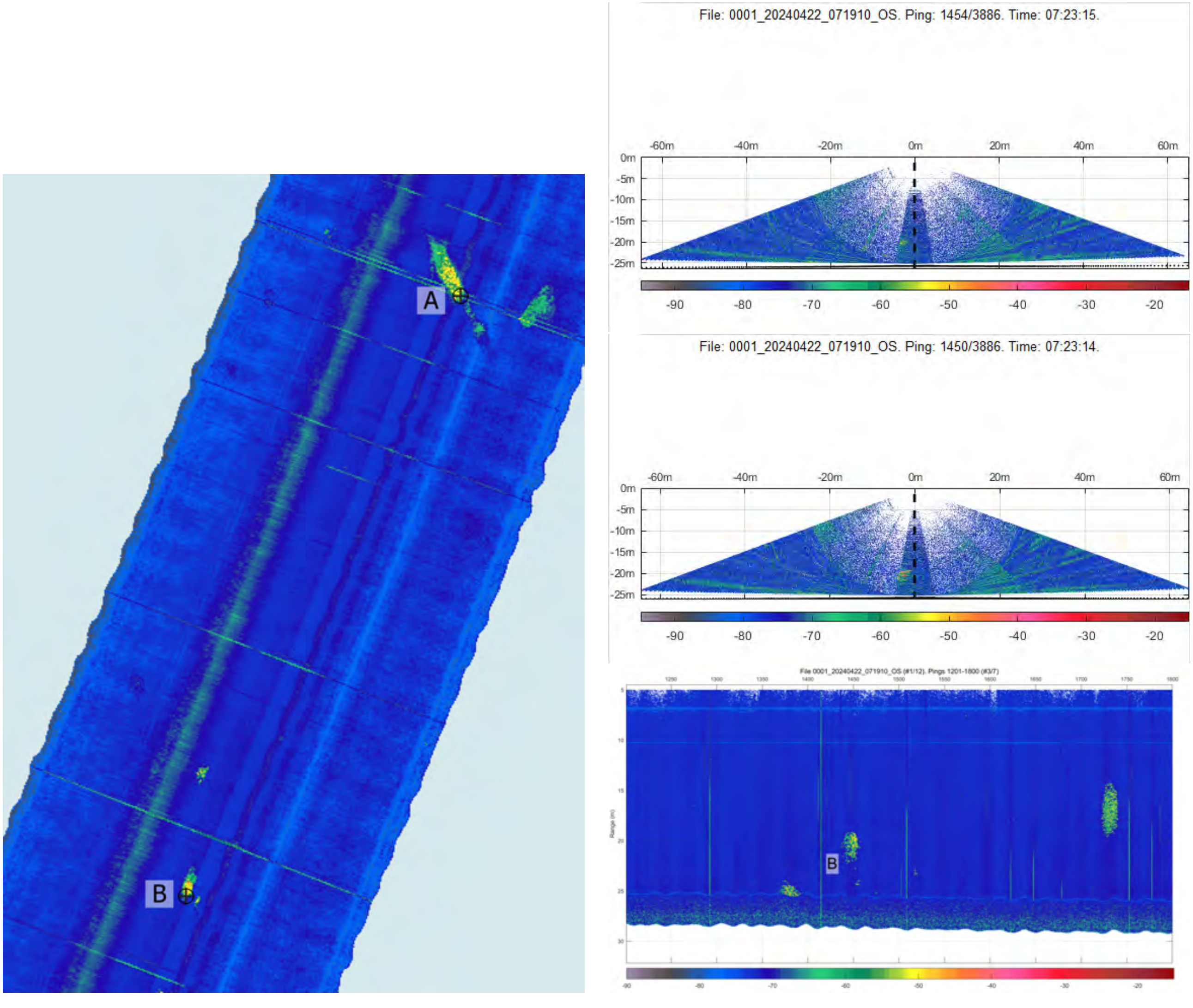

Fig. 40: Possible seep B in Area 2. Link to folder: Area 2 - B

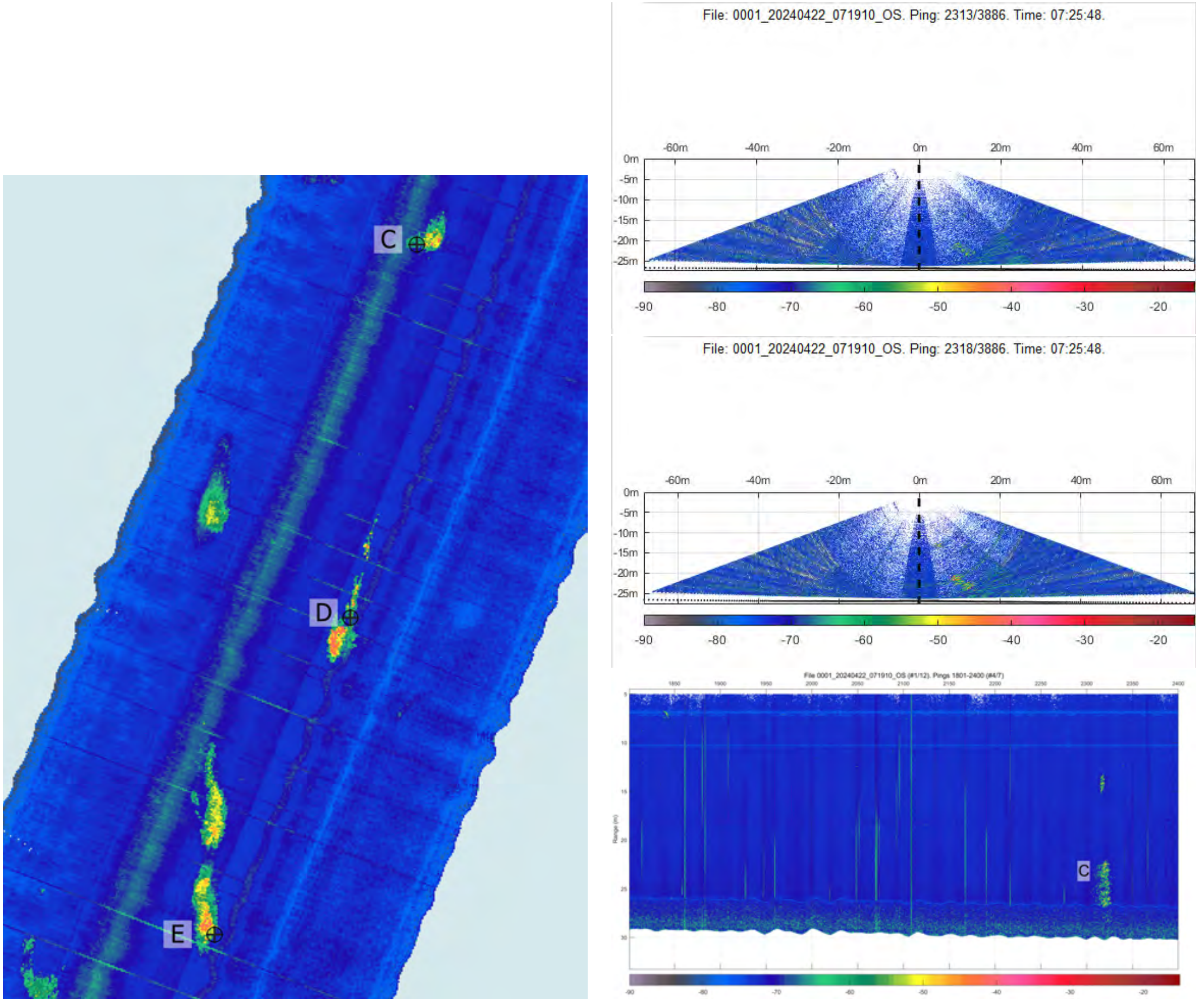

Fig. 41: Possible seep C in Area 2. Link to folder: Area 2 - C

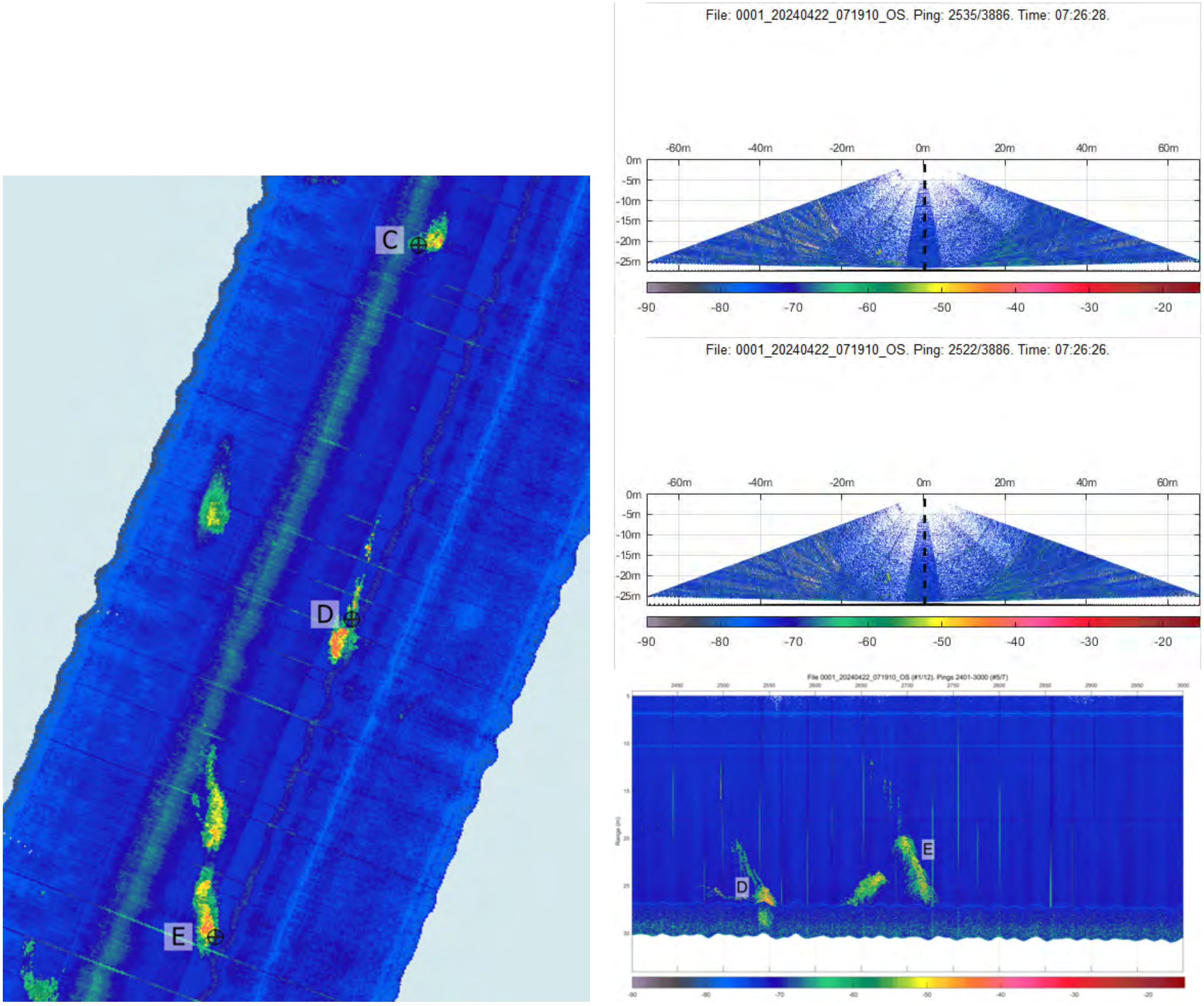

Fig. 42: Possible seep D in Area 2. Link to folder: Area 2 - D

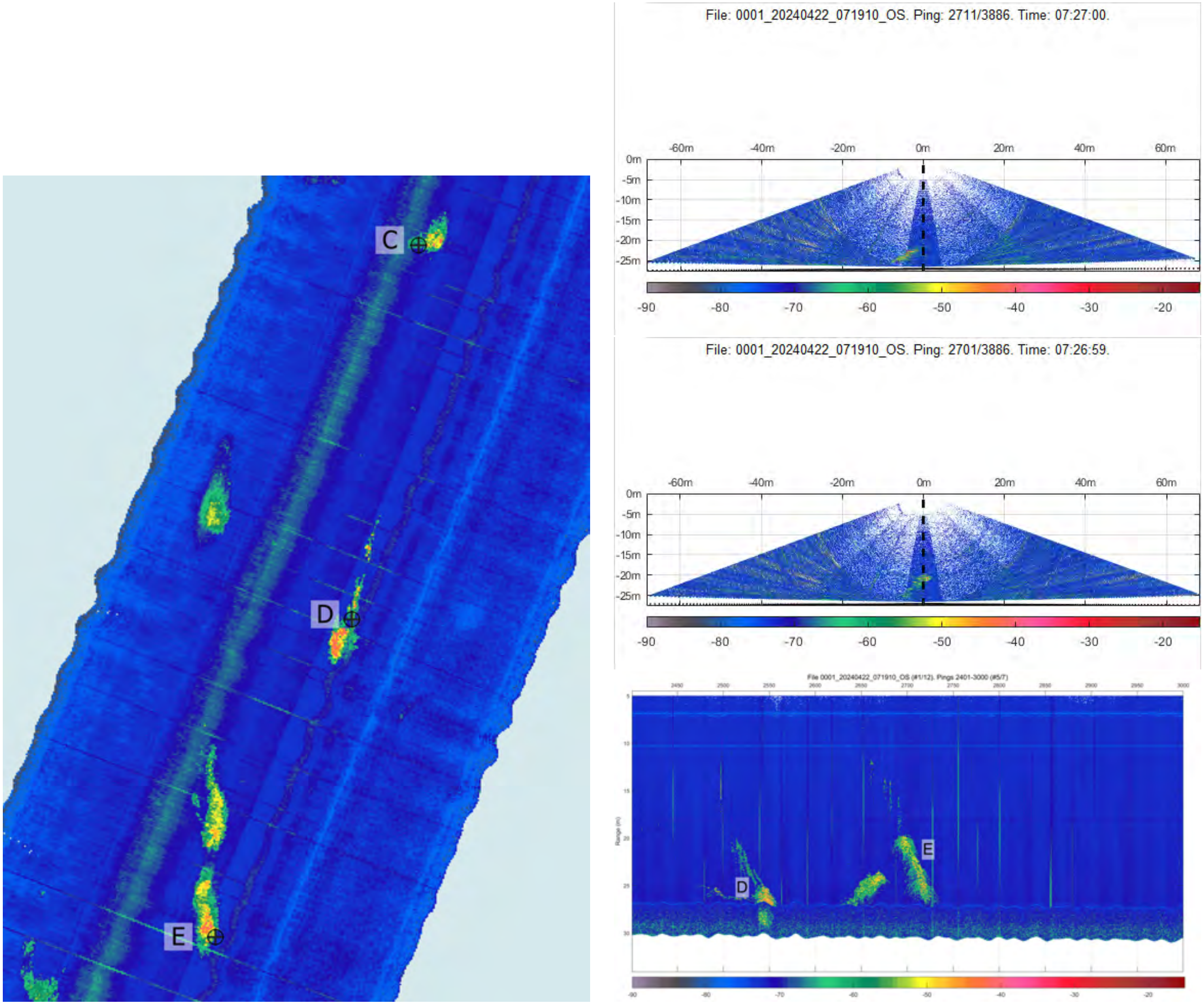

Fig. 43: Possible seep E in Area 2. Link to folder: Area 2 - E

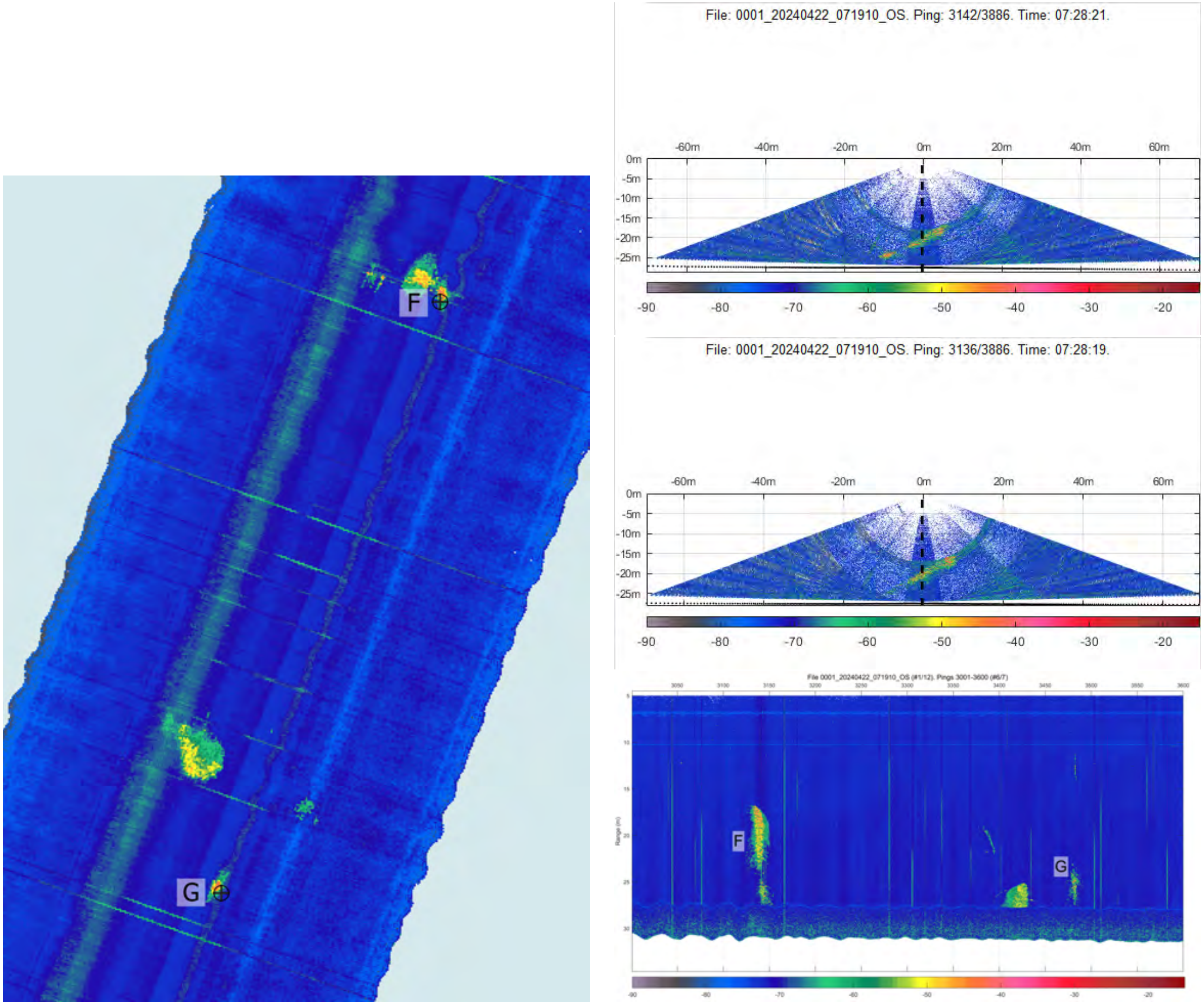

Fig. 44: Possible seep F in Area 2. Link to folder: Area 2 - F

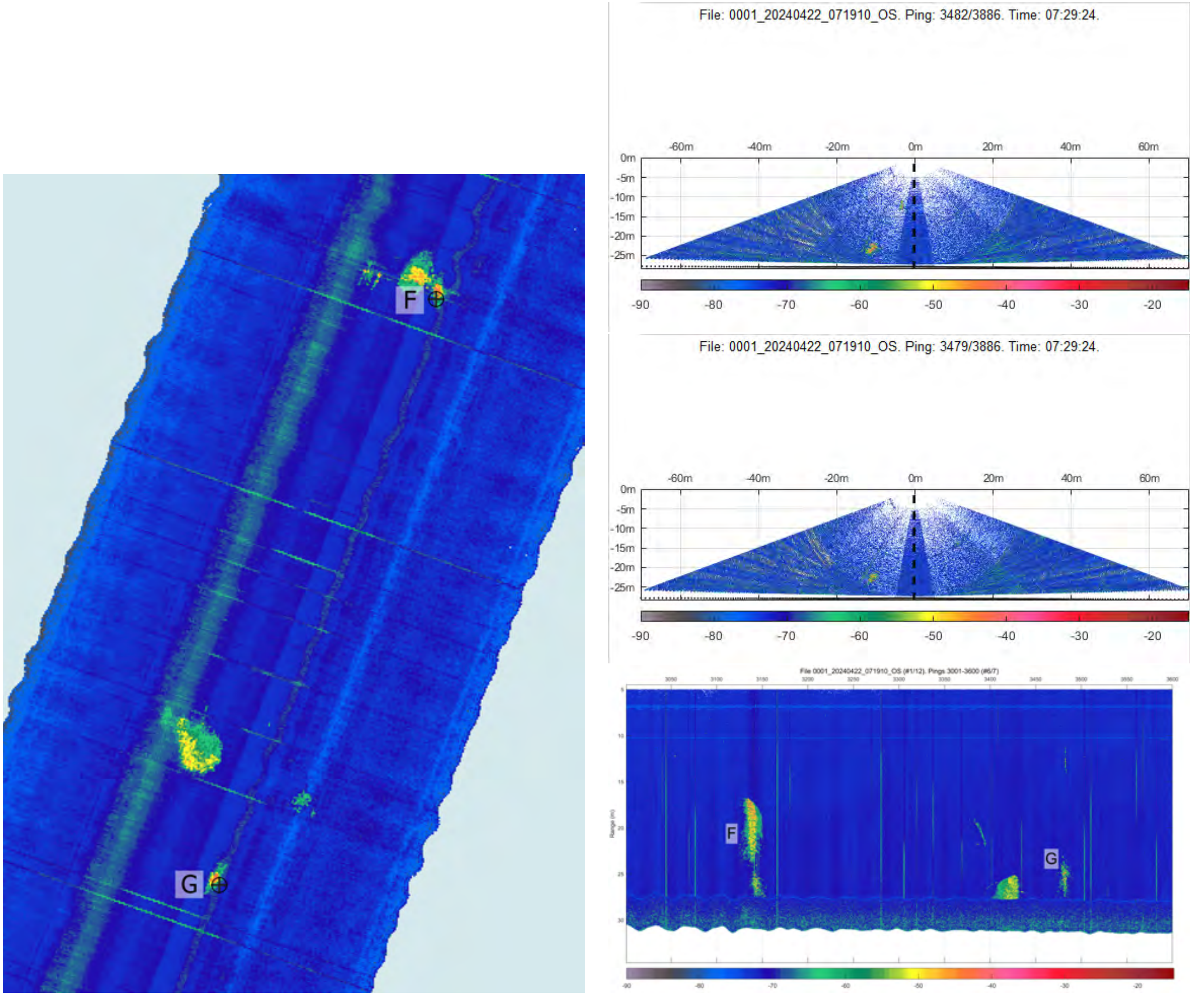

Fig. 45: Possible seep G in Area 2. Link to folder: Area 2 - G

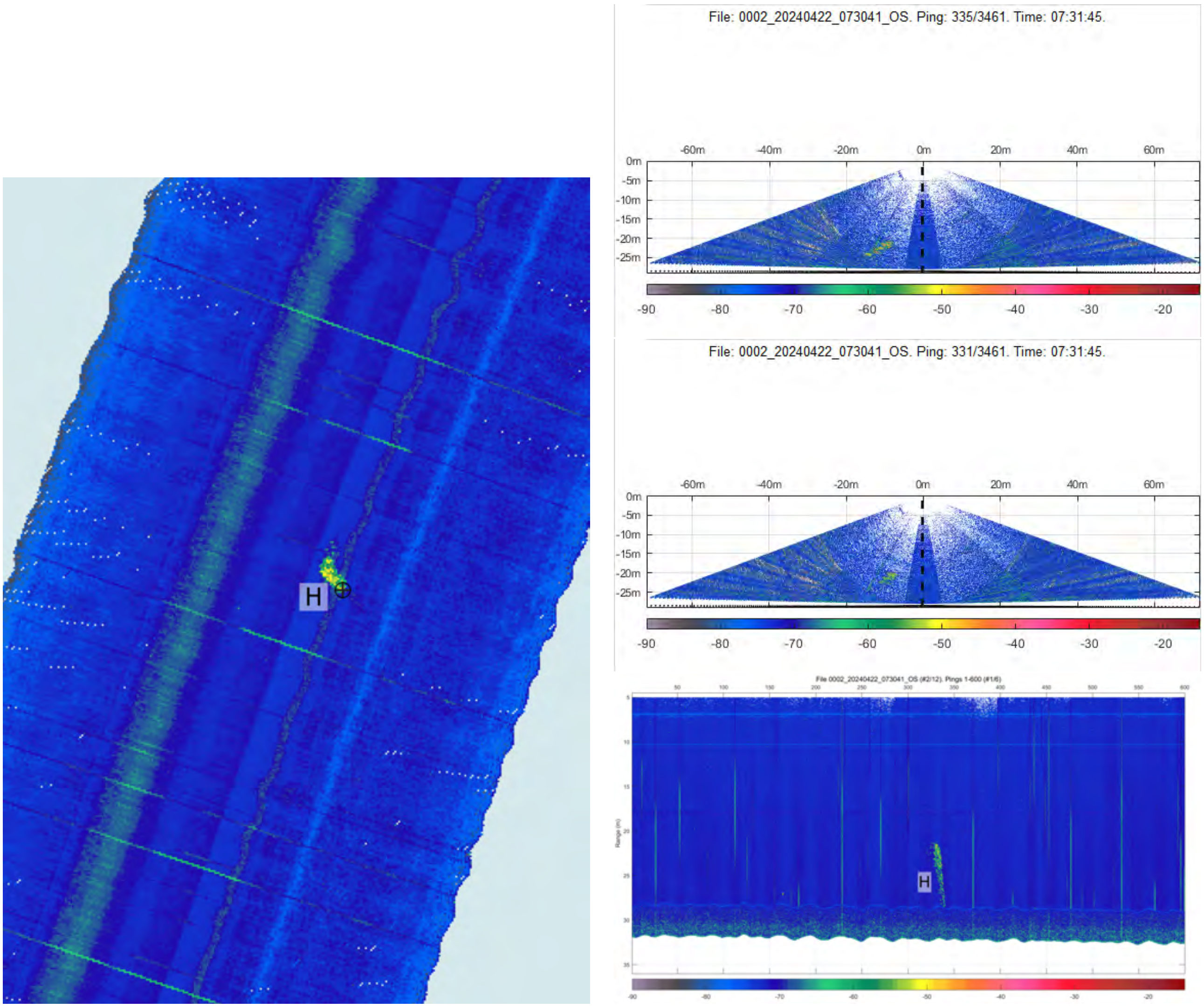

Fig. 46: Possible seep H in Area 2. Link to folder: Area 2 - H

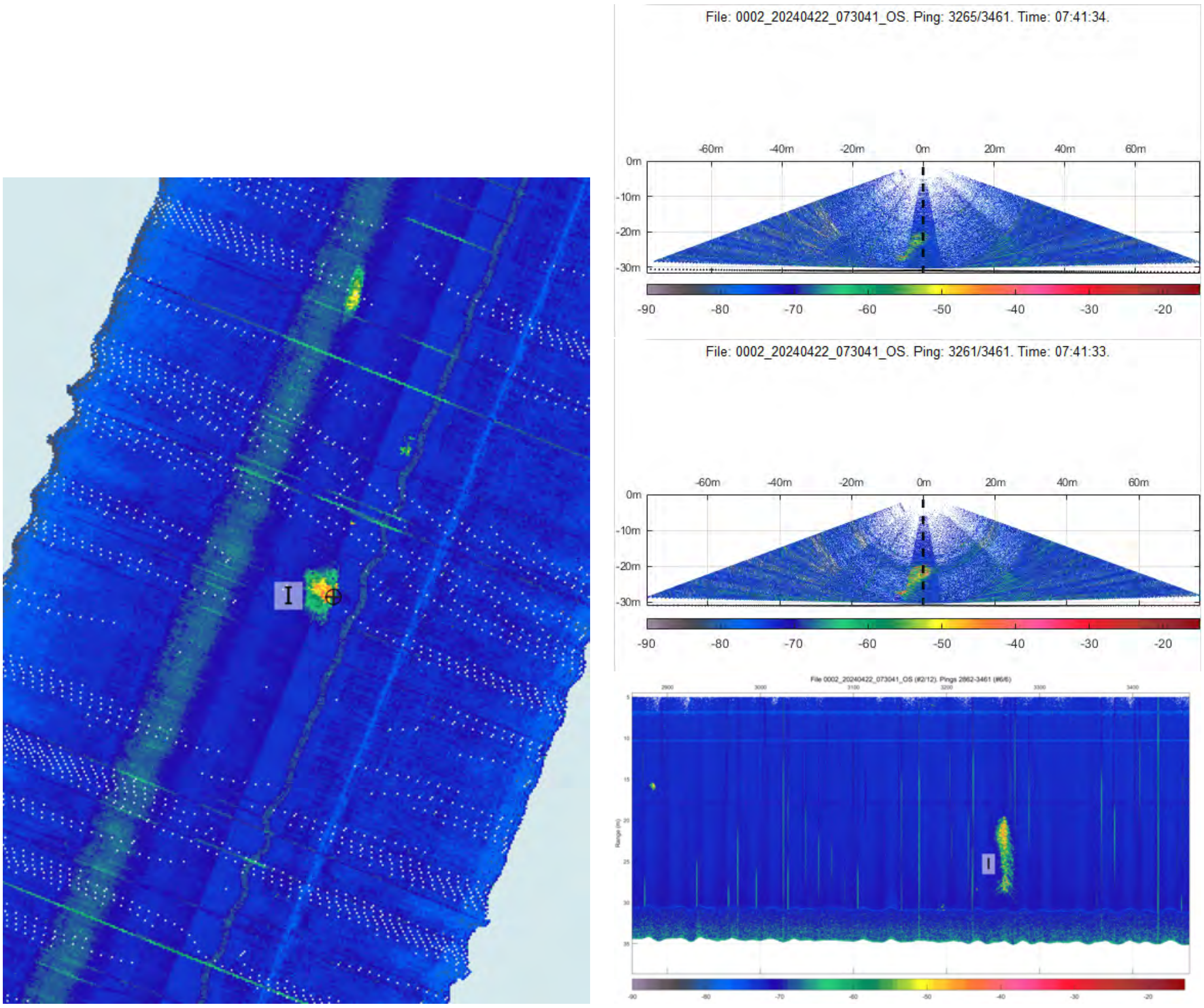

Fig. 47: Possible seep I in Area 2. Link to folder: Area 2 - I

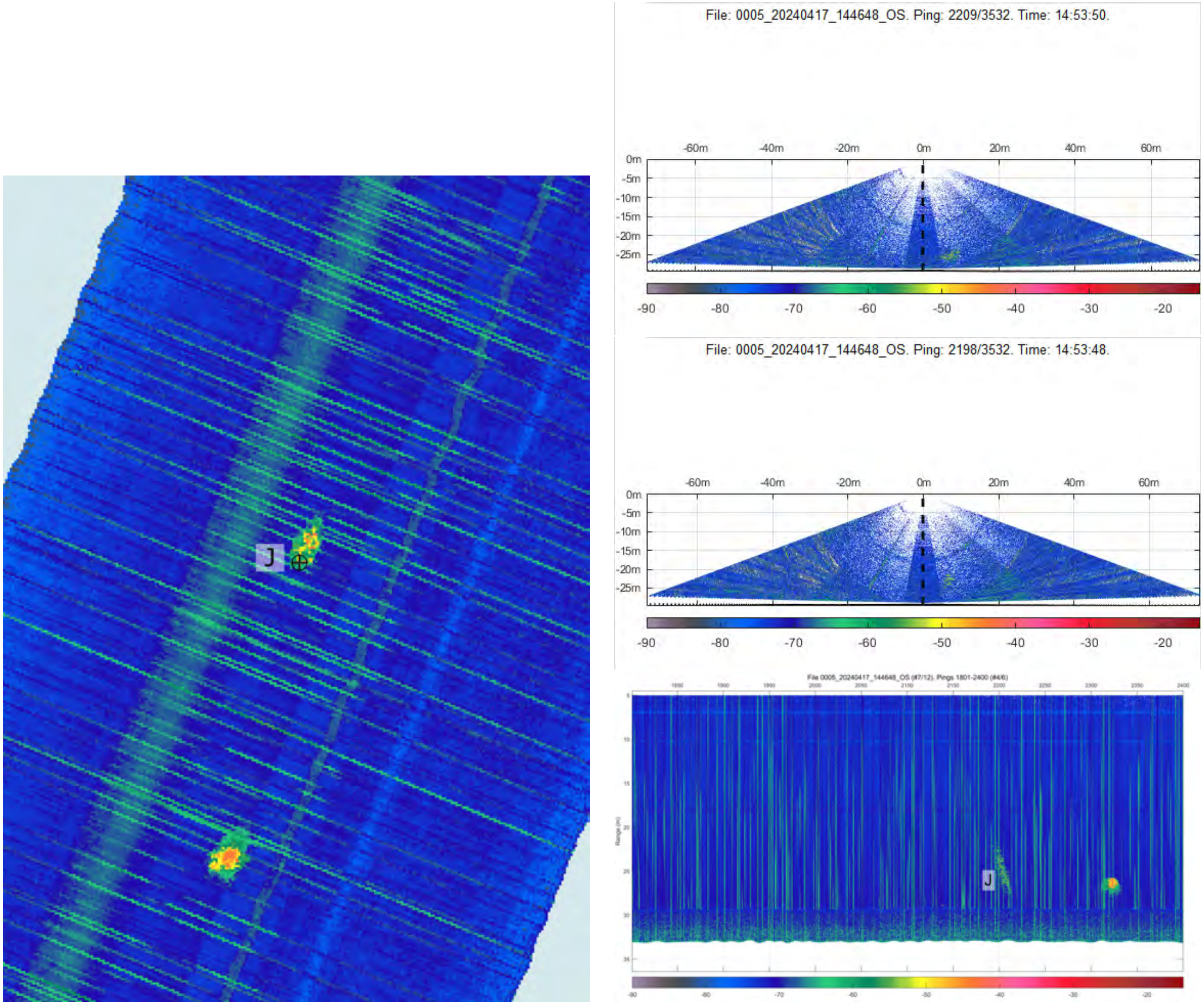

Fig. 48: Possible seep J in Area 2. Link to folder: Area 2 - J

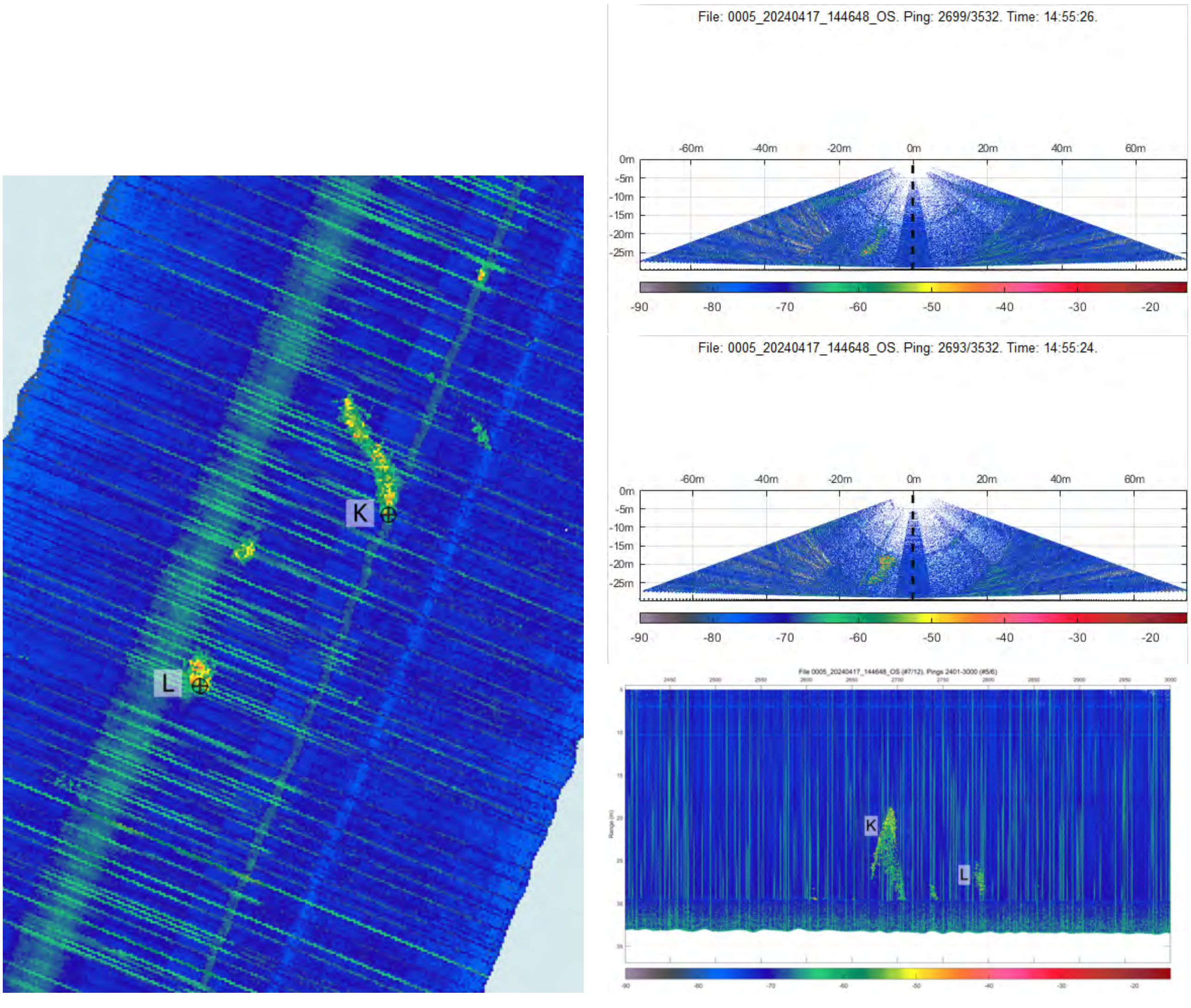

Fig. 49: Possible seep K in Area 2. Link to folder: Area 2 - K

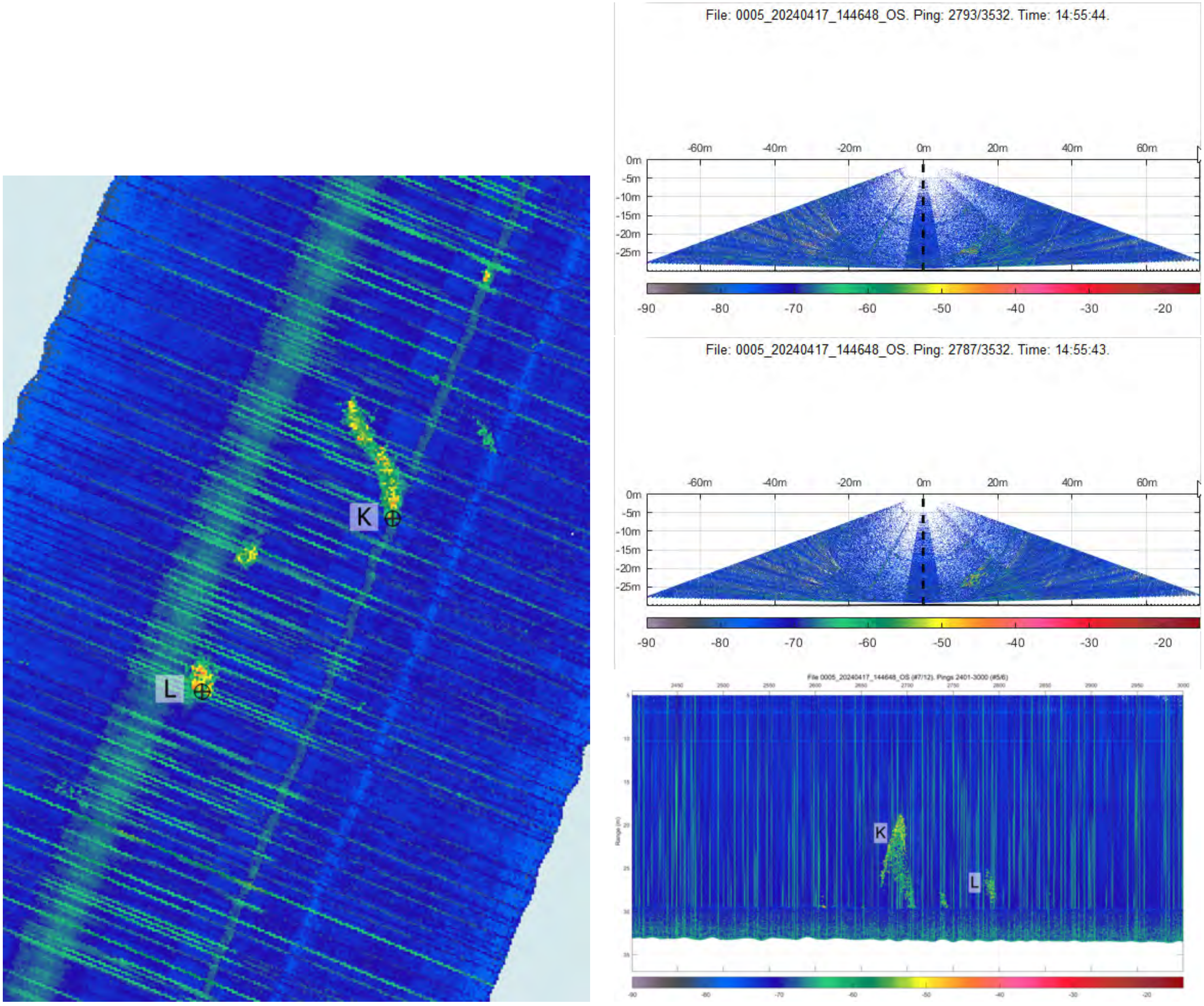

Fig. 50: Possible seep L in Area 2. Link to folder: Area 2 - L

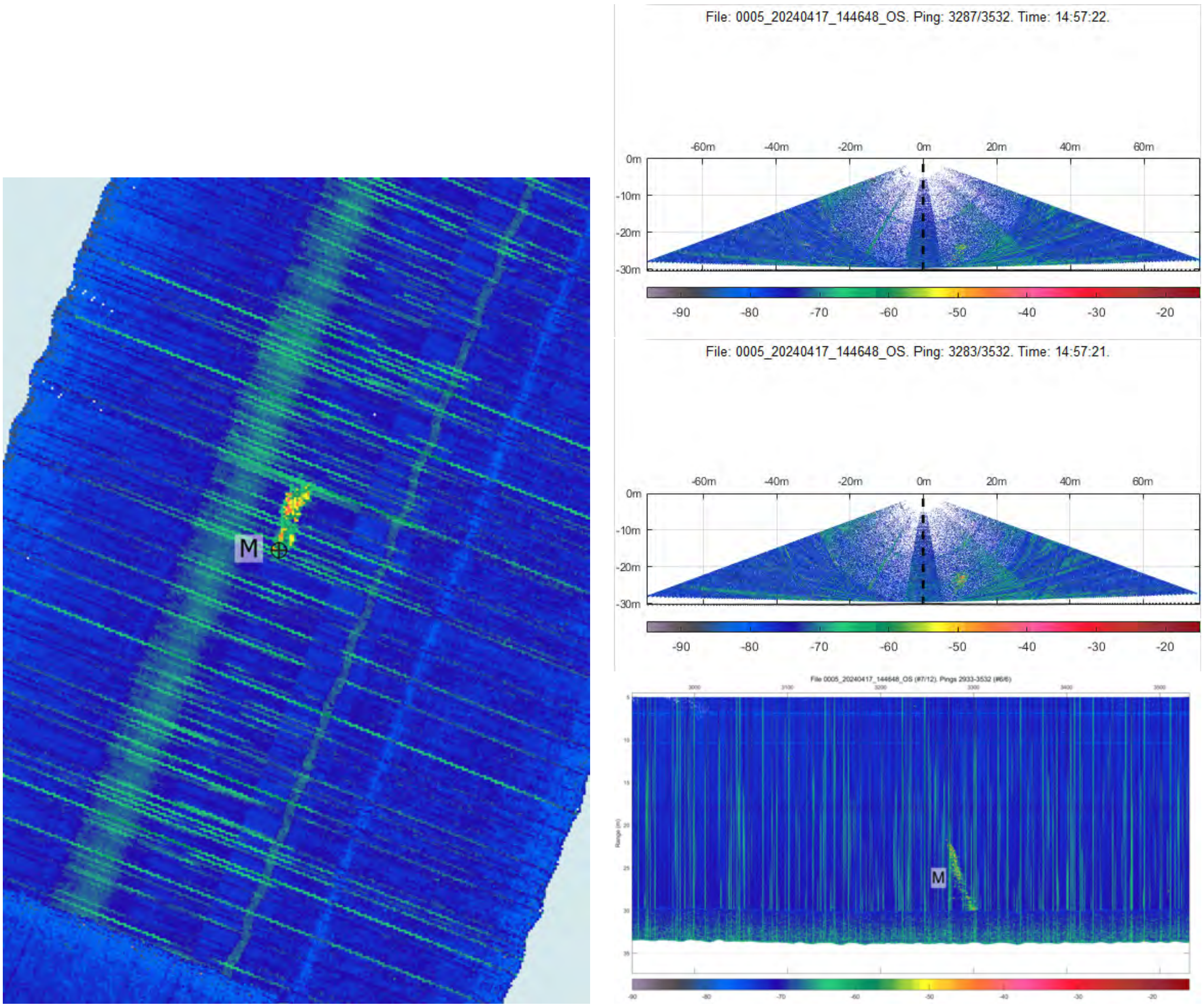

Fig. 51: Possible seep M in Area 2. Link to folder: Area 2 - M

Appendix B

This appendix contains all batch exported stacked view screenshots, grouped in sections; Byfjorden, Area 1, Area 2 and Area 3.

Byfjorden

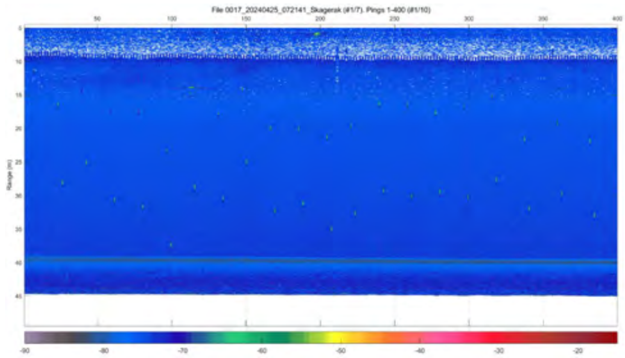

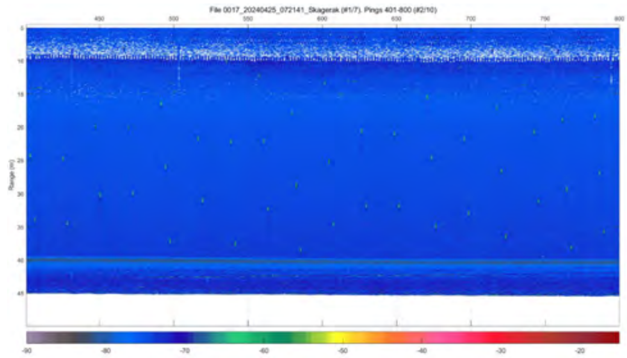

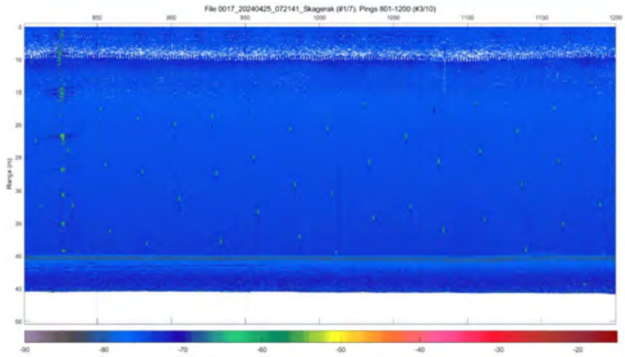

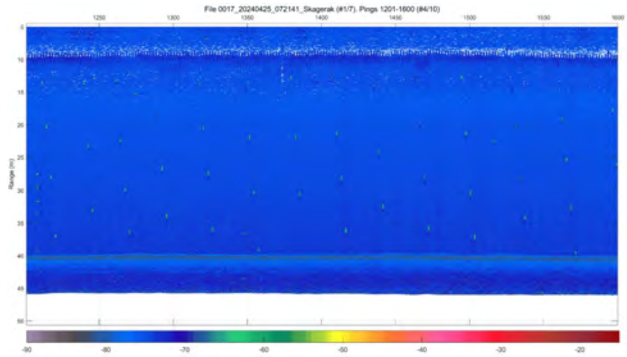

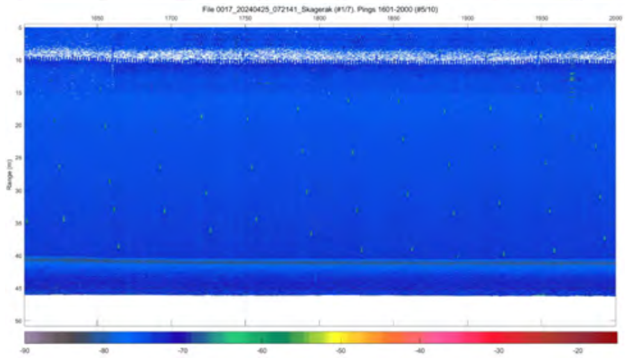

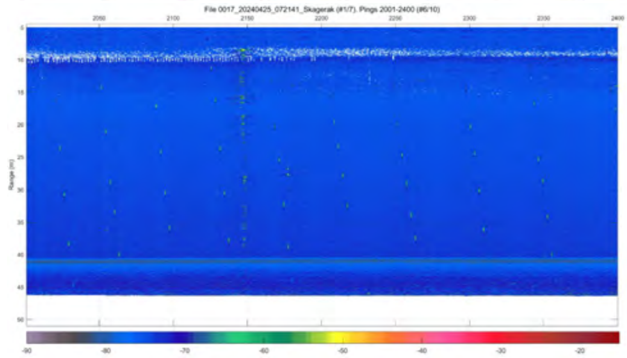

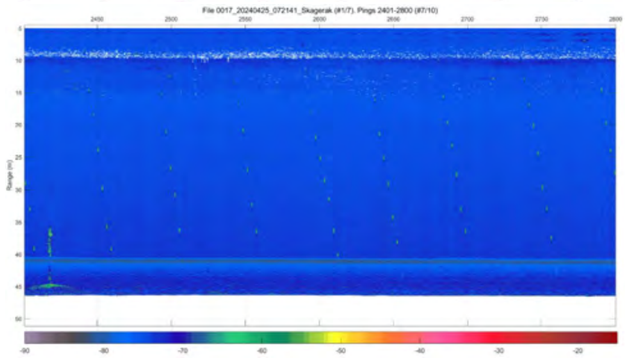

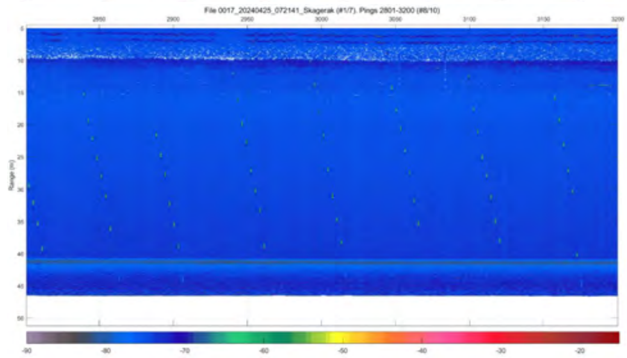

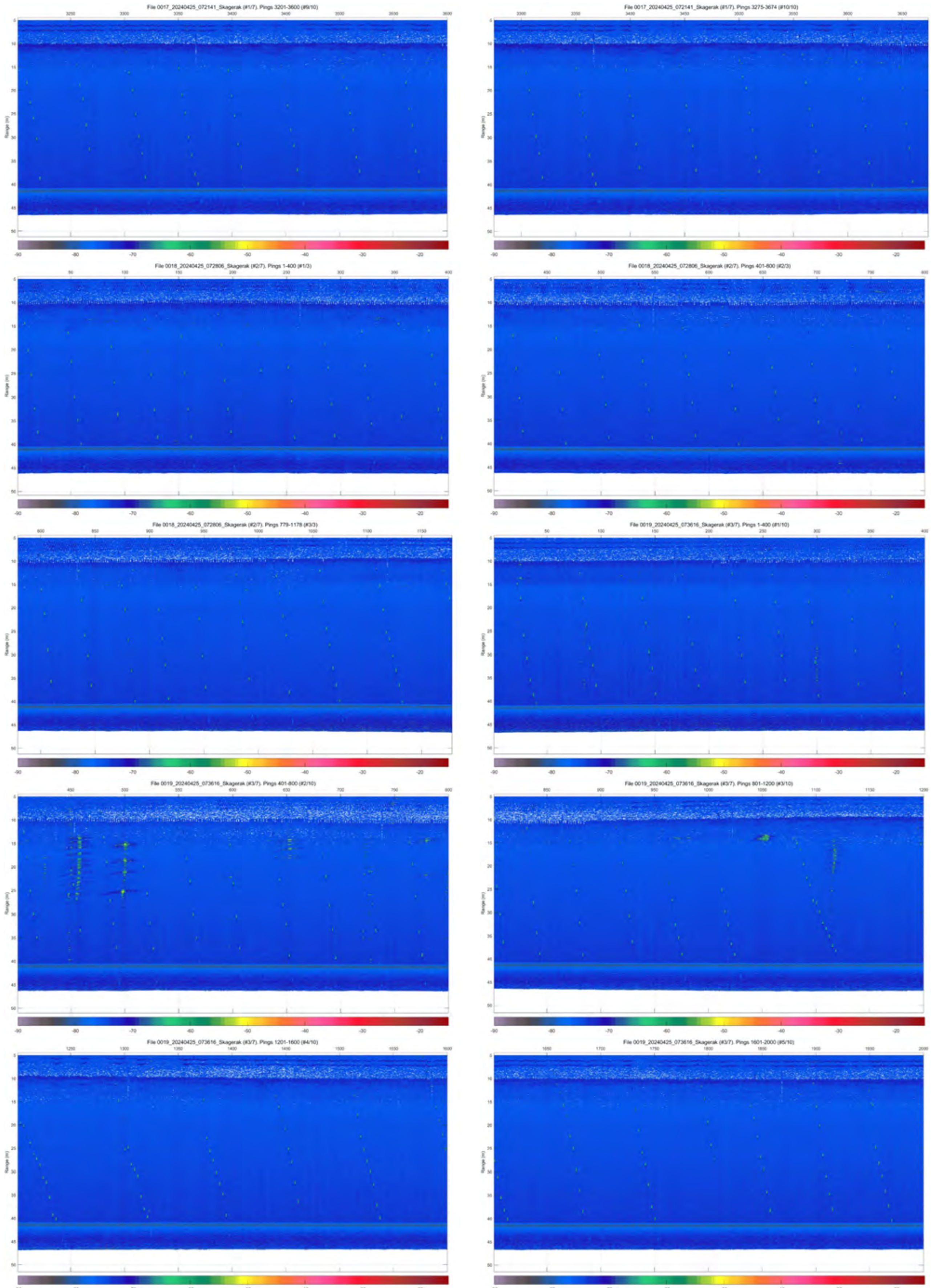
File 0017_20240425_072141_Skagerak (#1/7). Pings 3201-3600 (#9/10)
File 0017_20240425_072141_Skagerak (#1/7). Pings 3275-3674 (#10/10)
File 0018_20240425_072806_Skagerak (#2/7). Pings 1-400 (#1/3)
File 0018_20240425_072806_Skagerak (#2/7). Pings 401-800 (#2/3)
File 0018_20240425_072806_Skagerak (#2/7). Pings 779-1178 (#3/3)
File 0019_20240425_073616_Skagerak (#3/7). Pings 1-400 (#1/10)
File 0019_20240425_073616_Skagerak (#3/7). Pings 401-800 (#2/10)
File 0019_20240425_073616_Skagerak (#3/7). Pings 801-1200 (#3/10)
File 0019_20240425_073616_Skagerak (#3/7). Pings 1201-1600 (#4/10)
File 0019_20240425_073616_Skagerak (#3/7). Pings 1601-2000 (#5/10)
Range (m)

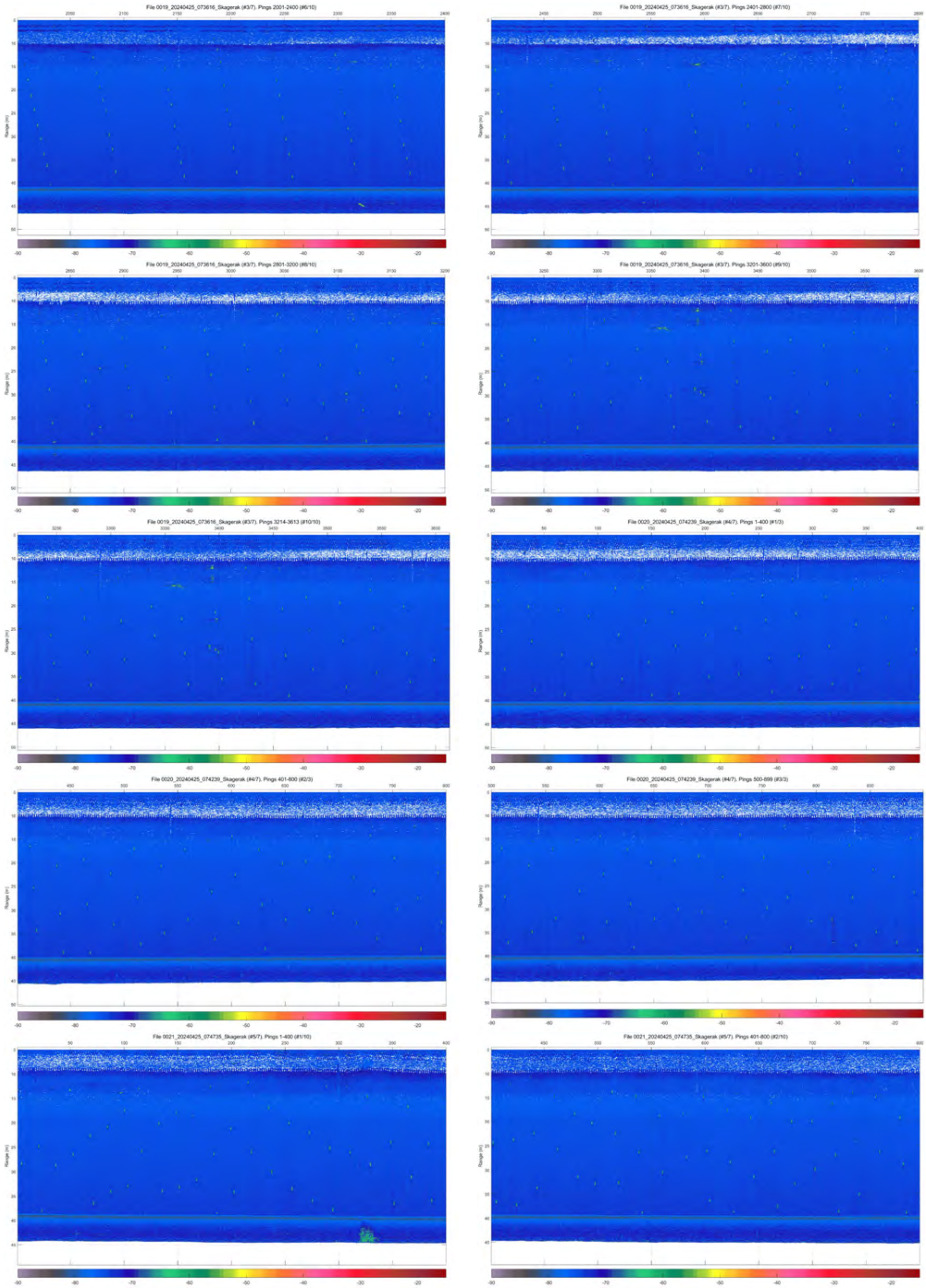
File 0019_20240425_073616_Skagerak (#3/7). Pings 2001-2400 (#6/10)
File 0019_20240425_073616_Skagerak (#3/7). Pings 2401-2800 (#7/10)
File 0019_20240425_073616_Skagerak (#3/7). Pings 2801-3200 (#8/10)
File 0019_20240425_073616_Skagerak (#3/7). Pings 3201-3600 (#9/10)
File 0019_20240425_073616_Skagerak (#3/7). Pings 3214-3613 (#10/10)
File 0020_20240425_074239_Skagerak (#4/7). Pings 1-400 (#1/3)
File 0020_20240425_074239_Skagerak (#4/7). Pings 401-800 (#2/3)
File 0020_20240425_074239_Skagerak (#4/7). Pings 500-899 (#3/3)
File 0021_20240425_074735_Skagerak (#5/7). Pings 1-400 (#1/10)
File 0021_20240425_074735_Skagerak (#5/7). Pings 401-800 (#2/10)
Range (m)

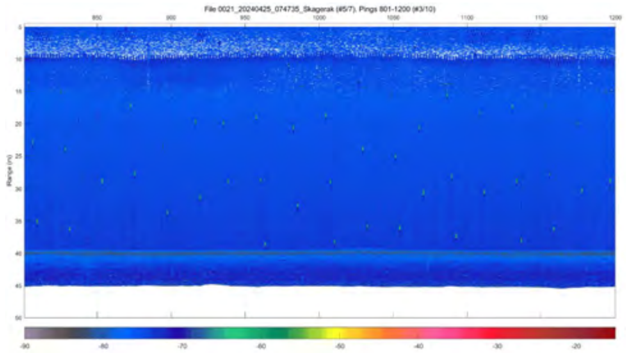
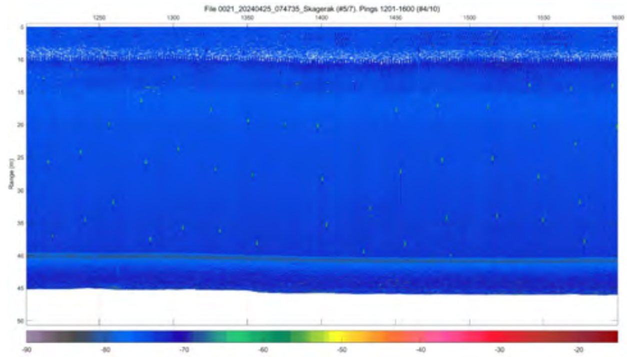
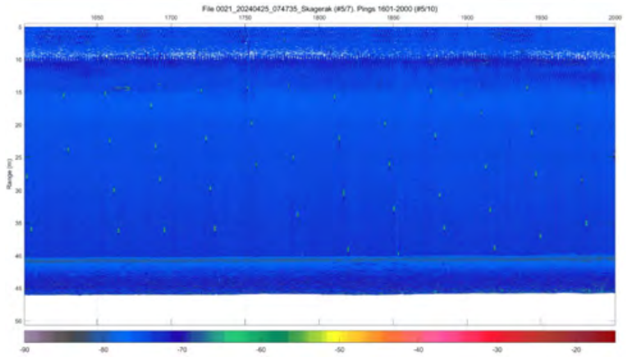
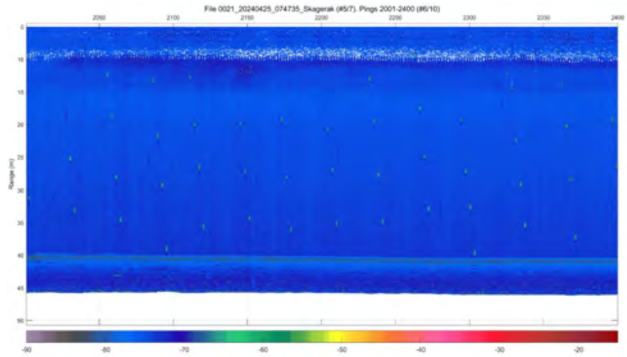
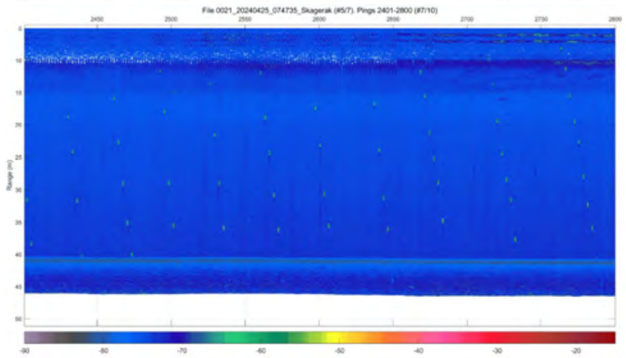
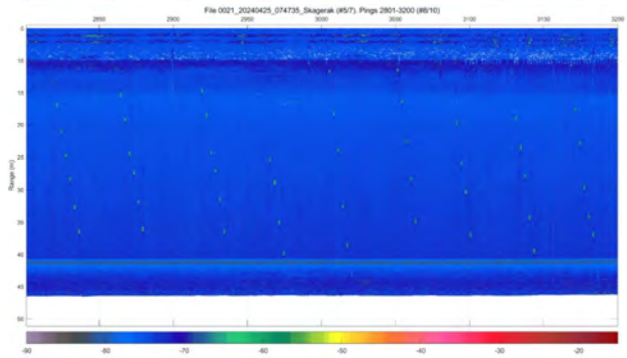
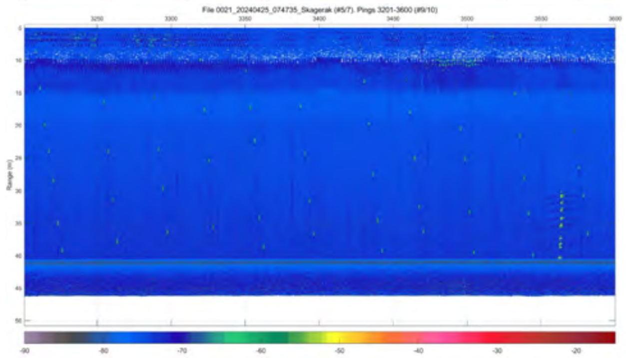
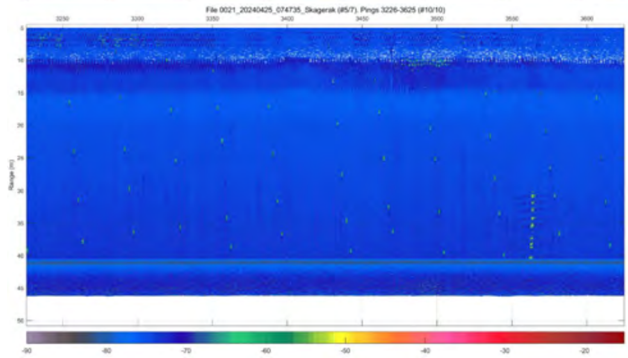
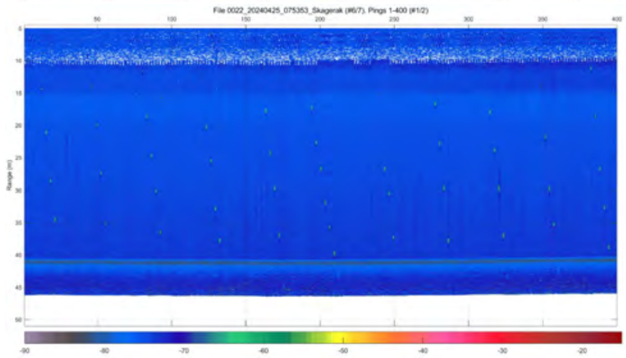
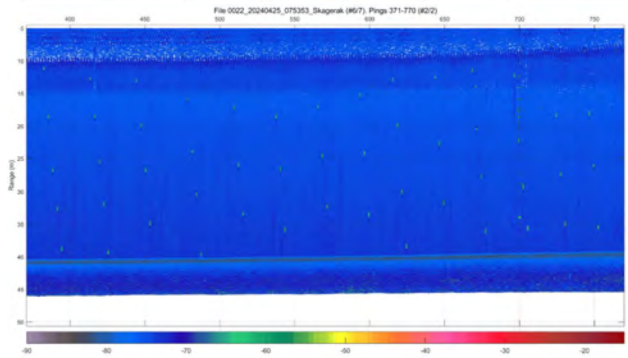

Skåne

Area 1:

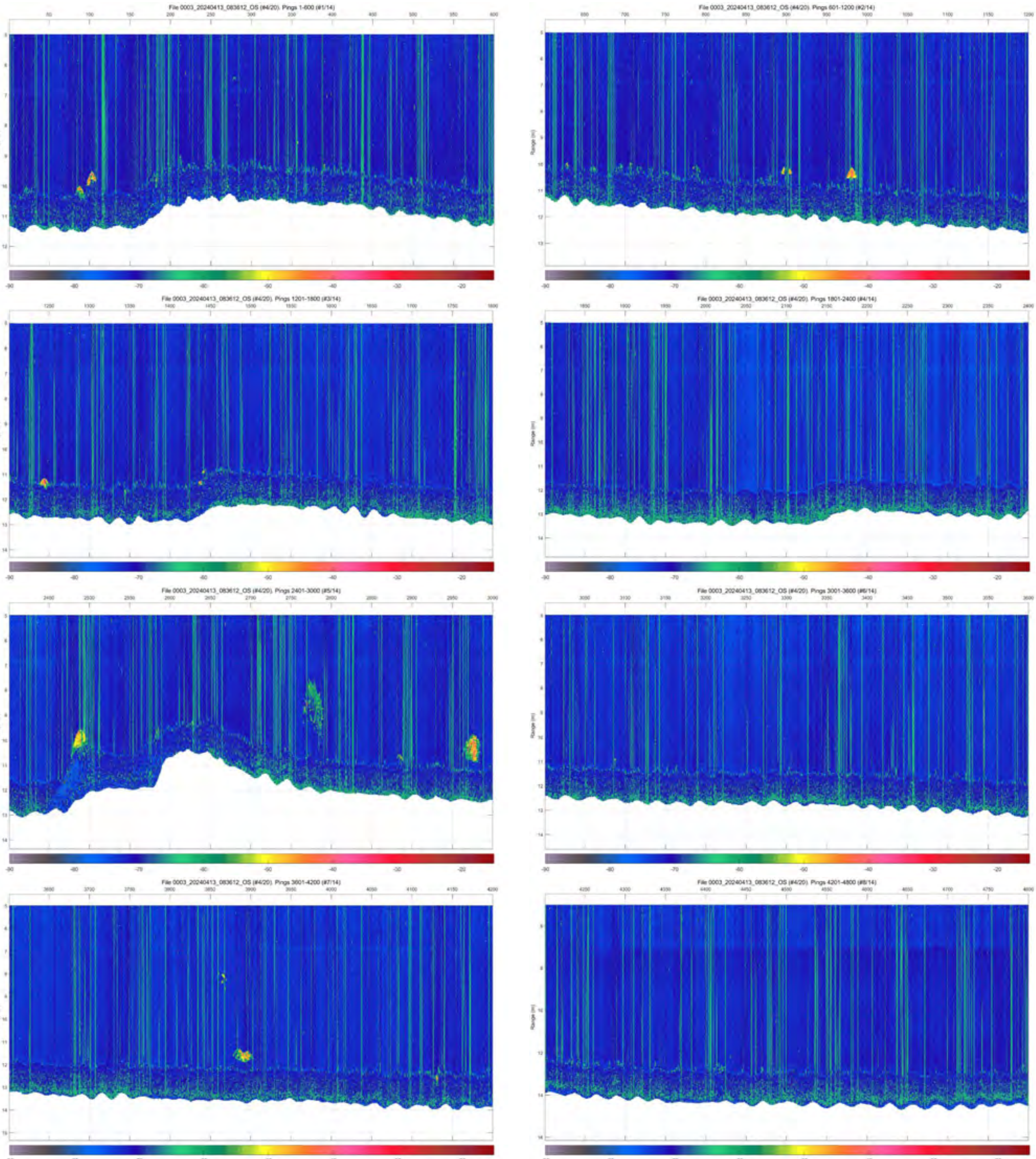

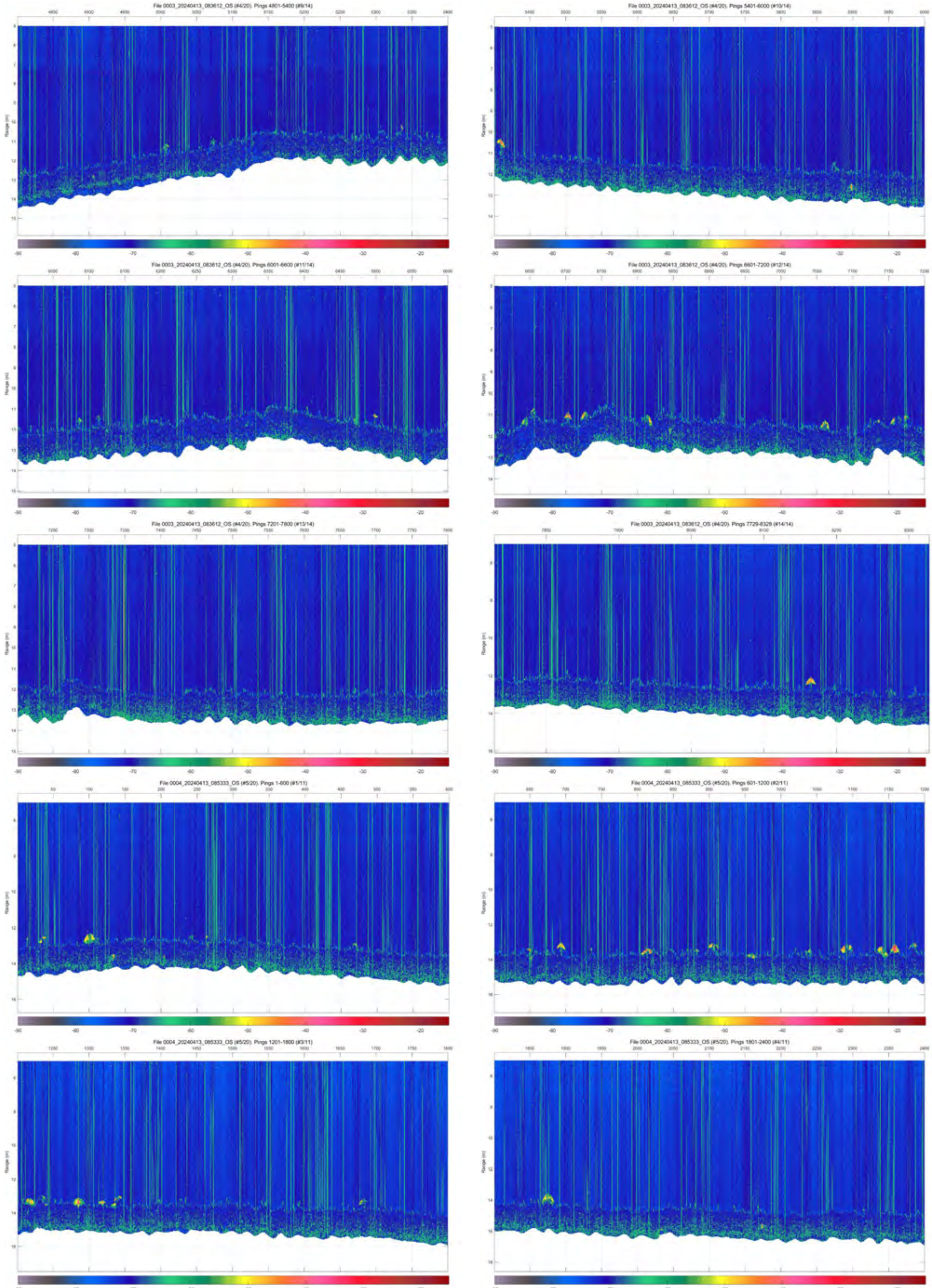
File 0003_20240413_083612_OS (#4/20). Pings 4801-5400 (#9/14)
File 0003_20240413_083612_OS (#4/20). Pings 5401-6000 (#10/14)
File 0003_20240413_083612_OS (#4/20). Pings 6001-6600 (#11/14)
File 0003_20240413_083612_OS (#4/20). Pings 6601-7200 (#12/14)
File 0003_20240413_083612_OS (#4/20). Pings 7201-7800 (#13/14)
File 0003_20240413_083612_OS (#4/20). Pings 7729-8328 (#14/14)
File 0004_20240413_085333_OS (#5/20). Pings 1-600 (#1/11)
File 0004_20240413_085333_OS (#5/20). Pings 601-1200 (#2/11)
File 0004_20240413_085333_OS (#5/20). Pings 1201-1800 (#3/11)
File 0004_20240413_085333_OS (#5/20). Pings 1801-2400 (#4/11)

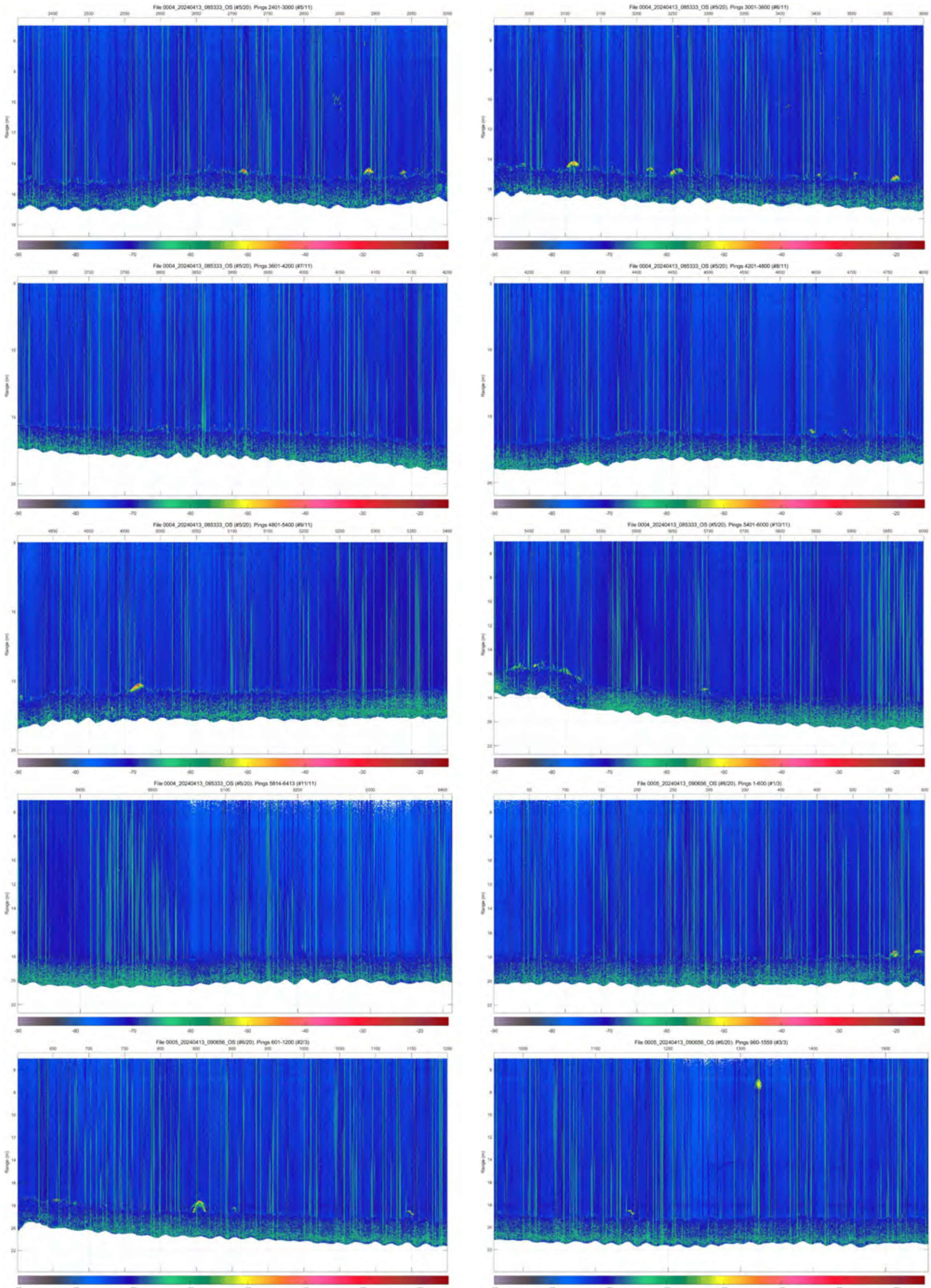
File 0004_20240413_085333_OS (#5/20). Pings 2401-3000 (#5/11)
File 0004_20240413_085333_OS (#5/20). Pings 3001-3600 (#6/11)
File 0004_20240413_085333_OS (#5/20). Pings 3601-4200 (#7/11)
File 0004_20240413_085333_OS (#5/20). Pings 4201-4800 (#8/11)
File 0004_20240413_085333_OS (#5/20). Pings 4801-5400 (#9/11)
File 0004_20240413_085333_OS (#5/20). Pings 5401-6000 (#10/11)
File 0004_20240413_085333_OS (#5/20). Pings 5814-6413 (#11/11)
File 0005_20240413_090656_OS (#6/20). Pings 1-600 (#1/3)
File 0005_20240413_090656_OS (#6/20). Pings 601-1200 (#2/3)
File 0005_20240413_090656_OS (#6/20). Pings 960-1559 (#3/3)

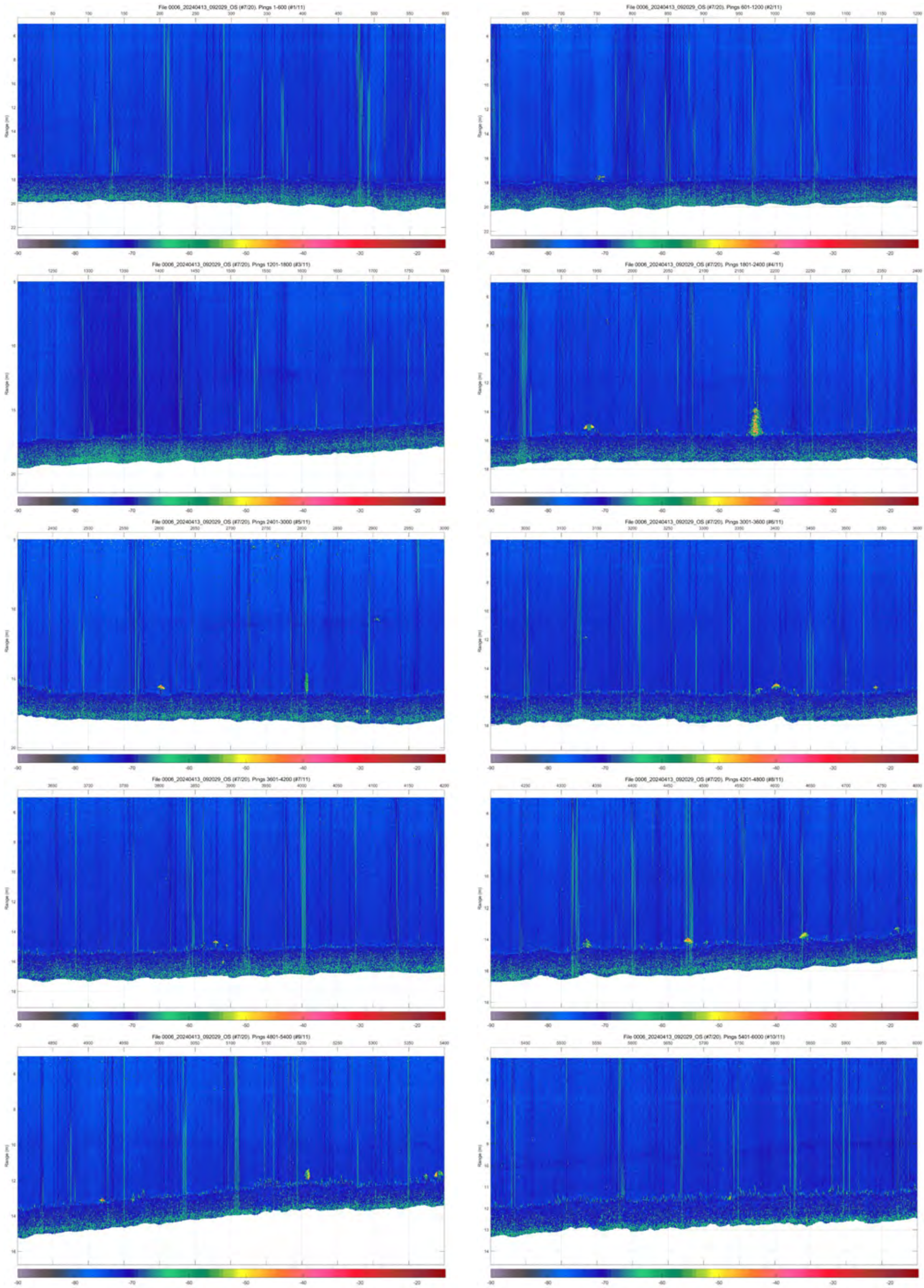
File 0006_20240413_092029_OS (#7/20). Pings 1-600 (#1/11)
File 0006_20240413_092029_OS (#7/20). Pings 601-1200 (#2/11)
File 0006_20240413_092029_OS (#7/20). Pings 1201-1800 (#3/11)
File 0006_20240413_092029_OS (#7/20). Pings 1801-2400 (#4/11)
File 0006_20240413_092029_OS (#7/20). Pings 2401-3000 (#5/11)
File 0006_20240413_092029_OS (#7/20). Pings 3001-3600 (#6/11)
File 0006_20240413_092029_OS (#7/20). Pings 3601-4200 (#7/11)
File 0006_20240413_092029_OS (#7/20). Pings 4201-4800 (#8/11)
File 0006_20240413_092029_OS (#7/20). Pings 4801-5400 (#9/11)
File 0006_20240413_092029_OS (#7/20). Pings 5401-6000 (#10/11)
Range (m)

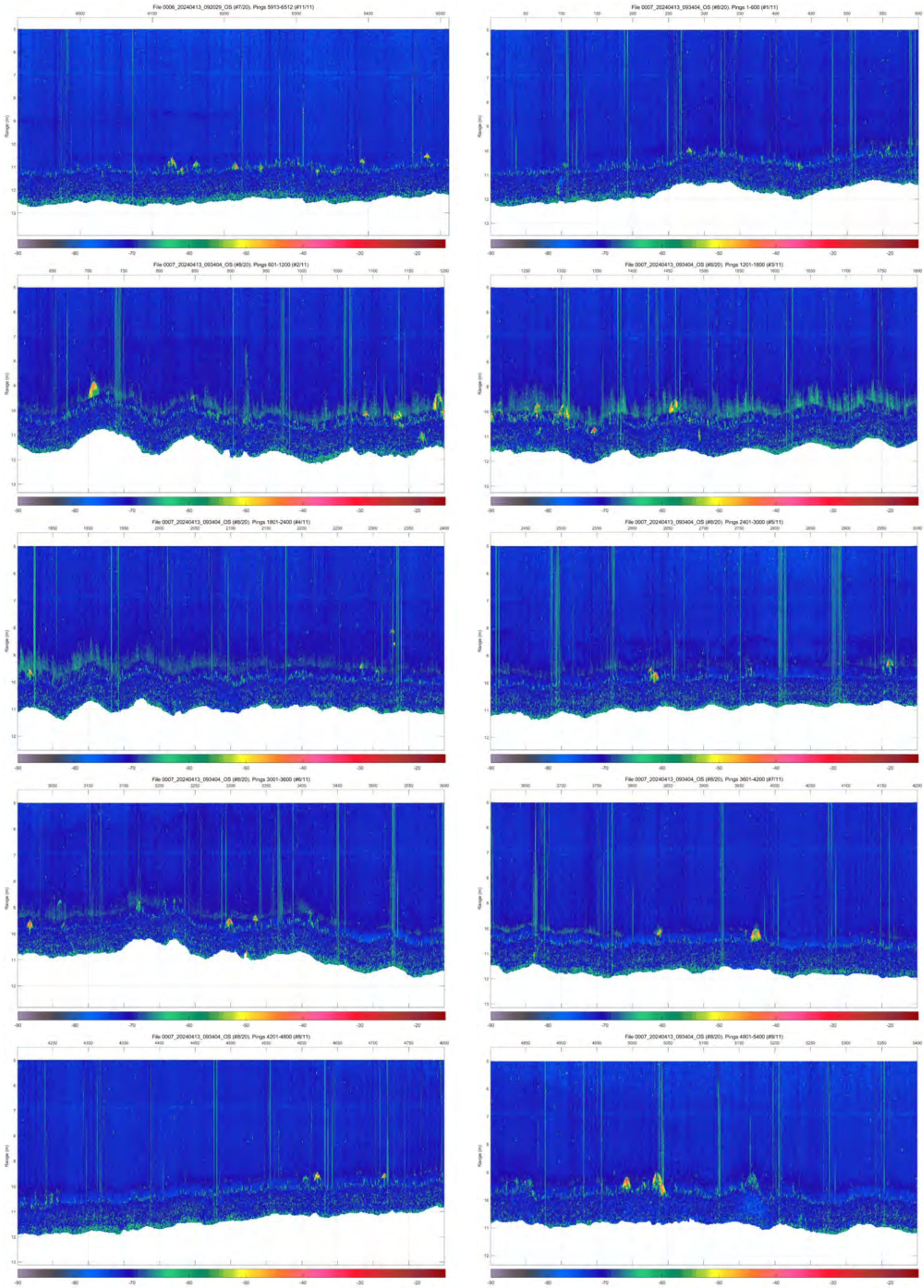

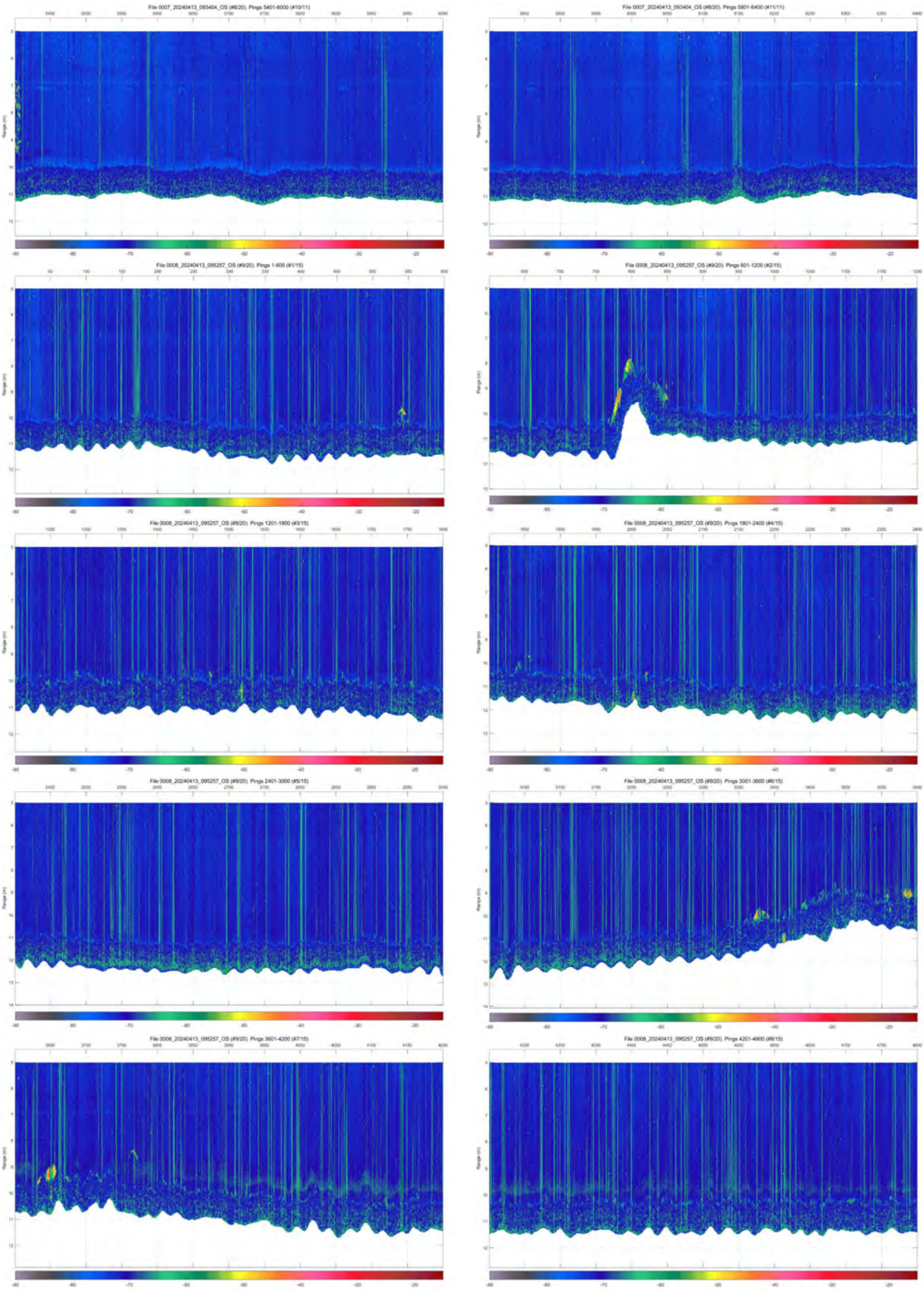
File 0007_20240413_093404_OS (#8/20). Pings 5401-6000 (#10/11)
File 0007_20240413_093404_OS (#8/20). Pings 5801-6400 (#11/11)
File 0008_20240413_095257_OS (#9/20). Pings 1-600 (#1/15)
File 0008_20240413_095257_OS (#9/20). Pings 601-1200 (#2/15)
File 0008_20240413_095257_OS (#9/20). Pings 1201-1800 (#3/15)
File 0008_20240413_095257_OS (#9/20). Pings 1801-2400 (#4/15)
File 0008_20240413_095257_OS (#9/20). Pings 2401-3000 (#5/15)
File 0008_20240413_095257_OS (#9/20). Pings 3001-3600 (#6/15)
File 0008_20240413_095257_OS (#9/20). Pings 3601-4200 (#7/15)
File 0008_20240413_095257_OS (#9/20). Pings 4201-4800 (#8/15)
Range (m)

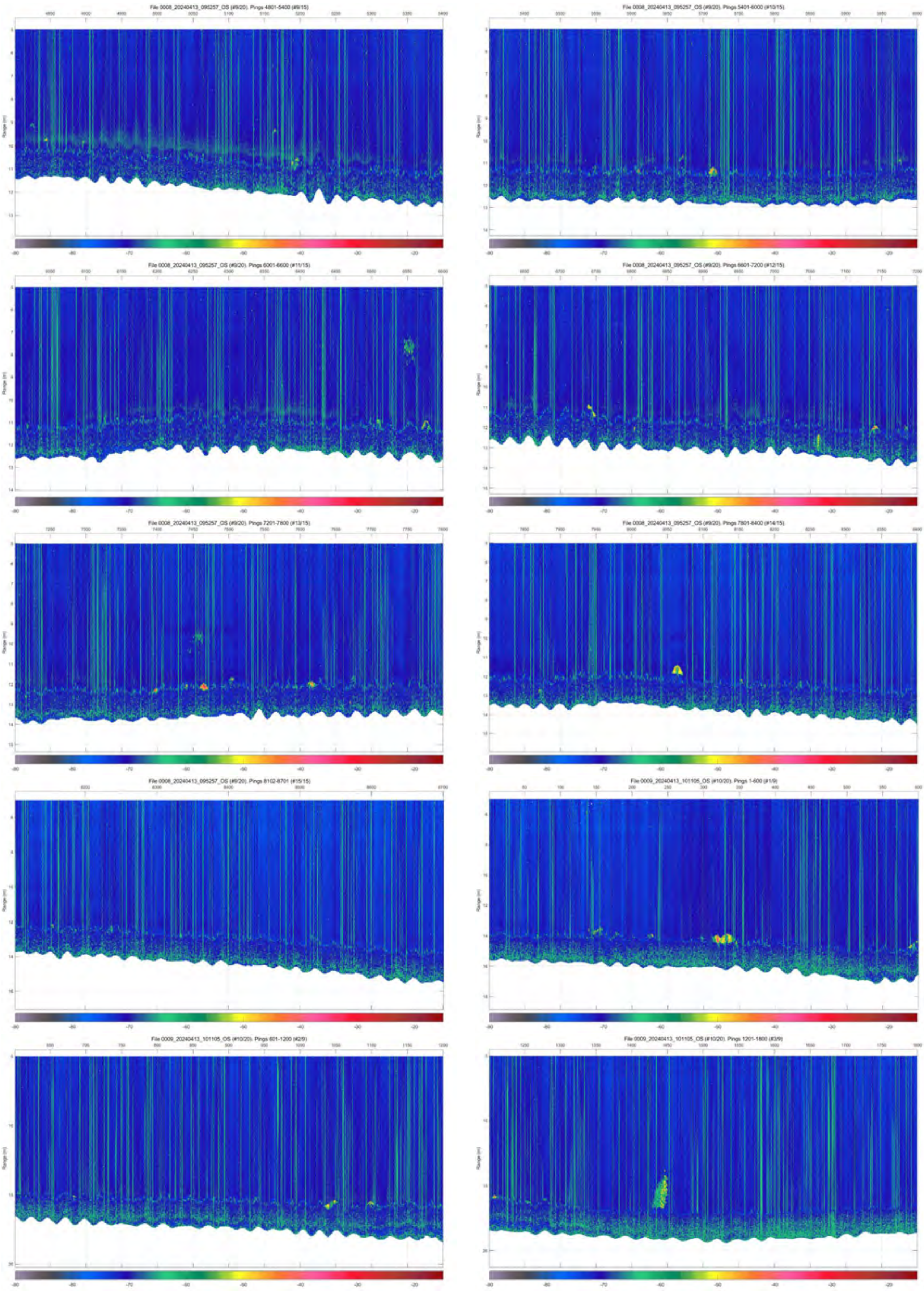

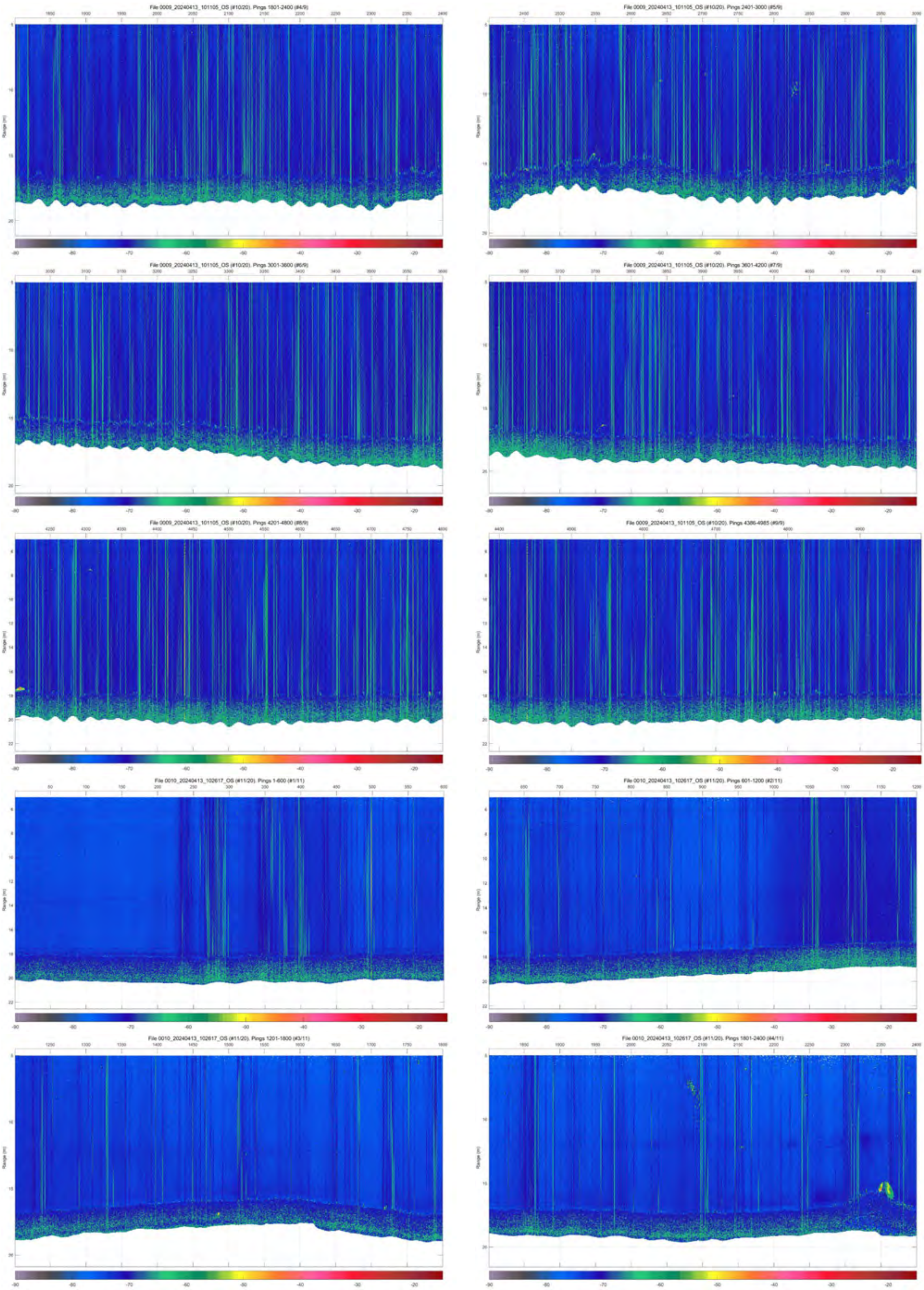

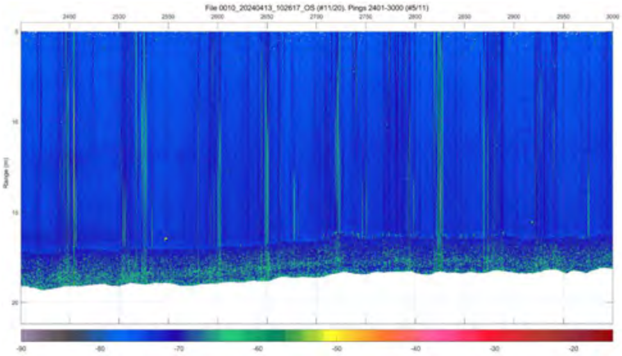
File 0010_20240413_102617_OS (#11/20). Pings 2401-3000 (#5/11)

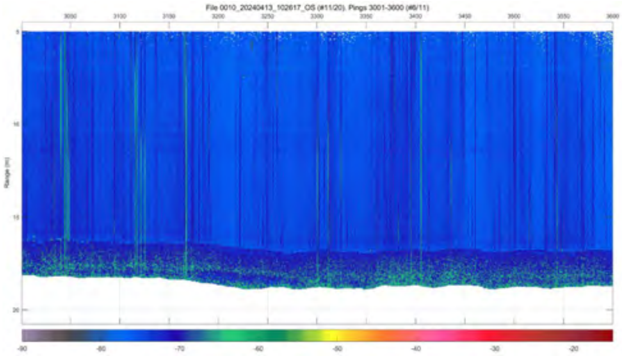
File 0010_20240413_102617_OS (#11/20). Pings 3001-3600 (#6/11)

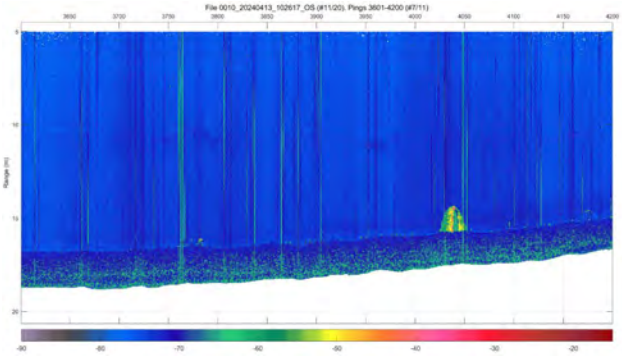
File 0010_20240413_102617_OS (#11/20). Pings 3601-4200 (#7/11)

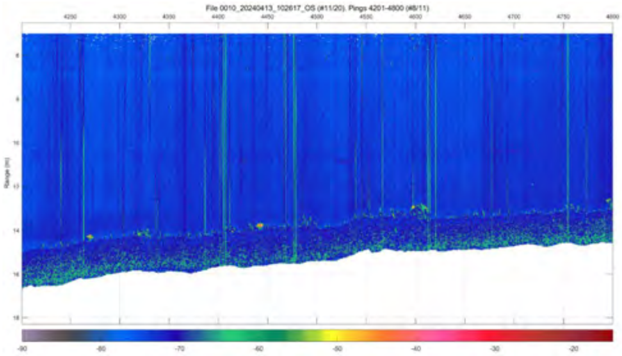
File 0010_20240413_102617_OS (#11/20). Pings 4201-4800 (#8/11)

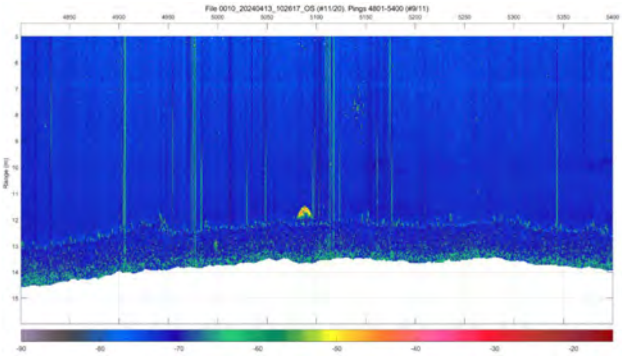
File 0010_20240413_102617_OS (#11/20). Pings 4801-5400 (#9/11)

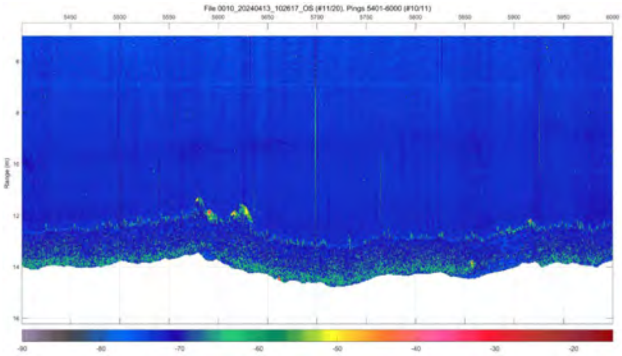
File 0010_20240413_102617_OS (#11/20). Pings 5401-6000 (#10/11)

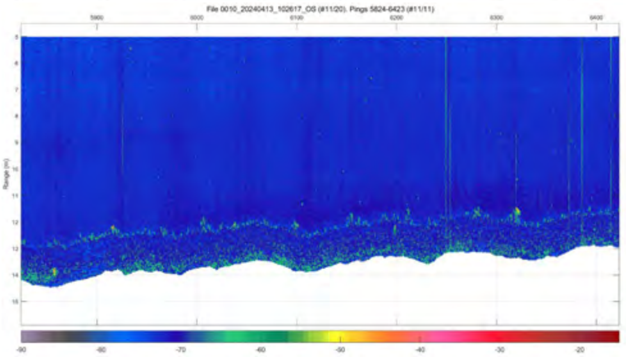
File 0010_20240413_102617_OS (#11/20). Pings 5824-6423 (#11/11)

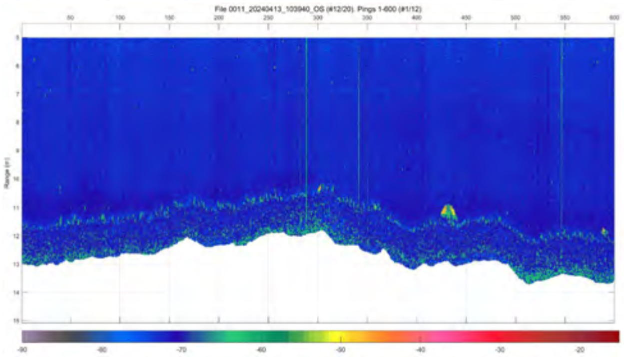
File 0011_20240413_103940_OS (#12/20). Pings 1-600 (#1/12)

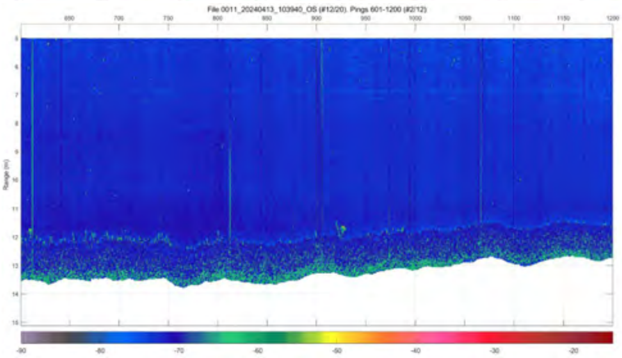
File 0011_20240413_103940_OS (#12/20). Pings 601-1200 (#2/12)

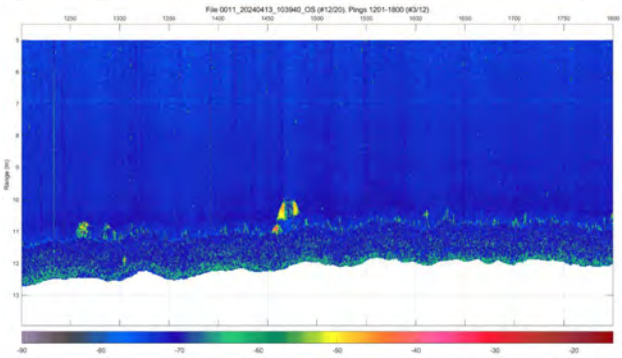
File 0011_20240413_103940_OS (#12/20). Pings 1201-1800 (#3/12)

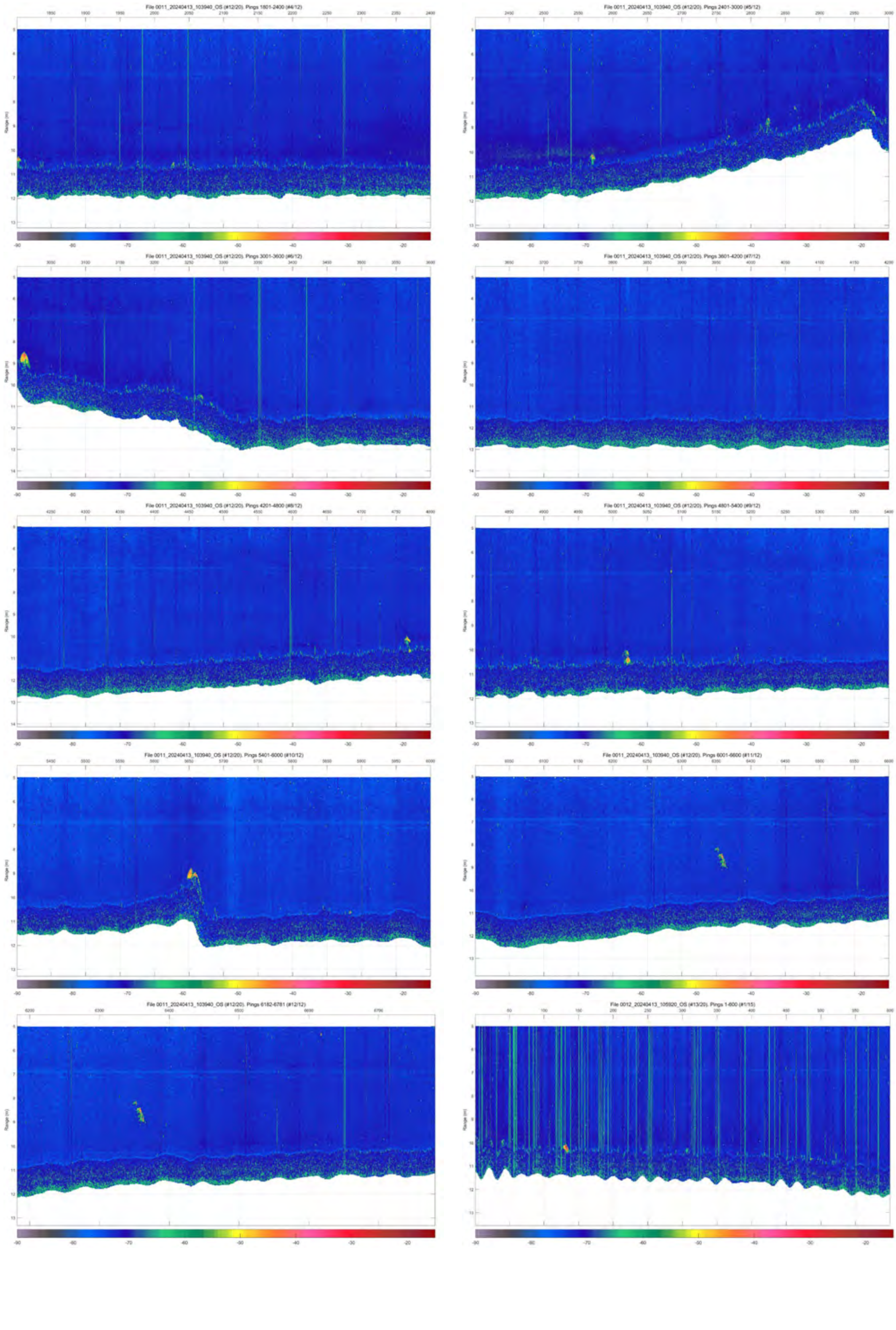

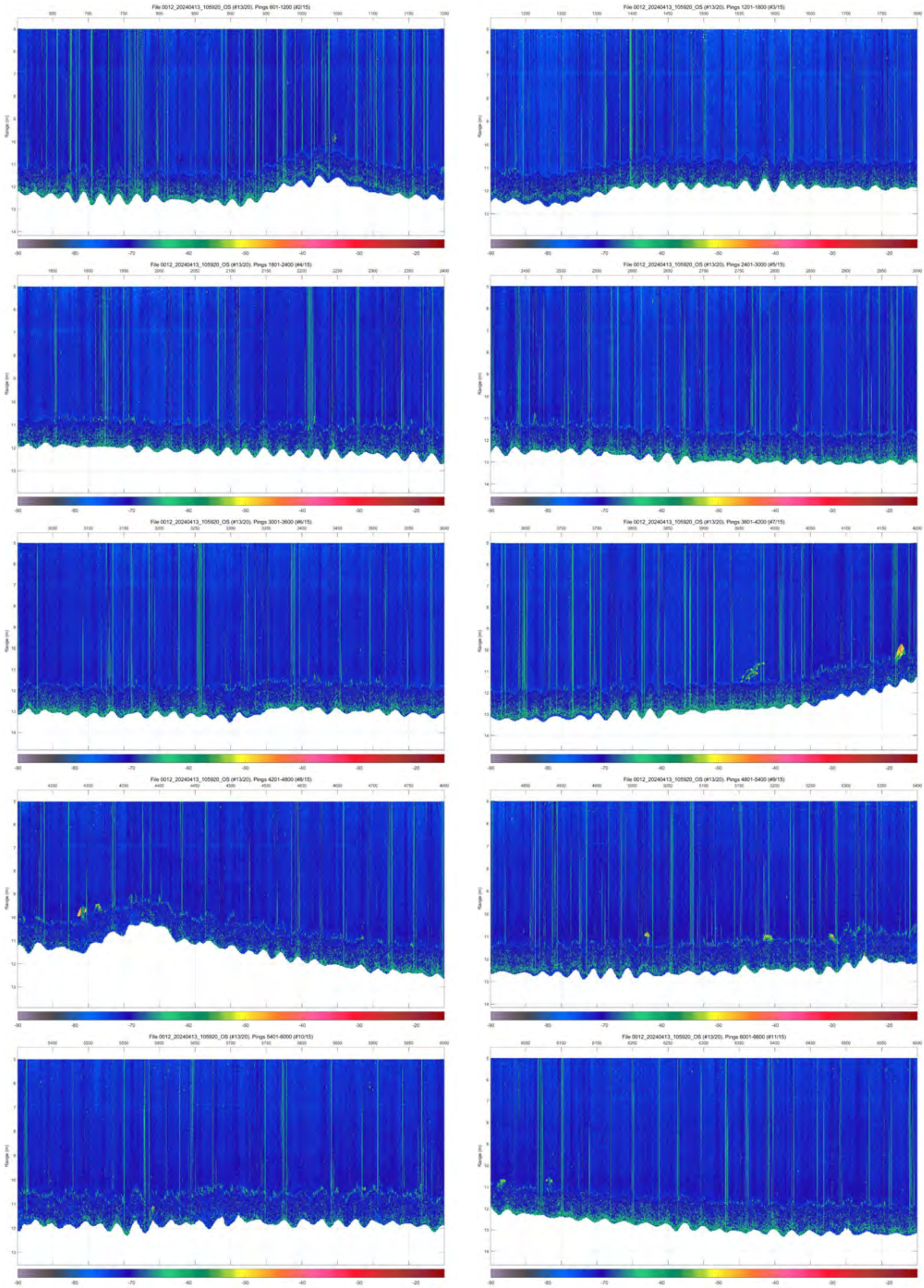

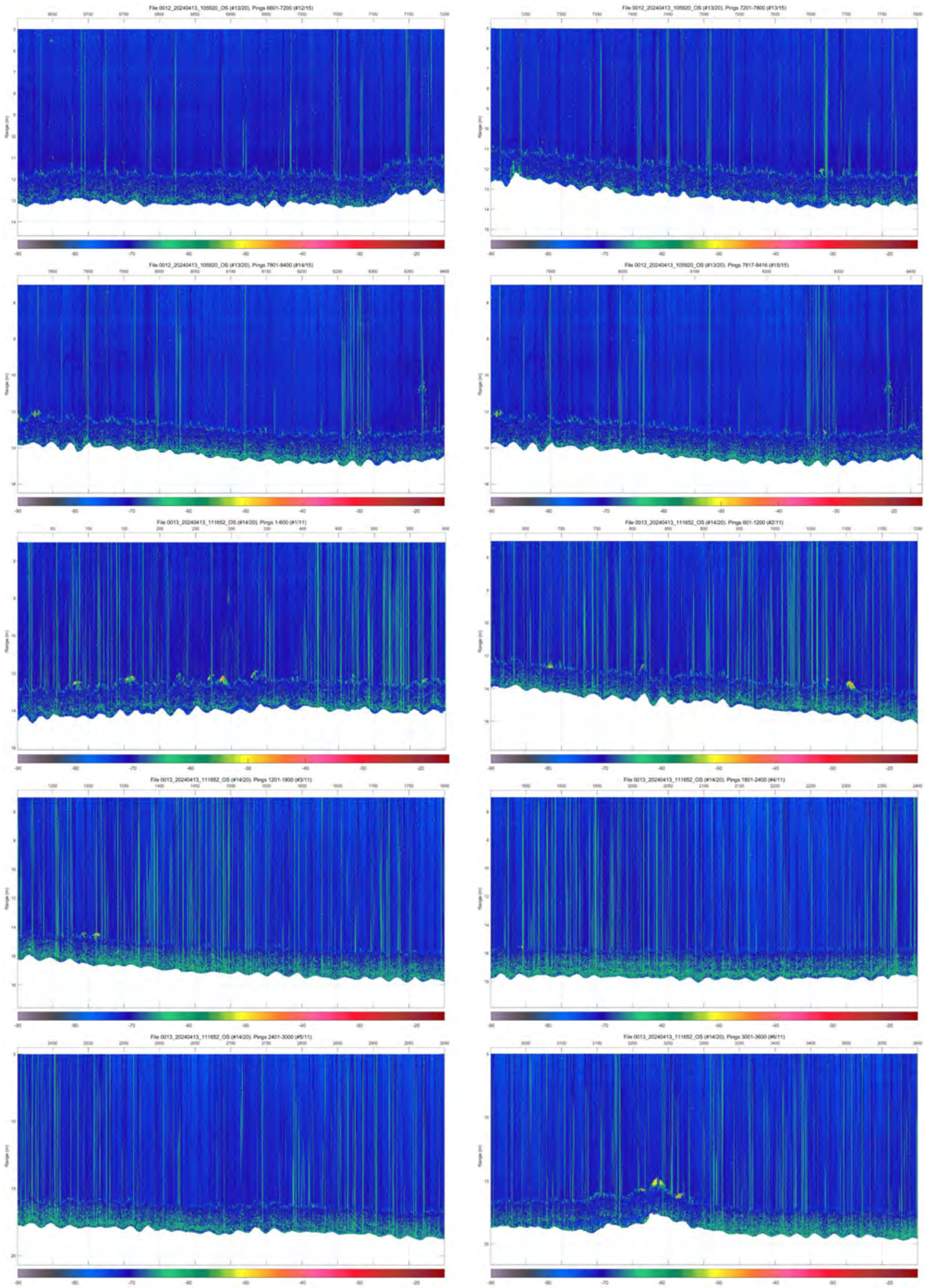
File 0012_20240413_105920_OS (#13/20). Pings 6601-7200 (#12/15)
File 0012_20240413_105920_OS (#13/20). Pings 7201-7800 (#13/15)
File 0012_20240413_105920_OS (#13/20). Pings 7801-8400 (#14/15)
File 0012_20240413_105920_OS (#13/20). Pings 7817-8416 (#15/15)
File 0013_20240413_111652_OS (#14/20). Pings 1-600 (#1/11)
File 0013_20240413_111652_OS (#14/20). Pings 601-1200 (#2/11)
File 0013_20240413_111652_OS (#14/20). Pings 1201-1800 (#3/11)
File 0013_20240413_111652_OS (#14/20). Pings 1801-2400 (#4/11)
File 0013_20240413_111652_OS (#14/20). Pings 2401-3000 (#5/11)
File 0013_20240413_111652_OS (#14/20). Pings 3001-3600 (#6/11)

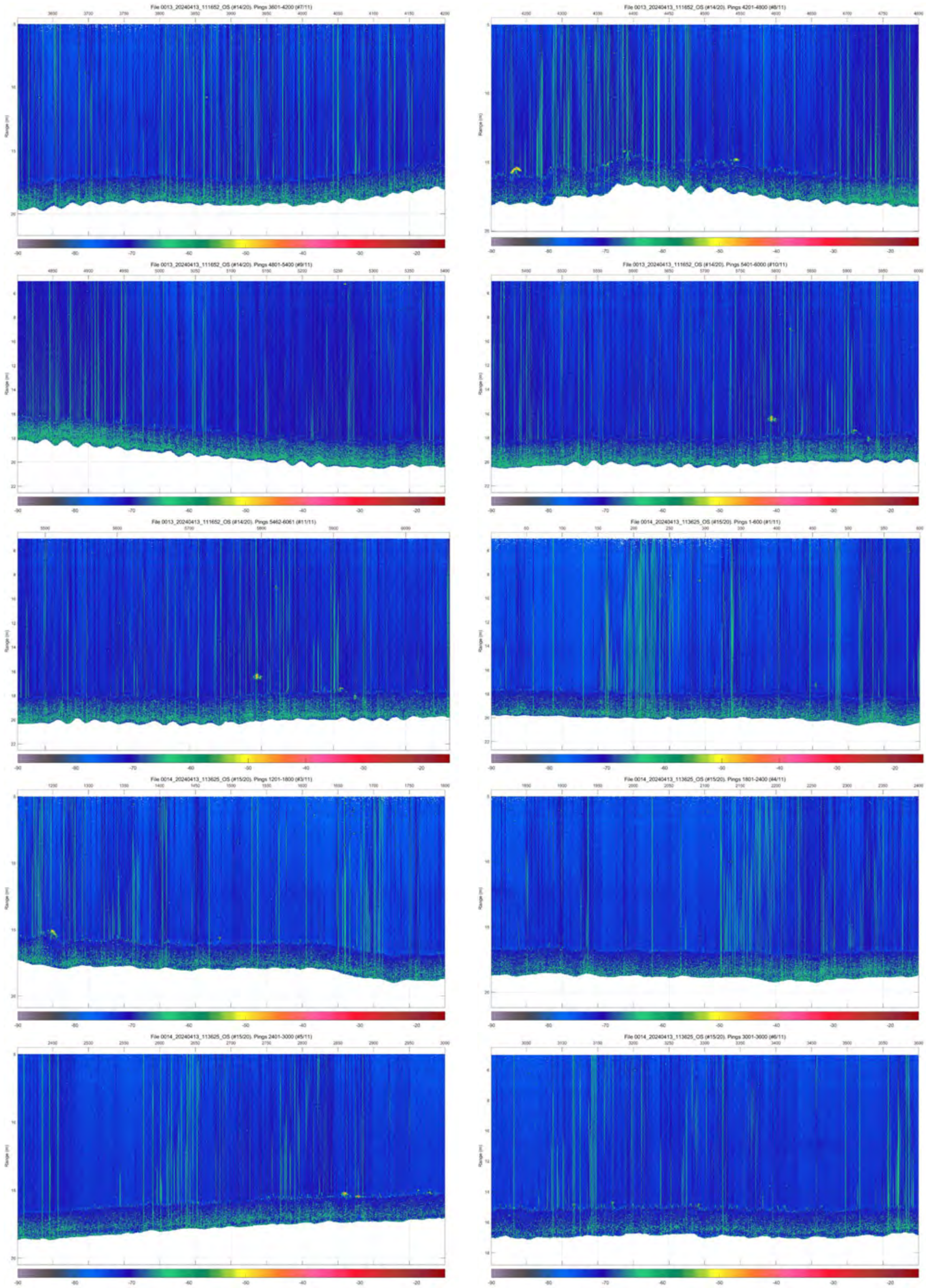
File 0013_20240413_111652_OS (#14/20). Pings 3601-4200 (#7/11)
File 0013_20240413_111652_OS (#14/20). Pings 4201-4800 (#8/11)
File 0013_20240413_111652_OS (#14/20). Pings 4801-5400 (#9/11)
File 0013_20240413_111652_OS (#14/20). Pings 5401-6000 (#10/11)
File 0013_20240413_111652_OS (#14/20). Pings 5462-6061 (#11/11)
File 0014_20240413_113625_OS (#15/20). Pings 1-600 (#1/11)
File 0014_20240413_113625_OS (#15/20). Pings 1201-1800 (#3/11)
File 0014_20240413_113625_OS (#15/20). Pings 1801-2400 (#4/11)
File 0014_20240413_113625_OS (#15/20). Pings 2401-3000 (#5/11)
File 0014_20240413_113625_OS (#15/20). Pings 3001-3600 (#6/11)

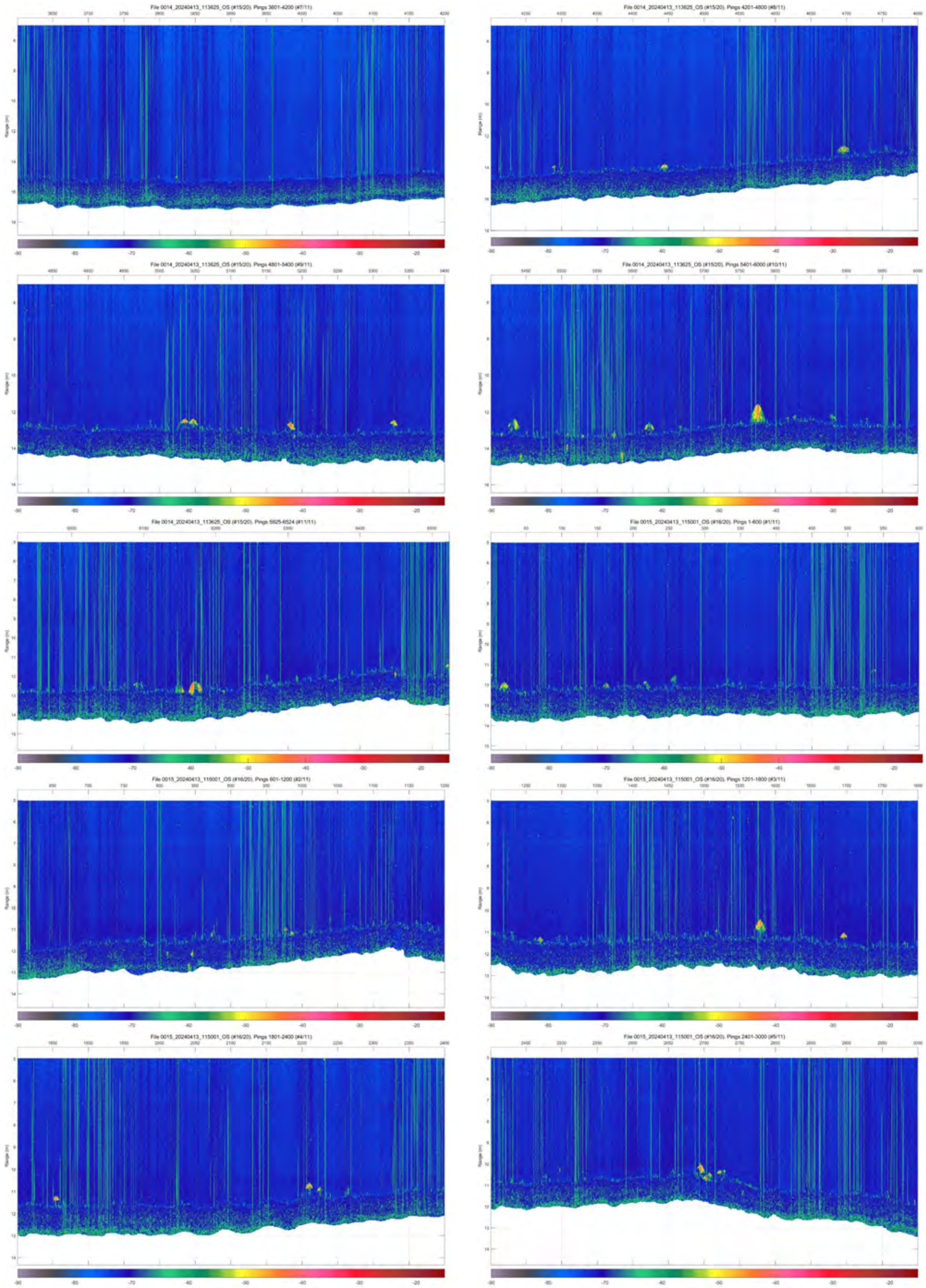
File 0014_20240413_113625_OS (#15/20). Pings 3601-4200 (#7/11)
File 0014_20240413_113625_OS (#15/20). Pings 4201-4800 (#8/11)
File 0014_20240413_113625_OS (#15/20). Pings 4801-5400 (#9/11)
File 0014_20240413_113625_OS (#15/20). Pings 5401-6000 (#10/11)
File 0014_20240413_113625_OS (#15/20). Pings 5925-6524 (#11/11)
File 0015_20240413_115001_OS (#16/20). Pings 1-600 (#1/11)
File 0015_20240413_115001_OS (#16/20). Pings 601-1200 (#2/11)
File 0015_20240413_115001_OS (#16/20). Pings 1201-1800 (#3/11)
File 0015_20240413_115001_OS (#16/20). Pings 1801-2400 (#4/11)
File 0015_20240413_115001_OS (#16/20). Pings 2401-3000 (#5/11)

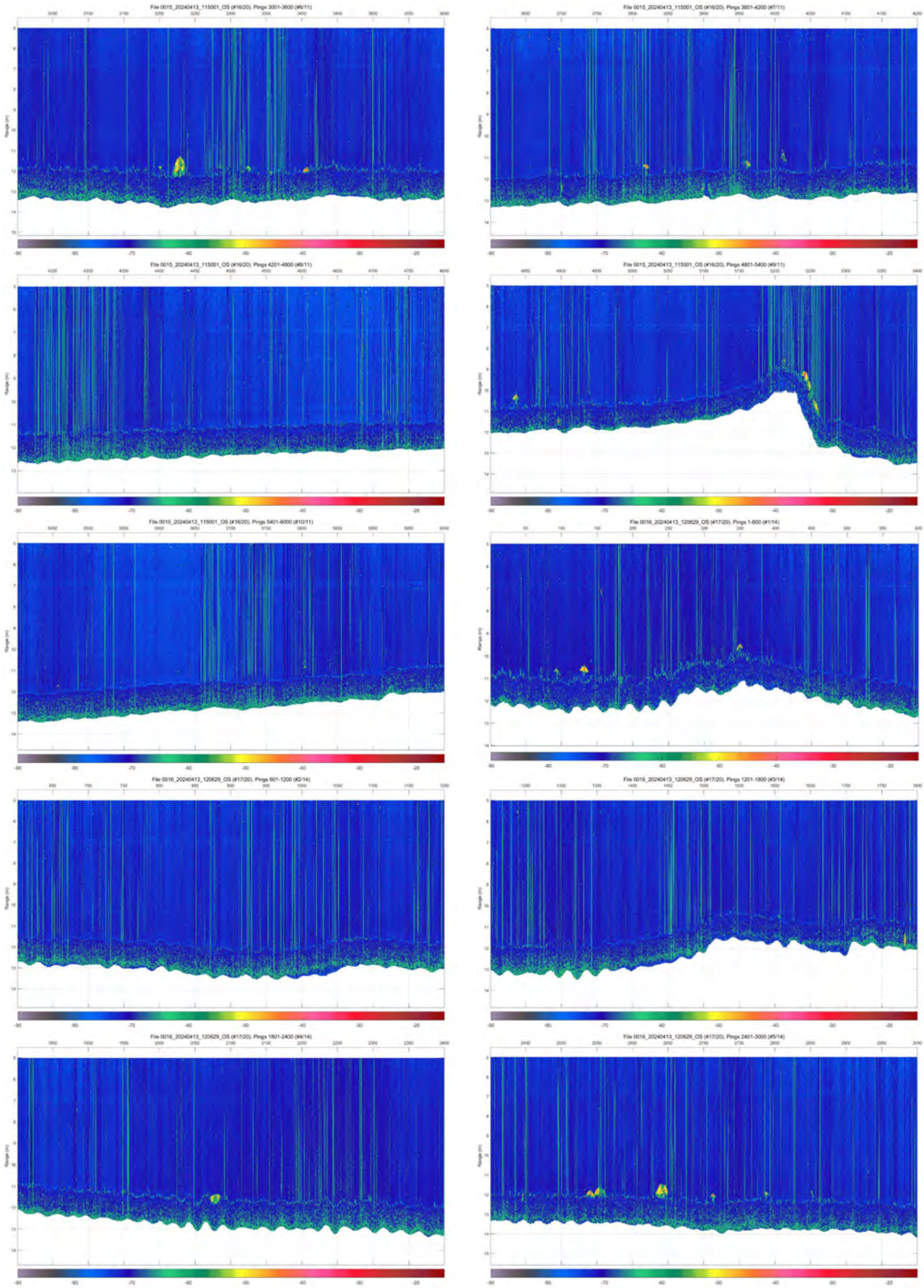

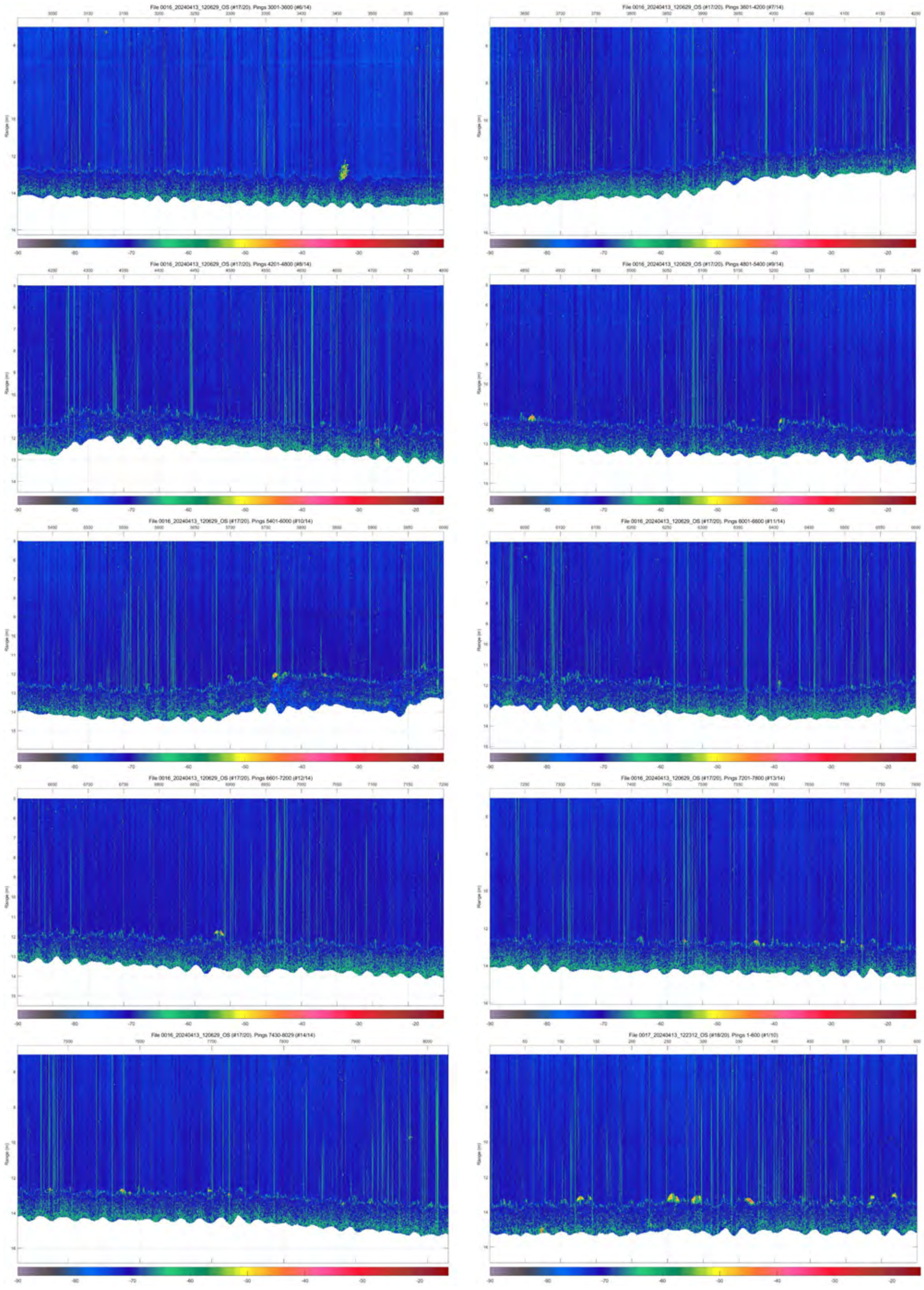
File 0016_20240413_120629_OS (#17/20). Pings 3001-3600 (#6/14)
File 0016_20240413_120629_OS (#17/20). Pings 3601-4200 (#7/14)
File 0016_20240413_120629_OS (#17/20). Pings 4201-4800 (#8/14)
File 0016_20240413_120629_OS (#17/20). Pings 4801-5400 (#9/14)
File 0016_20240413_120629_OS (#17/20). Pings 5401-6000 (#10/14)
File 0016_20240413_120629_OS (#17/20). Pings 6001-6600 (#11/14)
File 0016_20240413_120629_OS (#17/20). Pings 6601-7200 (#12/14)
File 0016_20240413_120629_OS (#17/20). Pings 7201-7800 (#13/14)
File 0016_20240413_120629_OS (#17/20). Pings 7430-8029 (#14/14)
File 0017_20240413_122312_OS (#18/20). Pings 1-600 (#1/10)

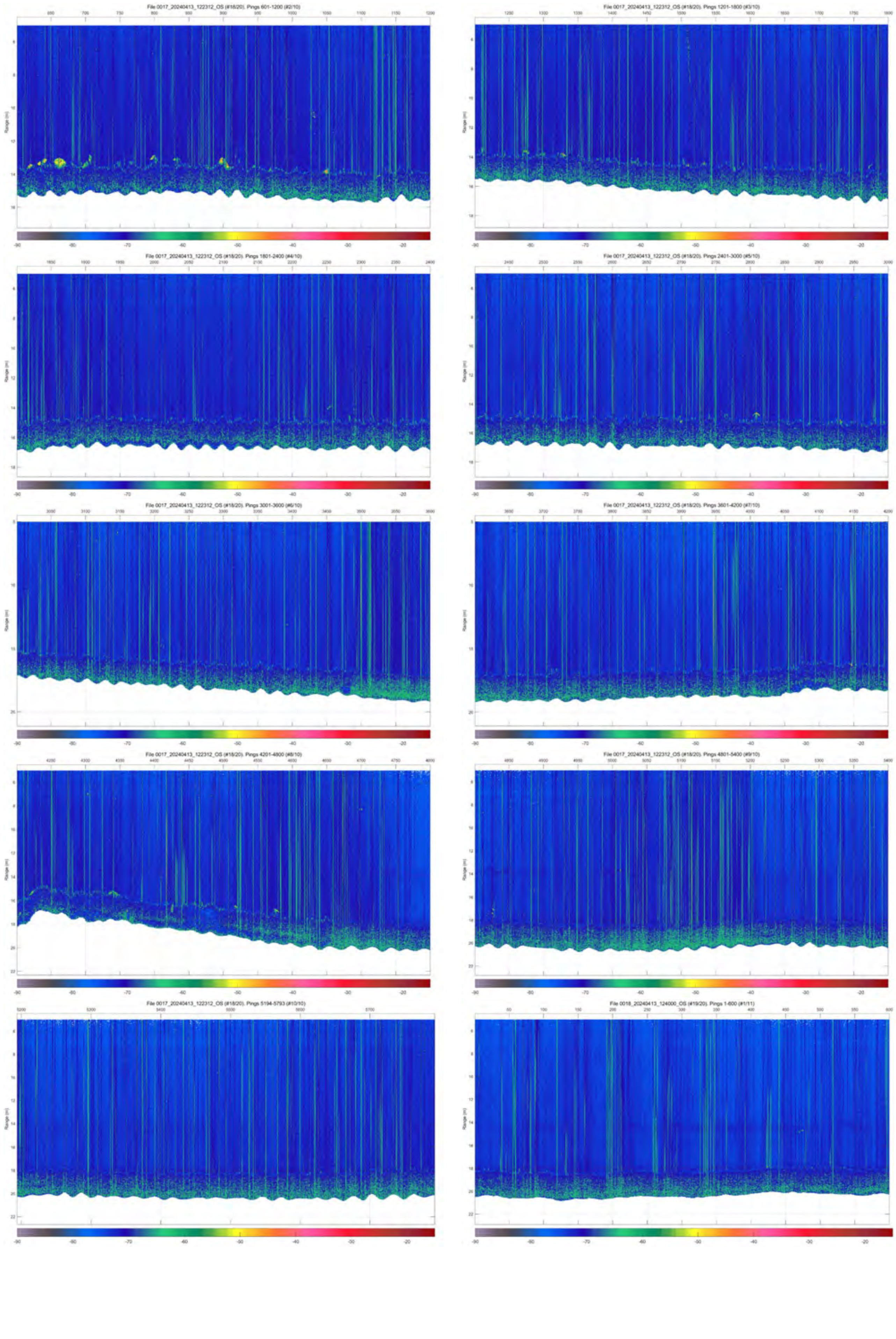

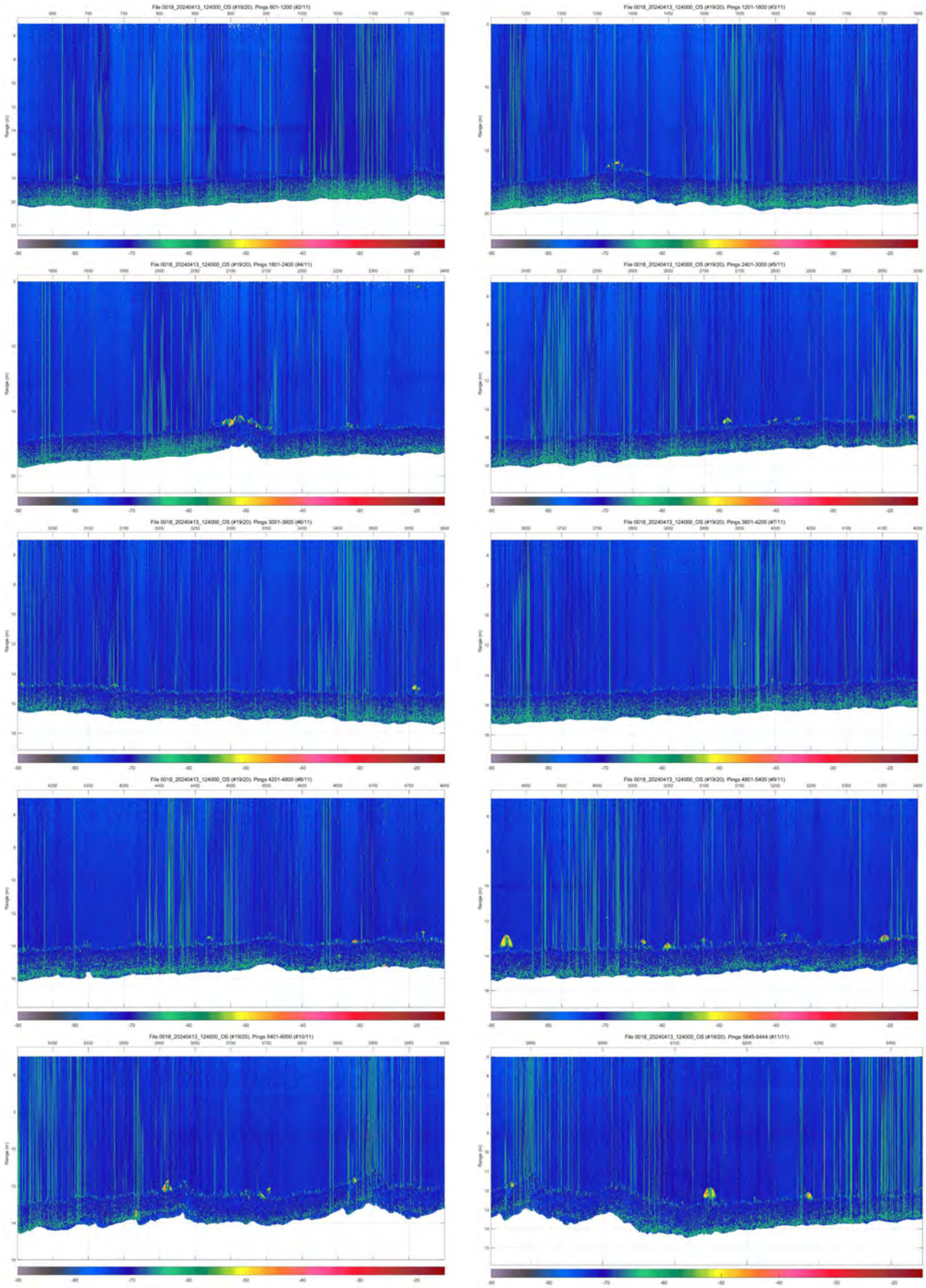
File 0018_20240413_124000_OS (#19/20). Pings 601-1200 (#2/11)
File 0018_20240413_124000_OS (#19/20). Pings 1201-1800 (#3/11)
File 0018_20240413_124000_OS (#19/20). Pings 1801-2400 (#4/11)
File 0018_20240413_124000_OS (#19/20). Pings 2401-3000 (#5/11)
File 0018_20240413_124000_OS (#19/20). Pings 3001-3600 (#6/11)
File 0018_20240413_124000_OS (#19/20). Pings 3601-4200 (#7/11)
File 0018_20240413_124000_OS (#19/20). Pings 4201-4800 (#8/11)
File 0018_20240413_124000_OS (#19/20). Pings 4801-5400 (#9/11)
File 0018_20240413_124000_OS (#19/20). Pings 5401-6000 (#10/11)
File 0018_20240413_124000_OS (#19/20). Pings 5845-6444 (#11/11)
Range (m)

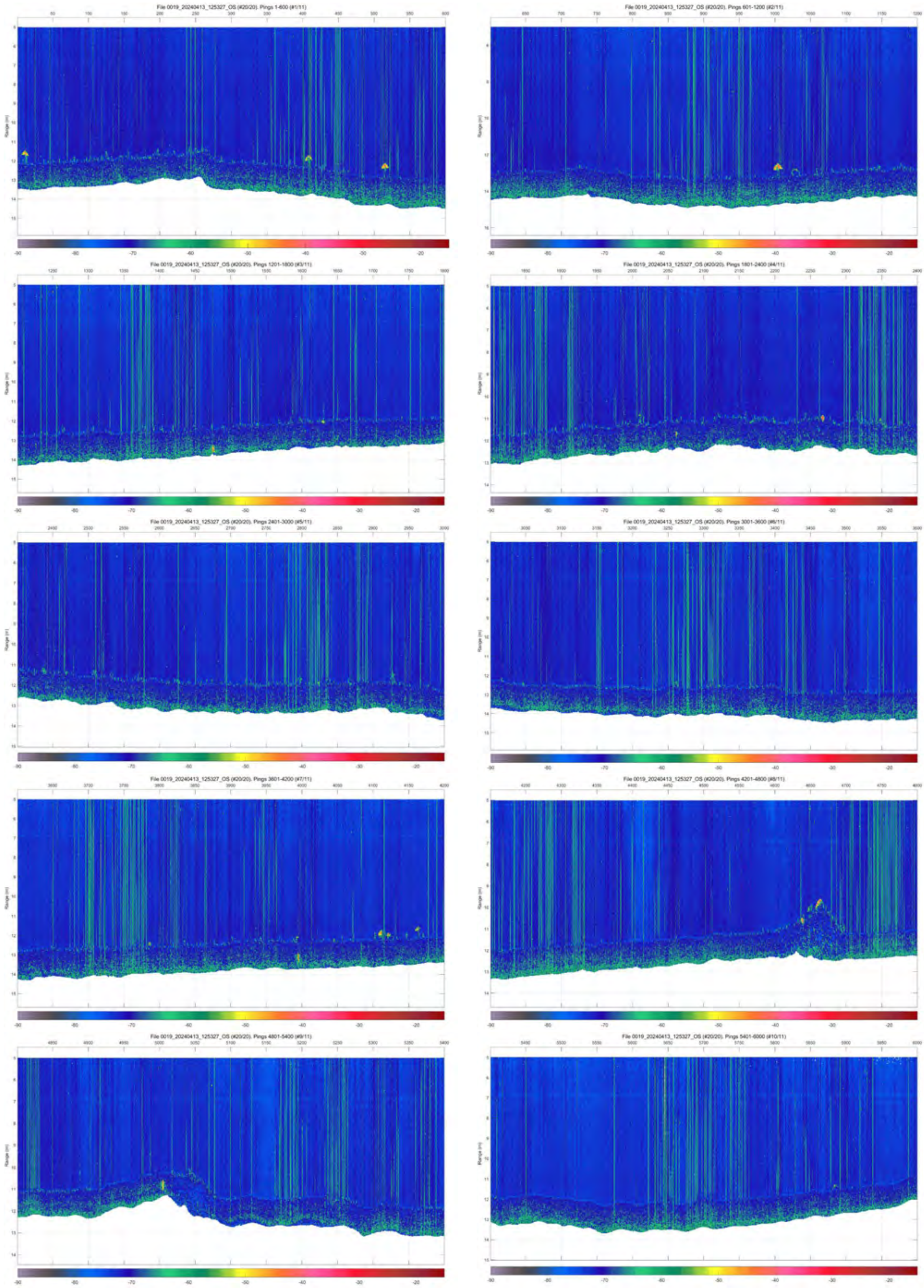
File 0019_20240413_125327_OS (#20/20). Pings 1-600 (#1/11)
File 0019_20240413_125327_OS (#20/20). Pings 601-1200 (#2/11)
File 0019_20240413_125327_OS (#20/20). Pings 1201-1800 (#3/11)
File 0019_20240413_125327_OS (#20/20). Pings 1801-2400 (#4/11)
File 0019_20240413_125327_OS (#20/20). Pings 2401-3000 (#5/11)
File 0019_20240413_125327_OS (#20/20). Pings 3001-3600 (#6/11)
File 0019_20240413_125327_OS (#20/20). Pings 3601-4200 (#7/11)
File 0019_20240413_125327_OS (#20/20). Pings 4201-4800 (#8/11)
File 0019_20240413_125327_OS (#20/20). Pings 4801-5400 (#9/11)
File 0019_20240413_125327_OS (#20/20). Pings 5401-6000 (#10/11)
Range (m)

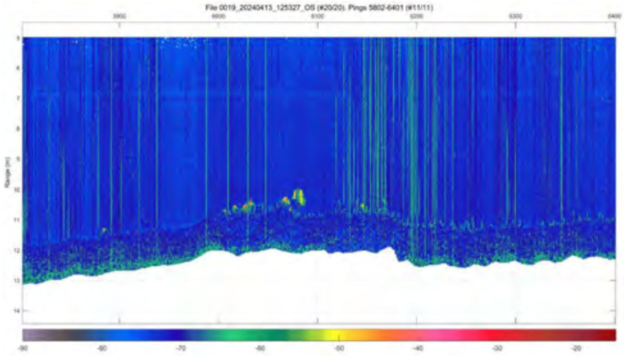

Area 2:

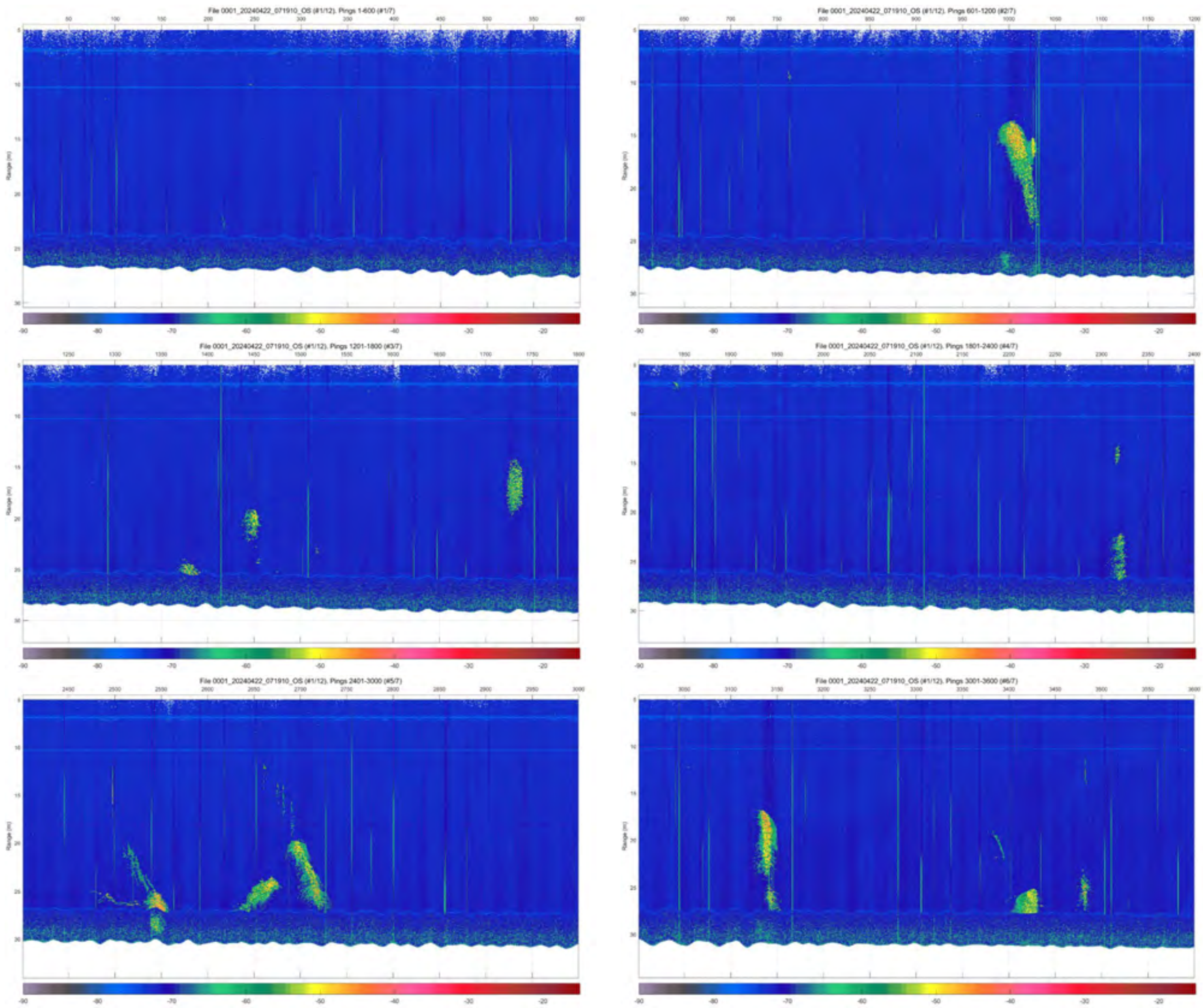

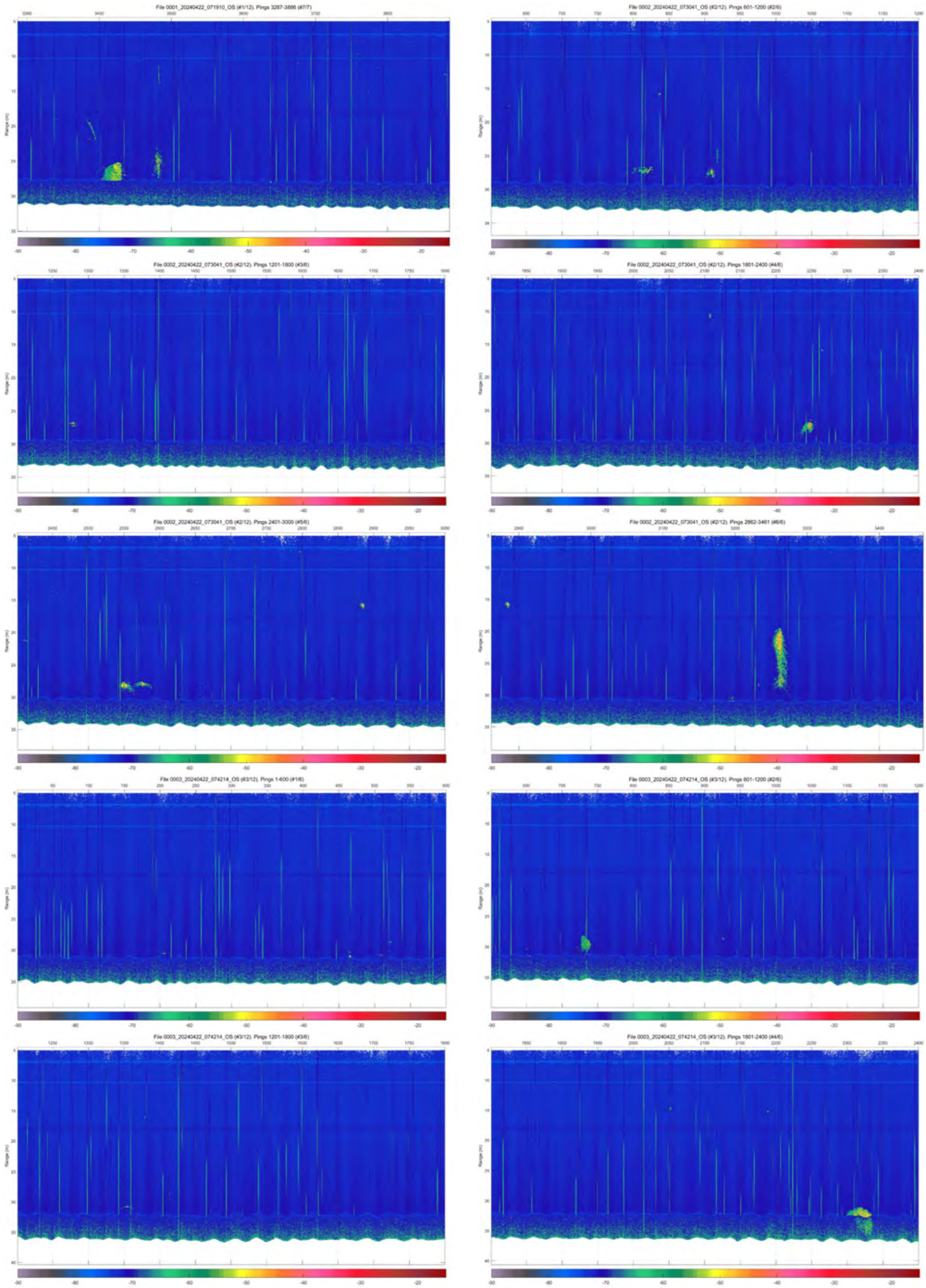

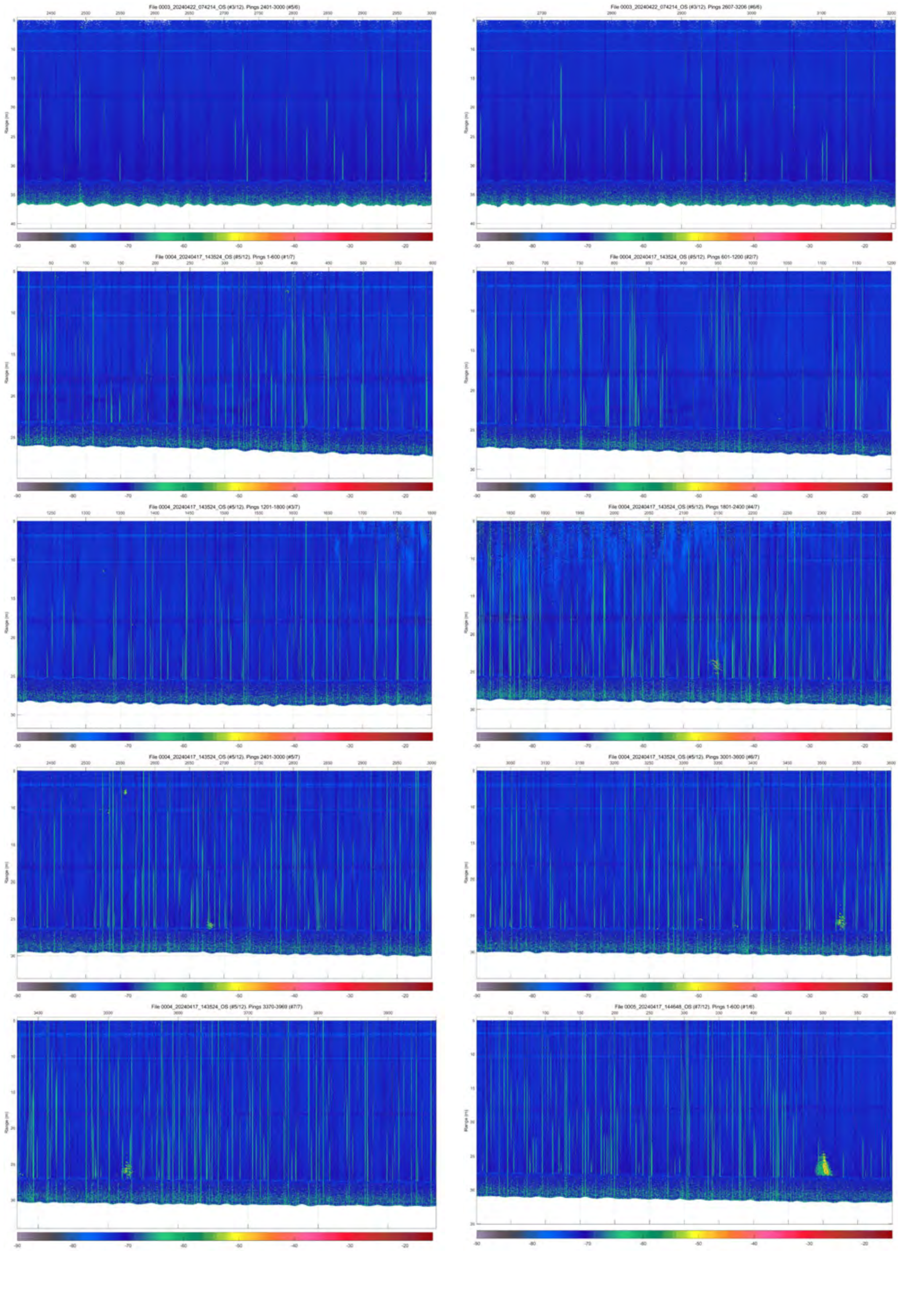
File 0003_20240422_074214_OS (#3/12). Pings 2401-3000 (#5/6)
File 0003_20240422_074214_OS (#3/12). Pings 2607-3206 (#6/6)
File 0004_20240417_143524_OS (#5/12). Pings 1-600 (#1/7)
File 0004_20240417_143524_OS (#5/12). Pings 601-1200 (#2/7)
File 0004_20240417_143524_OS (#5/12). Pings 1201-1800 (#3/7)
File 0004_20240417_143524_OS (#5/12). Pings 1801-2400 (#4/7)
File 0004_20240417_143524_OS (#5/12). Pings 2401-3000 (#5/7)
File 0004_20240417_143524_OS (#5/12). Pings 3001-3600 (#6/7)
File 0004_20240417_143524_OS (#5/12). Pings 3370-3969 (#7/7)
File 0005_20240417_144648_OS (#7/12). Pings 1-600 (#1/6)

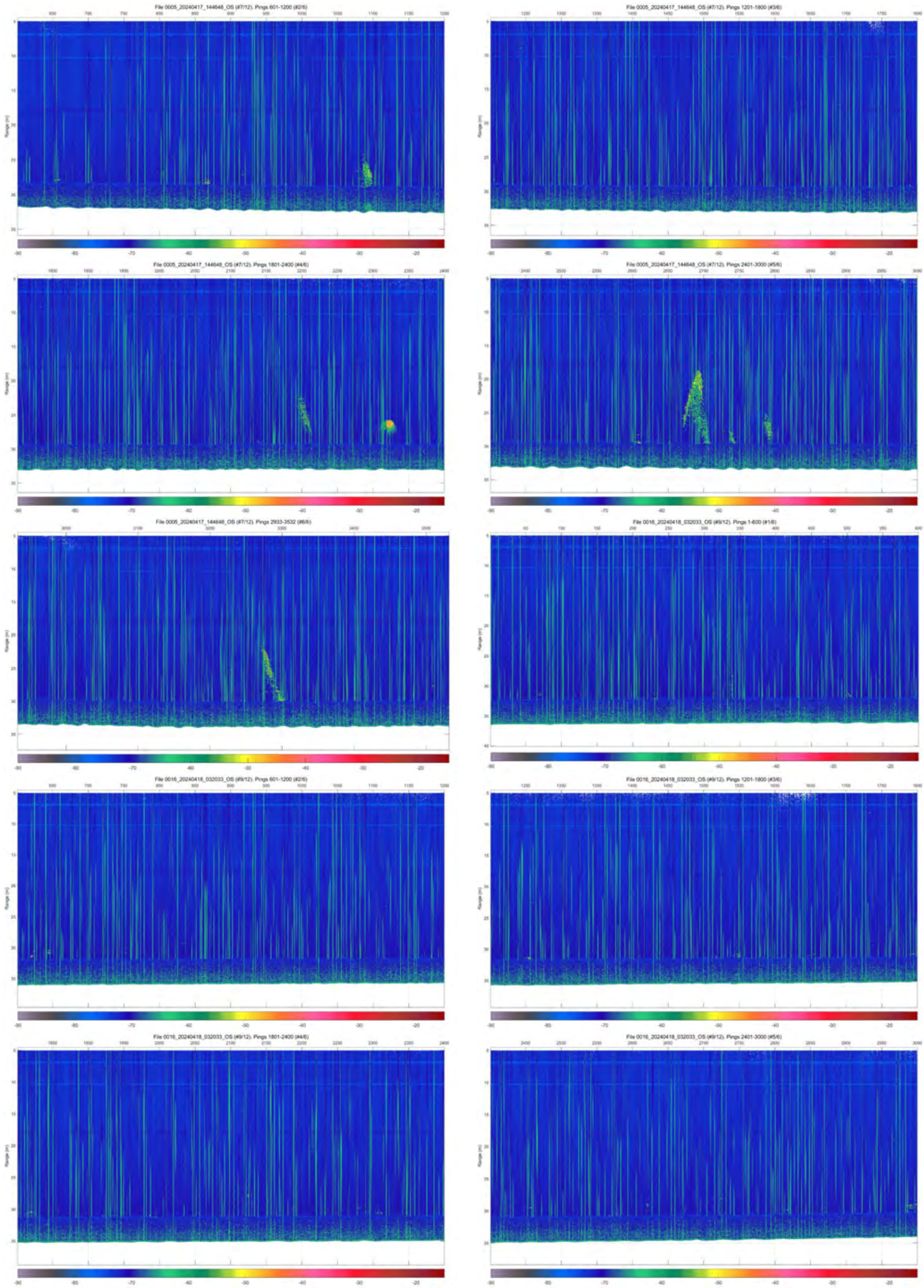

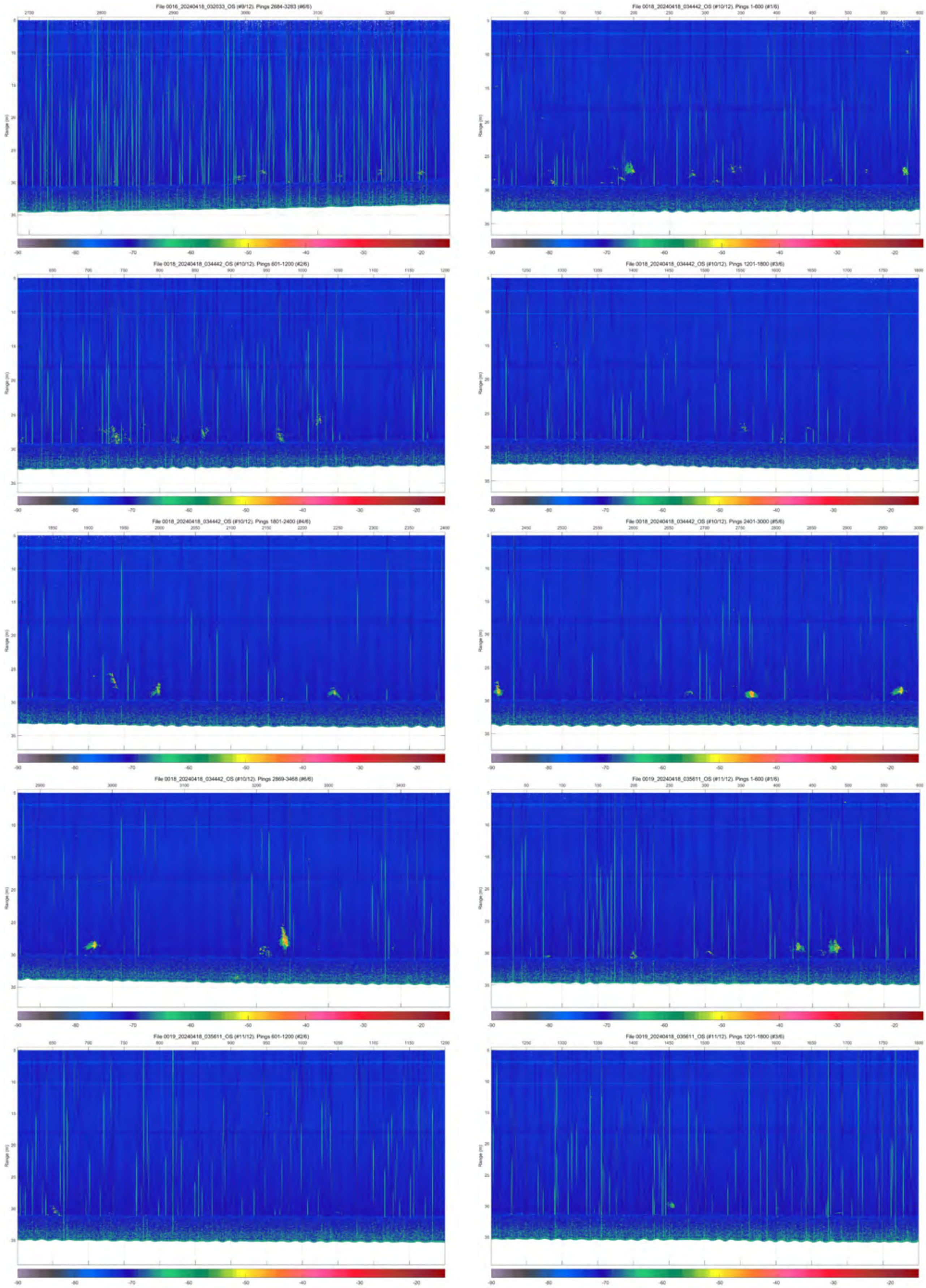
File 0016_20240418_032033_OS (#9/12). Pings 2684-3283 (#6/6)
File 0018_20240418_034442_OS (#10/12). Pings 1-600 (#1/6)
File 0018_20240418_034442_OS (#10/12). Pings 601-1200 (#2/6)
File 0018_20240418_034442_OS (#10/12). Pings 1201-1800 (#3/6)
File 0018_20240418_034442_OS (#10/12). Pings 1801-2400 (#4/6)
File 0018_20240418_034442_OS (#10/12). Pings 2401-3000 (#5/6)
File 0018_20240418_034442_OS (#10/12). Pings 2869-3468 (#6/6)
File 0019_20240418_035611_OS (#11/12). Pings 1-600 (#1/6)
File 0019_20240418_035611_OS (#11/12). Pings 601-1200 (#2/6)
File 0019_20240418_035611_OS (#11/12). Pings 1201-1800 (#3/6)

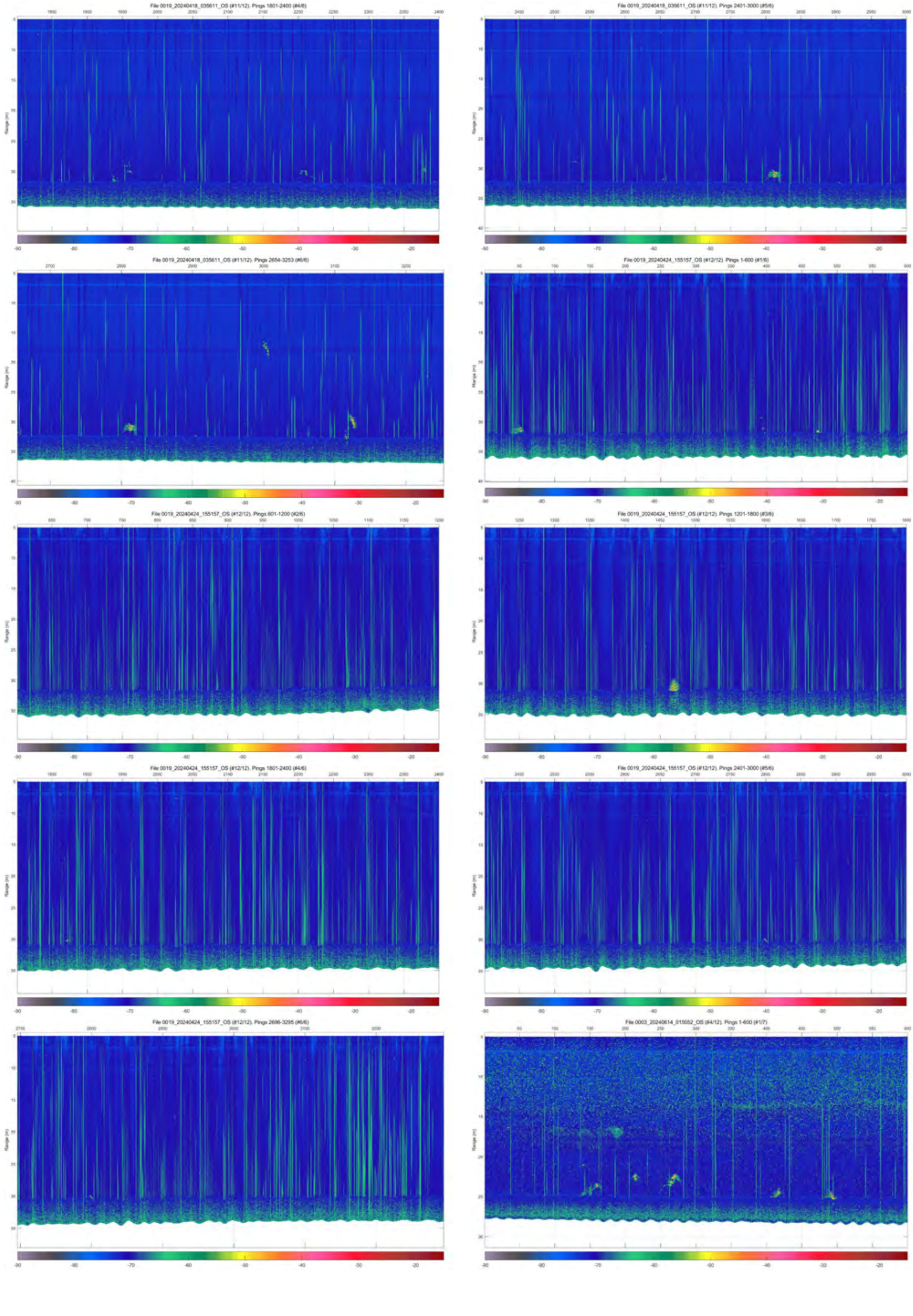

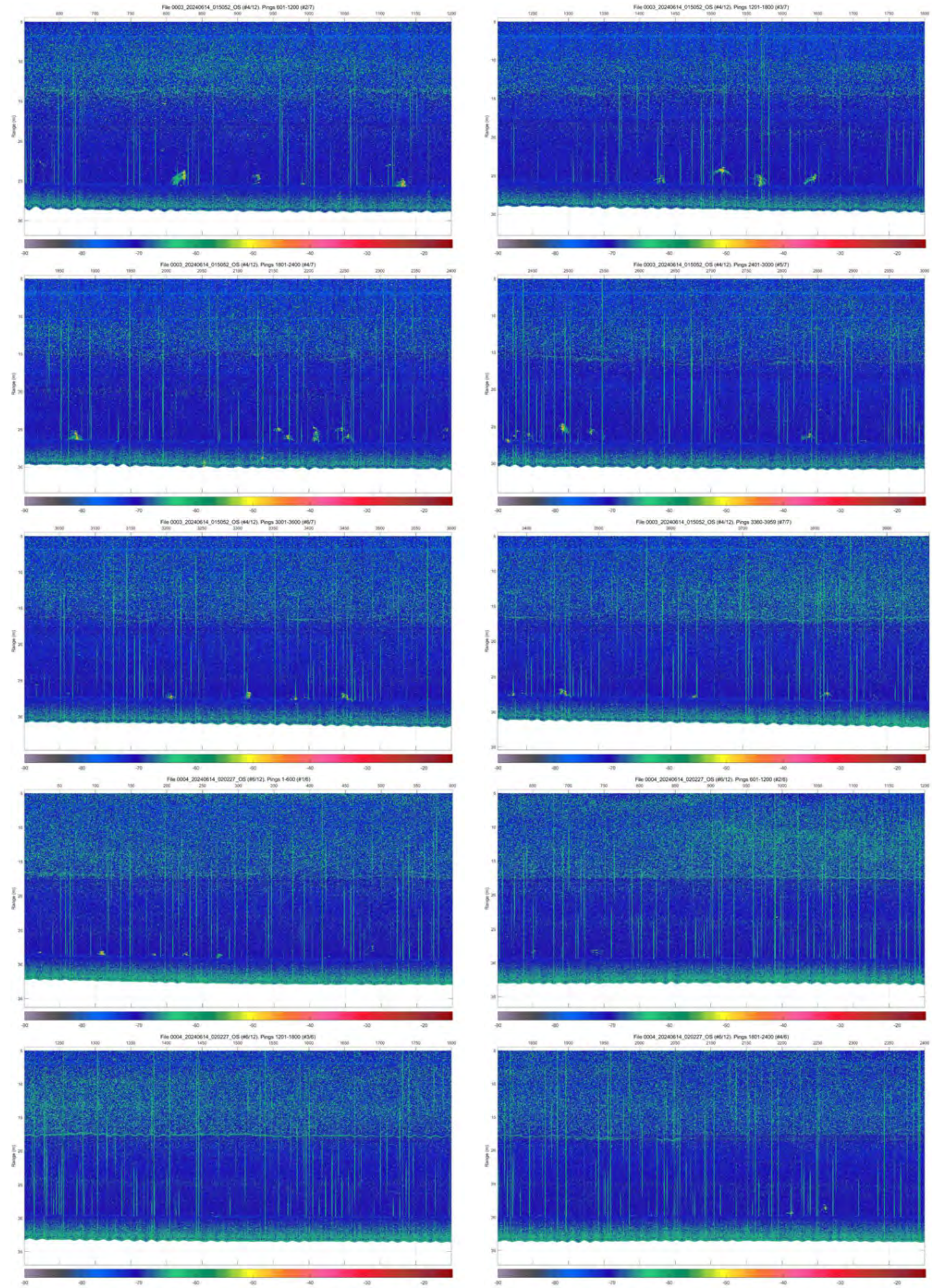

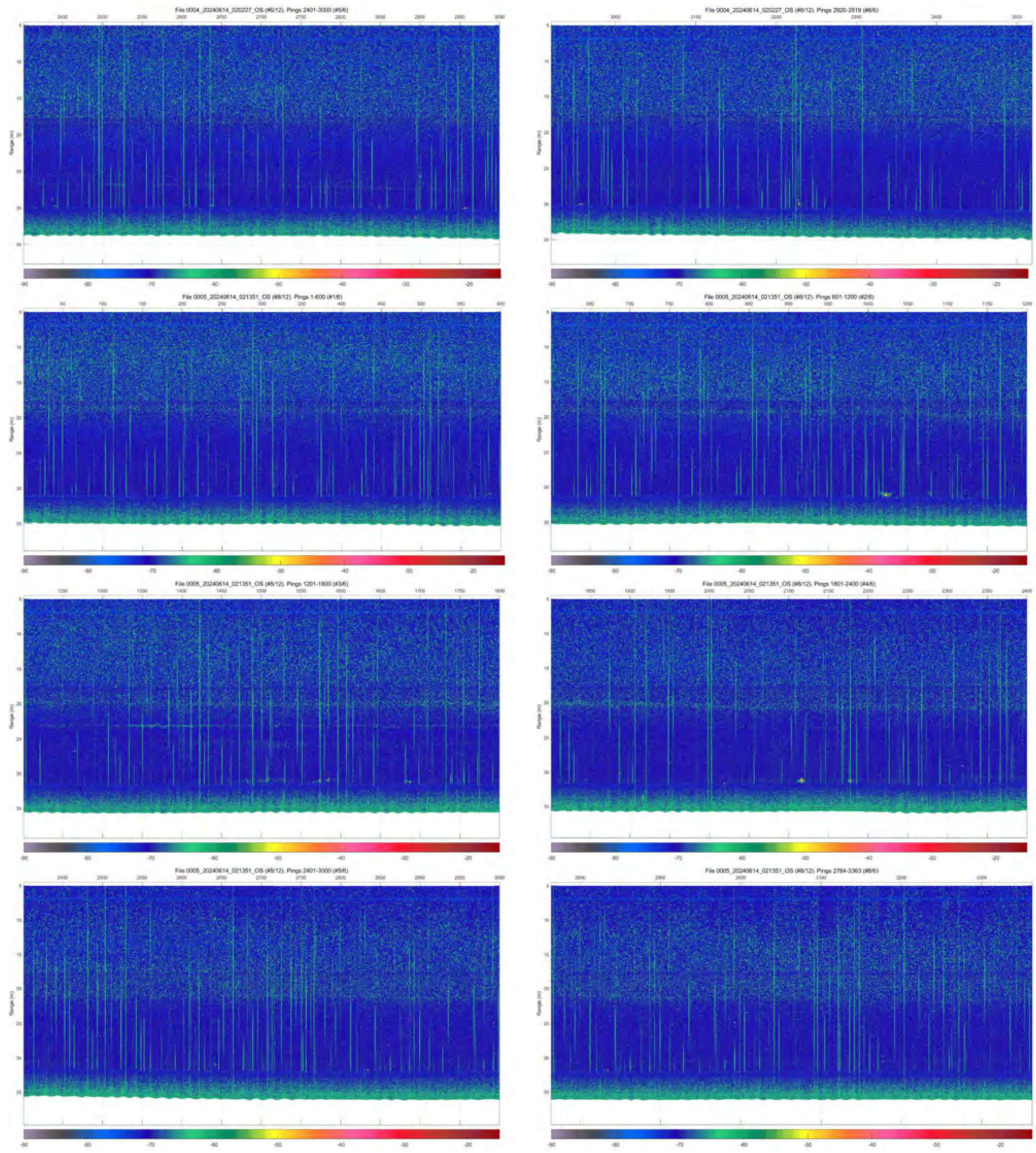

Area 3:

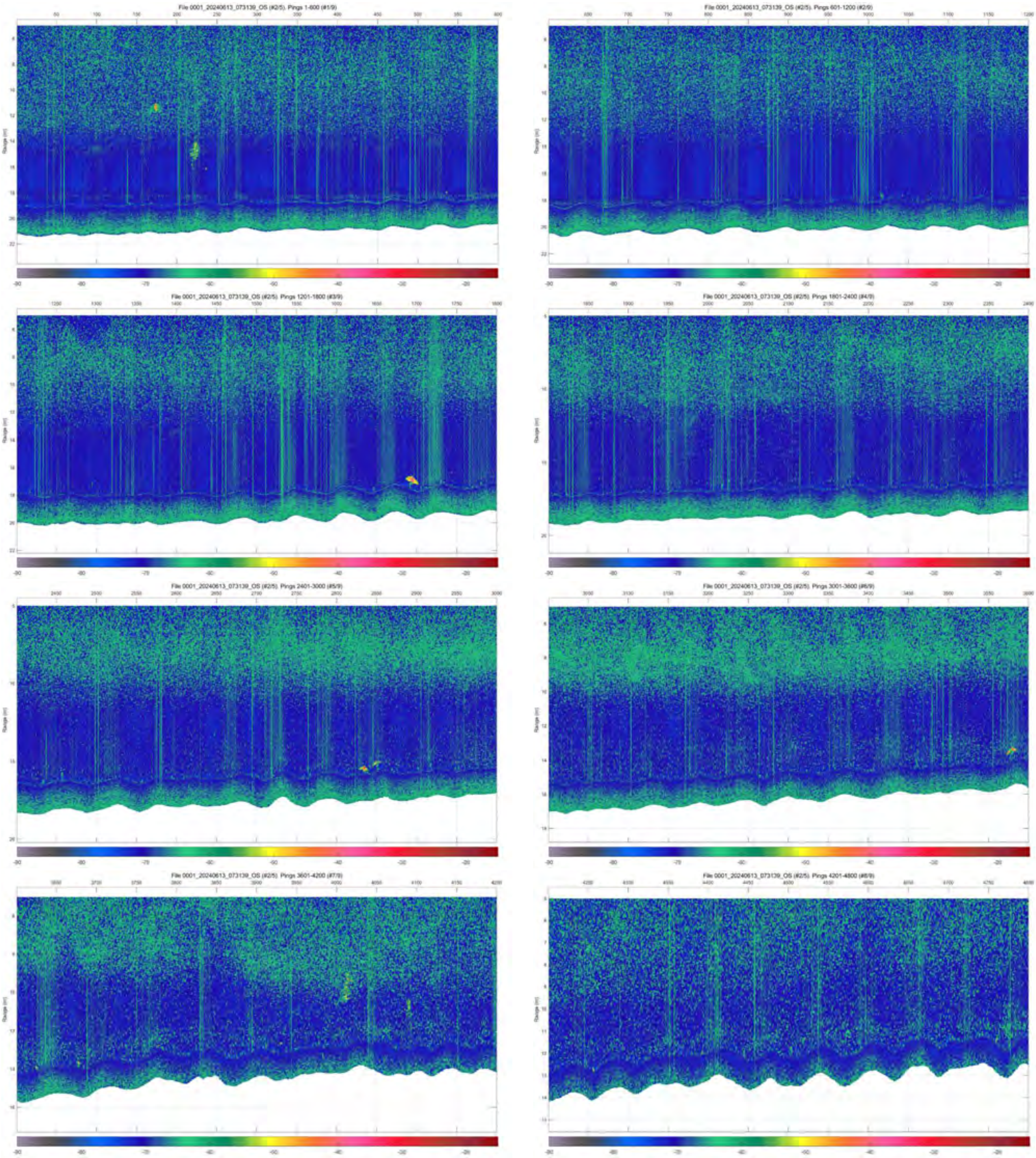
File 0001_20240613_073139_OS (#2/5). Pings 1-600 (#1/9)
File 0001_20240613_073139_OS (#2/5). Pings 601-1200 (#2/9)
File 0001_20240613_073139_OS (#2/5). Pings 1201-1800 (#3/9)
File 0001_20240613_073139_OS (#2/5). Pings 1801-2400 (#4/9)
File 0001_20240613_073139_OS (#2/5). Pings 2401-3000 (#5/9)
File 0001_20240613_073139_OS (#2/5). Pings 3001-3600 (#6/9)
File 0001_20240613_073139_OS (#2/5). Pings 3601-4200 (#7/9)
File 0001_20240613_073139_OS (#2/5). Pings 4201-4800 (#8/9)

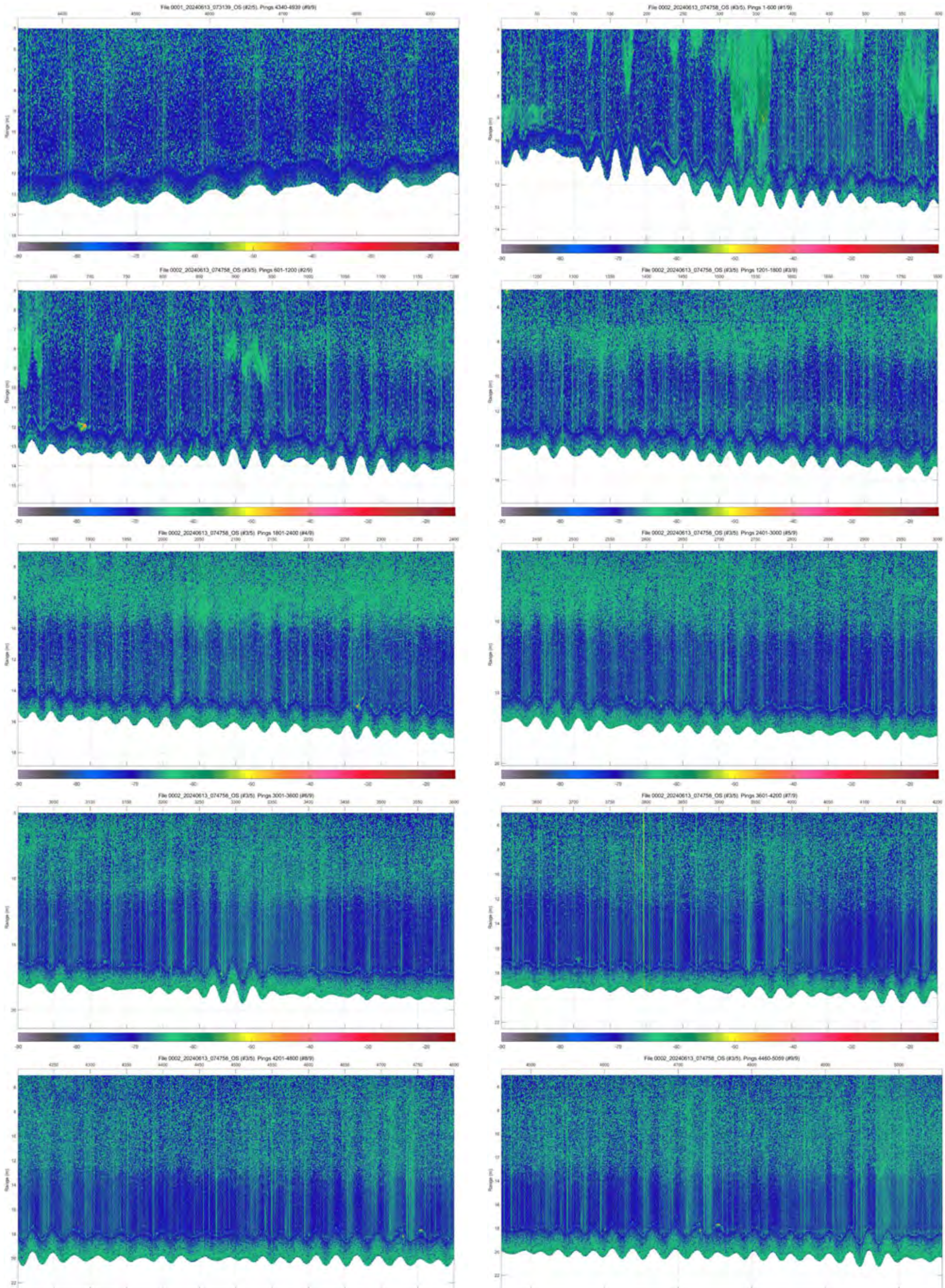

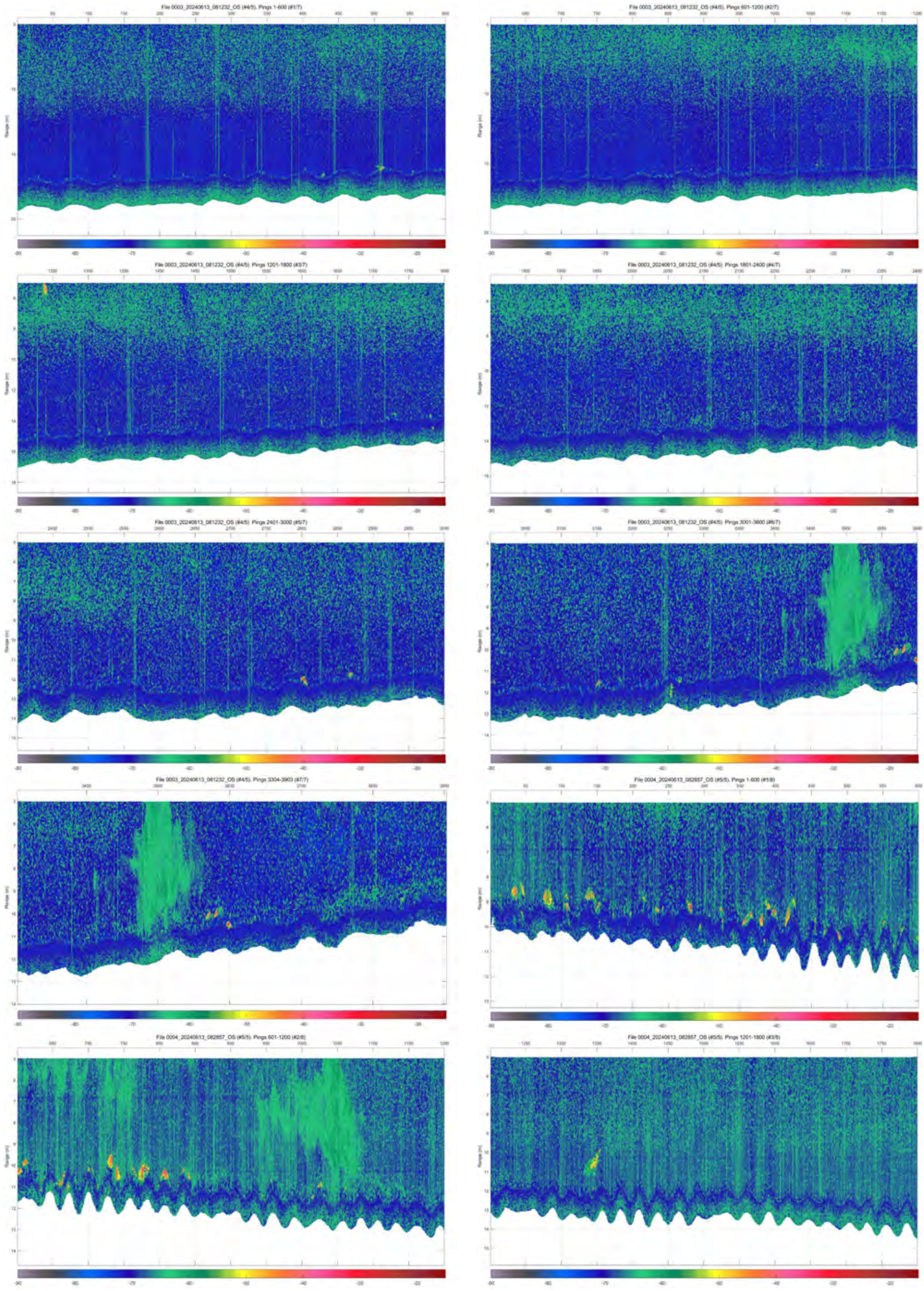

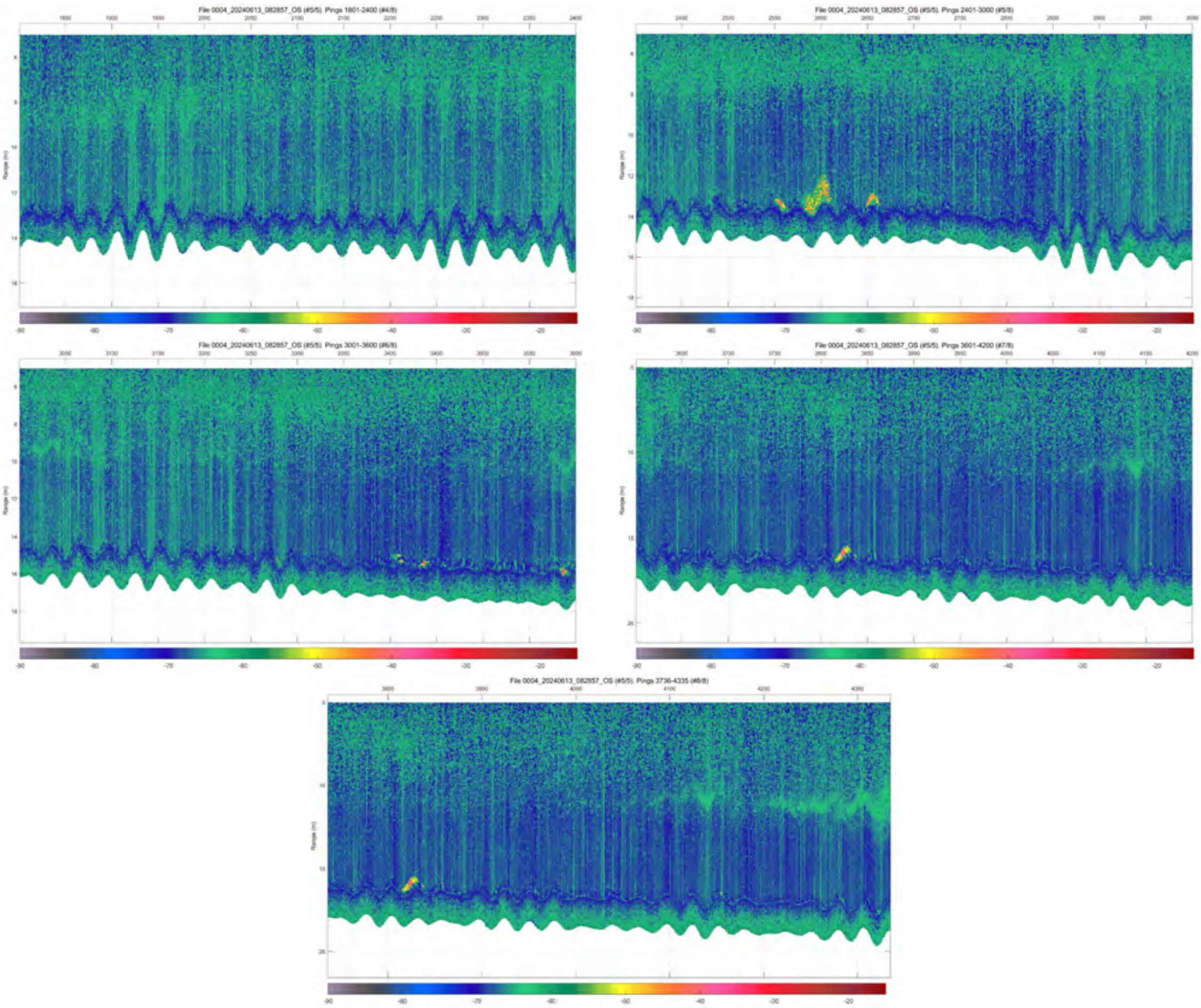
File 0004_20240613_082857_OS (#5/5). Pings 1801-2400 (#4/8)
File 0004_20240613_082857_OS (#5/5). Pings 2401-3000 (#5/8)
File 0004_20240613_082857_OS (#5/5). Pings 3001-3600 (#6/8)
File 0004_20240613_082857_OS (#5/5). Pings 3601-4200 (#7/8)
File 0004_20240613_082857_OS (#5/5). Pings 3736-4335 (#8/8)

Appendix C

Python script used for current calculations.

To run, download the script from GitHub at: github.com/vbacklin/marine_geo_thesis.. The data is downloaded from SMHI at; smhi.se/data/hav-och-havsmiljo/strommar/current/38058. Simply place the data, renamed as ”current_data.csv”, in the same folder as the python scrip and run.

```
import math
import numpy as np

def mean(vector):
    s = sum(vector)
    n = len(vector)
    return s/n

def calculate_average_direction(d_vector):
    radians = [math.radians(d) for d in d_vector]
    sin_dir = [math.sin(r) for r in radians]
    cos_dir = [math.cos(r) for r in radians]
    sin_mean = mean(sin_dir)
    cos_mean = mean(cos_dir)
    rad_avg = math.atan2(sin_mean, cos_mean)
    deg_avg = math.degrees(rad_avg) % 360
    return deg_avg

def calculate_average_scaled_direction(vd_vector):
    sin_dir = [v*math.sin(math.radians(d)) for (v, d) in vd_vector]
    cos_dir = [v*math.cos(math.radians(d)) for (v, d) in vd_vector]
    sin_mean = mean(sin_dir)
    cos_mean = mean(cos_dir)
    rad_avg = math.atan2(sin_mean, cos_mean)
    deg_avg = math.degrees(rad_avg) % 360
    return deg_avg

filename = "current_data.csv"
with open(filename, 'r') as f:
    lines = f.readlines()
    directions = {"April, 2019": [],
                  "April, 2020": [],
                  "April, 2021": [],
                  "April, 2022": [],
                  "April, 2019 - 2022": []}
    velocities = {"April, 2019": [],
                  "April, 2020": [],
                  "April, 2021": [],
                  "April, 2022": [],
                  "April, 2019 - 2022": []}
    both = {"April, 2019": [],
            "April, 2020": [],
            "April, 2021": [],
            "April, 2022": [],
            "April, 2019 - 2022": []}
    buffer = True
    for line in lines:
        cells = line.split(';')
        if buffer:
            if cells[0] == "Datum Tid (UTC)":
                buffer = False
        else:
            month = cells[0].split('-')[1]
            year = cells[0].split('-')[0]
            if cells[1]:
```

```
                direction = float(cells[1])
                if month == '04':
                    directions[f'April, {year}'].append(direction)
                    directions['April, 2019 - 2022'].append(direction)
            if cells[6]:
                velocity = float(cells[6])
                if month == '04':
                    velocities[f'April, {year}'].append(velocity)
                    velocities['April, 2019 - 2022'].append(velocity)
            if cells[6] and cells[1]:
                if month == '04':
                    both[f'April, {year}'].append((velocity, direction))
                    both['April, 2019 - 2022'].append((velocity, direction))
for key in directions.keys():
        avg_dir = calculate_average_direction(directions[key])
        avg_vel = mean(velocities[key])
        median_vel = np.median(velocities[key])
        max_vel = np.max(velocities[key])
        scaled_dir = calculate_average_scaled_direction(both[key])
        print(f'\n{key}')
        print(f'Avg. direction: {round(avg_dir)}')
        print(f'Avg. velocity: {round(avg_vel)}')
        print(f'Velocity median: {round(median_vel)}')
        print(f'Velocity maximum: {round(max_vel)}')
        print(f'Velocity scaled vector direction: {round(scaled_dir)}')
```